

On Optimality and Efficiency of Parallel Magnetic Resonance Imaging Reconstruction: Challenges and Solutions

A Dissertation
Presented to
The Academic Faculty

By

Roger Nana

In Partial Fulfillment
Of the Requirements for the Degree
Doctor of Philosophy in
Bioengineering

Georgia Institute of Technology

December 2008

On Optimality and Efficiency of Parallel Magnetic Resonance Imaging
Reconstruction: Challenges and Solutions

Approved by:

Dr. Xiaoping Hu, Advisor
School of Biomedical Engineering
Georgia Institute of Technology

Dr. Diego Martin
School of Medicine
Emory University

Dr. John Oshinski
School of Biomedical Engineering
Georgia Institute of Technology

Dr. Hui Mao
School of Medicine
Emory University

Dr. Shella Keilholz
School of Biomedical Engineering
Georgia Institute of Technology

Date Approved: November 5, 2008

=====

ACKNOWLEDGMENTS

I would like to express my profound gratitude to my advisor, Dr. Xiaoping Hu, whose expertise, understanding, and patience, added considerably to my graduate experience. He helped make the Ph.D. journey more enjoyable. I am also grateful to the members of my committee, Dr. Diego Martin, Dr. John Oshinski, Dr. Hui Mao, and Dr. Shella Keilhohz for their inputs and interests in this research.

Sincere thanks to Dr. Tiejun Zhao for his exceptional support. He has always been the first one to listen to my ideas, and has also devoted hours in discussing many aspects of my work. Special thanks to Dr. Keith Heberlein, whose support has been crucial during my early steps into the MRI world. Particular thanks to Dr. Andy James for proofreading the whole manuscript and for contributing to the scientific discussion.

I have been blessed by the opportunity to work at the Biomedical Imaging Center of Georgia Tech/Emory University School of Medicine. The friendly and supportive atmosphere inherent to the whole group contributed to the final outcome of my studies. In this context, I would like to thank particularly Dr. Lei Zhou, Christopher Gielmi, Jaemin Shin, Robert Smith, and Katrina Gourde for their support in different aspects.

Cordial thanks to Dr. Sven Zuehlsdorff, Dr. Rene Jerecic, and Dr. Brian Dale from Siemens Medical Solutions for providing all cardiac data used in this work. Thanks to Dr. Xiaodong Zhong for helpful discussion.

Very special thanks to my friends Remond Mbiada, Alphonse Kampto, and Roseline Bilina for their constant encouragement and moral support throughout the Ph.D. journey.

I am most thankful to my family, Daryl, Erwin, and Nadine, for their patience, love, constant support, and understanding during my graduate studies.

The National Institutes of Health (RO1EB002009) and the Georgia Research Alliance supported this research.

TABLE OF CONTENTS

ACKNOWLEDGMENTS.....	iii
LIST OF TABLES	vii
LIST OF FIGURES	viii
LIST OF ABBREVIATIONS.....	ix
SUMMARY.....	xi
CHAPTER 1. INTRODUCTION	1
1.1 General Introduction	1
1.2 Statement of the thesis.....	3
1.3 Background	10
1.4 General Summary.....	35
1.5 Chapter 1 References	36
CHAPTER 2. Cross-Validation-based Kernel Support Selection for Improved Parallel MRI	
Reconstruction in k -space.....	43
2.1 Introduction	43
2.2 Methods.....	46
2.3 Results.....	53
2.4 Discussion	59
2.5 Conclusions	65
2.6 Chapter 2 References	65
CHAPTER 3. A Simple and Robust Metric for Selecting Optimal Reconstruction Parameters in k-space Based Parallel Imaging.....	68
3.1 Introduction.....	69
3.2 Theory	71
3.3 Methods.....	74
3.4 Results	78
3.5 Discussion	84
3.6 Conclusions	93
3.7 Chapter 3 References	93
CHAPTER 4. Passive Tracking of THE Calibration Information Change using Data Consistency Error to Improve Reconstruction Efficiency and accuracy in Dynamic Parallel Imaging.....	97
4.1 Introduction	98
4.2 Methods.....	99
4.3 Results	103
4.4 Discussion	106
4.5 Conclusions	113
4.6 Chapter 4 References	113

CHAPTER 5.	Non-cartesian parallel image reconstruction with deconvolution of under-sampled gridding (dug) in k -space	115
5.1	Introduction	115
5.2	Theory	119
5.3	Methods	127
5.4	Results	130
5.5	Discussion	133
5.6	Conclusions	137
5.7	Chapter 5 References	137
CHAPTER 6.	Single-shot Multi-echo Parallel EPI for DTI with Improved SNR and Reduced Distortion	141
6.1	Introduction	141
6.2	Methods	144
6.3	Results	148
6.4	Discussion	153
6.5	Conclusions	158
6.6	Chapter 6 References	158
CHAPTER 7.	Conclusions	162

LIST OF TABLES

Table 2-1 Reconstruction mean square error.....	61
Table 3-1 Comparison between reconstruction mean square error	92
Table 4-1 Comparison between the total reconstruction times (in sec).....	110
Table 5-1 Comparison between reconstruction mean square errors.....	134
Table 5-2 Comparison between computation times per unit image (in sec).....	136
Table 6-1 Echo times (ms) used for different acceleration factors	146
Table 6-2 Comparison between calculated FA values of selected ROIs	156
Table 6-3 Comparison between calculated T_2 values of selected ROIs	157

LIST OF FIGURES

Figure 1.1 Spin behavior in the presence of an external magnetic field.....	13
Figure 1.2 Elements of a pulse sequence and k -space	24
Figure 2.1 GRAPPA fitting procedure	47
Figure 2.2 Cross-validation re-sampling strategy used for kernel support selection.....	49
Figure 2.3 Configuration of the kernel supports to be examined by cross-validation	50
Figure 2.4 Sketch of the 8-element head array coil used to generate for simulation.....	52
Figure 2.5 Simulated and experimental plots of cross-validation errors	54
Figure 2.6 Reconstructed Shepp-Logan phantom images	56
Figure 2.7 Reconstructed brain data images.....	57
Figure 2.8 Reconstructed cardiac images	58
Figure 3.1 Shift invariance property of the GRAPPA kernel	72
Figure 3.2 Formation of the set of frames to be examined by DCE	77
Figure 3.3 Dependence of DCE and MSE on the kernel size	79
Figure 3.4 Comparison between reconstruction methods on brain data.....	81
Figure 3.5 Influence of the ACS lines number on the optimal kernel	82
Figure 3.6 Dependence of DCE and MSE on the number of calibrating frames.....	84
Figure 3.7 Comparison between reconstructions on dynamic cardiac data.....	85
Figure 3.8 Quantitative comparison between TGRAPPA reconstructions	89
Figure 4.1 Formation of the blocks of frames to be examined by DCE	102
Figure 4.2 Dependence of DCE and MSE on the block of frames	105
Figure 4.3 Comparison between reconstructed images	106
Figure 4.4 Quantitative comparison between TGRAPPA reconstructions.....	108
Figure 4.5 Dependence of DCE on block of frames on the truly-accelerated outflow track cardiac view dataset.....	110
Figure 4.6 Reconstruction results of two different outflow track view frames ($R = 3$)	112
Figure 5.1 Analysis procedure of the energy distribution during gridding.....	122
Figure 5.2 Absolute contribution maps for spiral trajectory.....	124
Figure 5.3 Relative contribution maps for spiral trajectory.....	125
Figure 5.4 Simulation results for radial trajectory.....	125
Figure 5.5 DUG weights calculation procedure	127
Figure 5.6 Non-Cartesian trajectories used	128
Figure 5.7 Spiral reconstructed images	131
Figure 5.8 Reconstruction quality and gridding window	132
Figure 5.9 Radial reconstructed images	135
Figure 6.1 Single-shot Multi-echo parallel DTI sequence block diagram.....	144
Figure 6.2 Evidence of geometric distortion reduction	149
Figure 6.3 Simulated and experimental SNR gain	150
Figure 6.4 Illustration of acquisition efficiency improvement	151
Figure 6.5 Comparison between T_2 maps.....	152
Figure 6.6 Comparison between SOS and weighted average echo combination.....	154

LIST OF ABBREVIATIONS

^1H :	Hydrogen
^{13}C :	Carbon 13
^{15}N :	Nitrogen 15
^{31}P :	Phosphorus 31
AIC:	Anterior limb of the internal capsule
AUTO-SMASH:	Self-calibrating technique for SMASH imaging
ACS:	Auto-calibrating signal
ADC:	Analog digital converter
CSF:	Cerebro-spinal fluid
CT:	Computed tomography
CV:	Cross-validation
DCE:	Data consistency error
DTI:	Diffusion tensor imaging
DUG:	Non-Cartesian parallel image reconstruction with deconvolution of under-sampled gridding
EC:	External capsule
EPI:	Echo planar imaging
FA:	Fractional anisotropy
FFT:	Fast Fourier transform
FID:	Free induction decay
FOV:	Field of view
g-factor:	Geometric factor
g-SMASH:	Generalized SMASH
GM:	Gray matter
GP:	Globus pallidus
GRAPPA:	Generalized auto-calibrating partially parallel acquisition
IDEA:	Integrated development environment and applications
MOG:	Middle occipital gyrus
MRI:	Magnetic resonance imaging
NMR:	Nuclear magnetic resonance
ORF:	Outer reduction factor
PARS:	Parallel magnetic resonance imaging with adaptive radius in k -space
PET:	Positron emission tomography
PG:	Postcentral gyrus
PIC:	Posterior limb of the internal capsule
PNS:	Peripheral nerve stimulation
RF:	Radio frequency
ROI:	Region of interest
SAR:	Specific absorption rate
SE:	Spin echo
SENSE:	Sensitivity encoding
SFG:	Superior frontal gyrus
SMASH:	Simultaneous acquisition of spatial harmonic
SMG:	Supra marginal gyrus
SNR:	Signal to noise ratio

SPACE-RIP	Sensitivity profiles from an array of coils for encoding and reconstruction in parallel
STG:	Superior temporal gyrus
T1:	Spin lattice relaxation time
T2:	Spin-spin relaxation time
TE:	Echo time
TGRAPPA	Temporal GRAPPA
TR:	Repetition time
TrueFISP:	True fast imaging with steady state precession true fast imaging with steady state precession
VD-AUTO-SMASH:	Variable density AUTO-SMASH
WM:	White matter

SUMMARY

Imaging speed is an important issue in magnetic resonance imaging (MRI), as subject motion during image acquisition is liable to produce artifacts in the image. Many of the new applications of MRI require much faster acquisition. However, the speed at which data can be collected in conventional MRI is fundamentally limited by physical and physiological constraints. Parallel MRI is a technique that utilizes multiple receiver coils to increase the imaging speed beyond previous limits by reducing the amount of acquired data without degrading the image quality.

In order to remove the image aliasing due to k -space undersampling, parallel MRI reconstructions invert the encoding matrix that describes the net effect of the magnetic field gradient encoding and the coil sensitivity profiles. The accuracy, stability, and efficiency of a matrix inversion strategy largely dictate the quality of the reconstructed image. This thesis addresses five specific issues pertaining to this linear inverse problem with practical solutions to improve clinical and research applications.

First, for reconstruction algorithms adopting a k -space interpolation approach to the linear inverse problem, two methods are introduced that automatically select the optimal k -space subset samples participating in the synthesis of a missing datum, guaranteeing an optimal compromise between accuracy and stability, i.e. the best balance between artifacts and signal-to-noise ratio (SNR). While the former is based on cross-validation re-sampling technique, the second utilizes a newly introduced data consistency

error (DCE) metric that exploits the shift invariance property of the reconstruction kernel to provide a goodness measure of k -space interpolation in parallel MRI. Additionally, the utility of DCE as a metric for characterizing and comparing reconstruction methods is demonstrated. Second, a DCE-based strategy is introduced to improve reconstruction efficiency in real time parallel dynamic MRI. Third, an efficient and reliable reconstruction method that operates on gridded k -space for parallel MRI using non-Cartesian trajectories is introduced with a significant computational gain for applications involving repetitive measurements. Finally, a pulse sequence that combines parallel MRI and multi-echo strategy is introduced for improving SNR and reducing the geometric distortion in diffusion tensor imaging. In addition, the sequence inherently provides a T2 map, complementing information that can be useful for some applications.

CHAPTER 1. INTRODUCTION

1.1 General Introduction

Since the pioneering work by Lauterbur in the 1970s, magnetic resonance imaging (MRI) has revolutionized the field of medical imaging (1). Several factors contribute to the continuing widespread clinical and research use of MRI; it can provide good contrast between soft tissue types; it can produce high-resolution 3D images with high signal-to-noise ratio (SNR), and it does not employ ionizing radiation. The major drawback of MRI is imaging speed, as subject motion during image acquisition is liable to produce artifacts in the images. Many of the new applications of MRI require much faster imaging. Unfortunately, physiological safety guidelines limit the speed of conventional MRI. Parallel MRI is a recently introduced technique that relies on radiofrequency (RF) coil arrays to achieve acquisition speed not possible with conventional MRI (2-9).

The goal in MRI is to image the spatial distribution of atom nuclei (generally water hydrogen protons) in a subject. Conventional MRI makes use of spatial linearly varying magnetic fields (magnetic field gradients) to encode the localized nuclear magnetic resonance (NMR (10,11)) signal in order to produce an image. This gradient encoding process requires a sequential switching of the magnetic field gradients a greater number of times than the number of uniquely-identifiable spatial information of the object along

the phase encoding¹ direction (1,12). This sequential requirement imposes a significant time penalty since the time that separates two gradient encoding steps may range in the order of hundred microseconds or milliseconds. The traditional method for reducing MRI acquisition time has been to use faster gradient hardware. Unfortunately, safety measures regarding magnetic field switching rates and RF power deposition limit the speed achievable in conventional MRI.

The spatial variations in the sensitivities of an array of receiver coils can emulate the effect of gradient encoding on the NMR signal (2). Therefore, if conventional MRI acquisition were performed with an array of RF coils, there would be some redundancy in the spatial encoding of the NMR signal. To image an object, parallel MRI exploits this redundancy with RF coil arrays to reduce the number of times the magnetic field gradient is required to be switched on and off. In other words, some of the magnetic gradient encoding steps can be omitted during acquisition (i.e. the data can be undersampled below Nyquist requirement) without Nyquist-aliasing artifacts in the reconstructed image, consequently accelerating the image acquisition. Thus, parallel MRI offers faster imaging than conventional MR imaging of the same object at the same resolution.

By markedly increasing the acquisition speed, parallel MRI improves image quality, reduces examination time, improves patient comfort, and permits the imaging of

¹ Phase encoding is the process by which spins are spatially encoded based on their phase evolution over time. This is generally performed in a direction orthogonal to the direction of the signal readout. (see section 1.3.2.2.1)

moving structures. Currently, parallel MRI is a widely used commercial product with significant impacts on almost every practical aspect of MRI (13).

1.2 Statement of the thesis

The quality of a parallel-acquired MR image is in large dictated by the performance of the image reconstruction method. Although parallel MRI is an established technique and available in virtually all latest generation of MRI scanners, various challenges in image reconstruction still impede many aspects of its routine use. This thesis addresses five important aspects of parallel MRI reconstruction with practical solutions to ease routine clinical and research applications.

1.2.1 Accuracy and stability

In order to remove the image aliasing due to k -space² undersampling, parallel MRI reconstruction must invert the encoding matrix that describes the net effect of magnetic field gradient encoding and coil sensitivity encoding. In general, two main strategies are currently used for this inversion process: direct and indirect inversion. Most direct inversion-based reconstruction methods formulate the linear inverse problem in image space and an explicit determination of the encoding matrix is required. While it may be numerically unstable and computationally intensive to calculate the matrix inverse, the direct inversion approach has the appeal of a theoretically exact solution. Additionally, a variety of conditioning and regularization techniques have proven useful to mitigate instability of the direct inversion-based reconstruction (14).

² k -space represents the domain in which the signal is acquired and corresponds to the Fourier transform of the image space. (see section 1.3.2.2.1)

The indirect inversion approach operates in k -space and an explicit determination of the encoding matrix is not needed. Rather, each missing datum is interpolated from only a few local acquired samples from all coil channels. Reconstruction algorithms utilizing this approach are generally referred to as k -space based reconstructions. Implementation of the indirect inversion approach presents several advantages including numerical stability and computational efficiency, but makes the solution to the inverse problem inexact. Performance of reconstruction strongly depends on the selection of the local acquired k -space samples, or reconstruction kernel. For example, small kernels may be inadequate in capturing the complexity of the k -space interpolation while large kernels tend to be overly sensitive to errors in the data (15-17). The optimal kernel, which has been shown to depend on coil array configuration, noise level in the acquired data, imaging configuration, and calibration data, must provide a suitable compromise between these limits. In general, there has been an insufficient understanding of how to automatically control the errors in the indirect inversion reconstruction.

In Chapter 2, the different types and sources of errors involve in indirect inversion based parallel MRI reconstruction are discussed. It is shown that for a given undersampled dataset, only the kernel support can be varied to influence the total error. A method based on cross-validation (CV) is proposed which automatically select the optimal kernel support that best balances the conflicting demands of fit accuracy and stability (i.e. between artifacts and SNR) in the reconstruction. In this method, the kernel selection is posed as a model selection problem and cross-validation is used for selecting

a regression model among a group of candidate models. Specifically, the method is demonstrated with the generalized auto-calibrating partially parallel acquisition (GRAPPA (8)). The effectiveness of CV-selected kernel support in image reconstruction is evaluated with simulated and experimental data, and compared with standard GRAPPA reconstruction.

Along the same line, Chapter 3 introduces a simple and robust data consistency error (DCE) function for selecting the optimal kernel settings (e.g. kernel support size, kernel support configuration, calibration dataset) among a set of settings that influence the performance of parallel MRI reconstruction in k -space. As an alternative to cross-validation (introduced in Chapter 2), which relies only on the low k -space information, DCE integrates information at all acquired resolutions and is therefore more robust and balanced. Additionally, DCE is computationally efficient compared to cross-validation. DCE exploits the shift invariance property requirement of the reconstruction kernel to provide a goodness measure of k -space based parallel MRI reconstruction algorithms. As an illustration of its utility, strategies for utilizing DCE to select the optimal kernel support for GRAPPA and the optimal calibration dataset for temporal GRAPPA (TGRAPPA (18)) are outlined with the presentation of *in vivo* results.

1.2.2 Performance assessment

The design of a parallel MRI reconstruction method should be validated for particular coil array geometries and sampling trajectory. This suggests the need for quantitative measures for assessing reconstruction performance. The performance of

parallel MRI reconstruction employing direct matrix inversion has been generally quantified using metrics such as g-factor (3) which measures the degree of noise amplification in reconstructed images. For indirect inversion based reconstructions, however, the noise amplification solely cannot provide a good performance assessment of the reconstruction because of the presence of many other dominant errors that include model errors (approximation error) and other noise-related errors. Tools for quantifying the total error for k -space based parallel MRI reconstructions have been lacking.

The data consistency error (DCE) function introduced in Chapter 3 is proposed as a measure for quantifying the performance of k -space based parallel MRI reconstructions. It is shown by simulation on experimental data that there is a strong correspondence between DCE and the mean square error (i.e. the normalized mean square difference between the reduced-data reconstructed image and the full-data reconstructed image). The potentials of DCE as a quantitative metric for characterizing reconstruction error, for comparing different parallel image reconstruction algorithms, and more importantly for optimizing reconstructions are explored on GRAPPA and TGRAPPA reconstructions.

1.2.3 Computational efficiency for real time accelerated dynamic datasets

Reconstruction time is one of the most important factors to be considered in a parallel image reconstruction algorithm for real time accelerated dynamic acquisition. To reconstruct an image from an undersampled dataset, parallel imaging relies on prior knowledge of the coil arrays sensitivities. The coil sensitivity information is generally obtained through calibration. In dynamic MRI acquisition such as free breathing cardiac

imaging with flexible cardiac matrix coils, the coil sensitivities change in time due to respiration induced chest wall excursions. This requires that the calibration information be determined for every time frame, possibly leading to long reconstruction time. Reconstruction efficiency may be improved since the cyclic respiratory induced chest wall movement may cause many frames to carry approximately the same calibration information.

In chapter 4, an approach is introduced that utilizes DCE to provide a consistency measure of the frame-to-frame calibration information change in real time dynamic parallel imaging. This tracking information can be exploited to improve the reconstruction efficiency and accuracy by allowing time frames to share the same calibration information and avoid using inconsistent calibrating frames. The method is demonstrated using TGRAPPA with *in vivo* free-breathing cardiac imaging data. Compared to the original TGRAPPA, the modified TGRAPPA produces images with reduced artifacts and allows for faster reconstruction. The method is simple and robust and can be applied to other real-time parallel dynamic image reconstructions.

1.2.4 Computational efficiency for non-Cartesian trajectories

While parallel imaging has enjoyed great success with sequences based on rectilinear sampling, incorporating non-Cartesian sampling into parallel imaging poses non-trivial challenges in the reconstruction. It has been recognized that in some applications, non-Cartesian sampling trajectories such as spiral (19) and radial (20) may be preferred. In general, parallel MRI reconstructions from partially acquired non-

Cartesian k -space data require the solution of large linear equation systems, which pose greater challenges due to memory requirement and computational demand for inverting large matrices.

In the last few years, several algorithms for reconstructing non-rectilinear undersampled datasets have been proposed (15,21-24). Despite the successes of these algorithms, no commercial scanner has been reported to support reconstruction of undersampled non-Cartesian k -space data. This suggests that it remains a challenge to rapidly and reliably reconstruct an image from undersampled non-Cartesian k -space data. This challenge is higher in applications involving large volume of datasets such as functional MRI (25), perfusion weighted imaging (26), and diffusion tensor imaging (27).

Chapter 5 presents an approach for efficiently reconstructing non-Cartesian undersampled k -space datasets. Typically an indirect inversion based method, the approach operates on gridded k -space. A rigorous GRAPPA interpolation on the gridded data requires a different fitting kernel for each datum (24) because an invariant kernel is not applicable. Consequently, the reconstruction process can be very time consuming. To overcome this difficulty, a strategy is presented that exploits the pattern of energy distribution during the gridding process to reduce the number of kernels per coil, necessary to produce high quality image, down to the parallel imaging acceleration factor. This number of kernels per coil is only one kernel more than that of a normal Cartesian GRAPPA, a significant gain for non-Cartesian applications involving repetitive

measurements such as functional MRI, perfusion MRI, and diffusion tensor imaging. Reconstructions of *in vivo* undersampled spiral and radial datasets are demonstrated.

1.2.5 SNR improvement in parallel Diffusion Tensor Imaging

Diffusion tensor imaging (DTI) is a recently developed MRI technique that can provide information regarding the architecture and microstructure of a tissue through characterization of free diffusion (i.e. Brownian motion) of water in tissue. The greatest technical difficulty in DTI acquisition is to overcome the effects of macroscopic tissue motion, while retaining sensitivity to microscopic water motion. Single-shot echo planar imaging (EPI (28)) is the most widely used acquisition strategy for DTI owing to its insensitivity to motion. However, limited spatial resolution, geometric distortion, and low SNR are serious EPI limitations (29). These limitations severely entangle the *in vivo* applications of DTI particularly in the regions of strong field inhomogeneities.

Parallel MRI has been proposed as a means to reduce artifacts and improve spatial-temporal resolution in DTI. However, parallel MRI may compromise the SNR as a result of reduced acquired data, which is detrimental for DTI since SNR is often limited in DTI. In practice, multiple measurements are often performed to recover the SNR lost, which results in lengthy scan times, annulling the speed benefit of parallel imaging. It is therefore important to adapt parallel DTI sequences to improve image SNR without compromising the advantages of parallel MRI.

In Chapter 6, a single-shot multi-echo parallel EPI pulse sequence is proposed to improve the acquisition efficiency in parallel diffusion tensor imaging (DTI). It is demonstrated by simulation and by experiments that with an appropriate echo combination strategy the sequence can provide a SNR enhancement while maintaining the advantages of parallel EPI. It is also experimentally shown that this SNR gain can be utilized to reduce the number of measurements often required to ensure adequate SNR for accurate DTI measures. Additionally, it is shown that the multiple echoes can be used to derive a T_2 map³, providing additional information that might be useful in some applications.

1.3 Background

This section describes principles and terminologies necessary for appropriate appreciation of the thesis aims. A more detail explanation of the physical and engineering principles of MRI can be found in many textbooks (30). To varying degrees and without rigorous derivation, the section provides the highlights of the physics behind MR signal generation and how this signal is translated into an image. To put parallel MRI in context and enable the reader to appreciate the necessity of its development, a brief description of spatial encoding and decoding in conventional MRI is provided as well as traditional strategies to accelerate the scan time. The basic concepts of parallel MRI and selected examples of parallel image reconstruction methods are described.

³ T_2 map is a graphical representation of the spin-spin relaxation time distribution (see section 1.3.1.2)

1.3.1 Review of MR physics

Felix Bloch and Edward Purcell independently demonstrated the phenomenon of nuclear magnetic resonance (NMR) in 1946 (10,11). In 1952, they were both awarded the Nobel Prize in Physics for the discovery. NMR relies on a few principles. All elements with nuclear *spin* placed in an external magnetic field *oscillate*. The frequency at which they oscillate depends on the strength of the magnetic field. These nuclei are capable of absorbing energy if exposed to electromagnetic energy at the frequency of oscillation. After absorption of the energy, the nuclei release or reradiate this energy to return to their initial state of equilibrium. This reradiated or transmitted energy is detected as MR signal. From the MR signal, information about physical and chemical properties of the excited elements can be obtained. NMR finds applications in many fields of science, medicine, and engineering.

1.3.1.1 Nuclei behavior

Certain nuclei (^1H , ^{13}C , ^{15}N , ^{31}P , among others) have spin states, and thus behave like tiny bar magnets with magnetic dipole moments. In the absence of magnetic field, the dipole moments are randomly oriented (Figure 1.1a). In the quantum world, this scenario is indicative of a degenerate state where all particles in the population are expected to reside in the same energy level. In the presence of a magnetic field the nuclei can align either towards or against the induced field (Figure 1.1b). Nuclei aligned with the field are in a lower energy state (spin-up) than those aligned against (spin-down). The energy difference between the states is given by $\Delta E = \hbar\omega_0$ where \hbar is Plank's constant

and ω_0 is the *Larmor frequency* or *resonance frequency*. The Larmor frequency is given by

$$\omega_0 = \gamma B_0, \quad [1.1]$$

where B_0 is the strength of the external magnetic field and γ is the gyromagnetic ratio of the nucleus under consideration. The current discussion is restricted to hydrogen nuclei ^1H as it is the primarily focus in MRI. The ^1H atom gyromagnetic ratio is 42.58 MHz/Tesla and its resonance frequency in a 1.5 Tesla magnetic field typical for MRI is approximately 63 MHz. A group of spins experiencing the same magnetic field has a net magnetization that represents the difference in the amount of spin-up and spin-down particles. An approximation of this net magnetization is given by

$$M_0 \approx \frac{\gamma^2 \hbar^2 B_0 N_s}{4kT_s} \rho, \hbar\omega_0 \ll kT_s. \quad [1.2]$$

Here, k is the Boltzmann's constant, N_s is the number of spins in the group, T_s is the sample's temperature, ρ is the spin density, M_0 is the magnetization vector magnitude, and B_0 is the main magnetic fields strength. It is important to note from Eq. [1.2] that the net magnetization can be maximized in practical circumstances by utilizing high static magnetic field strengths, interrogating a large spin population, or lowering the sample's temperature (this later strategy is not suitable for medical purposes)(31).

At equilibrium, the net magnetization is aligned with the static main magnetic field orientation (Figure 1.1c). In transition state, the net magnetization is composed of the *longitudinal* component M_z along the orientation of the main magnetic field, and the *transversal* part M_T which is perpendicular to the longitudinal direction.

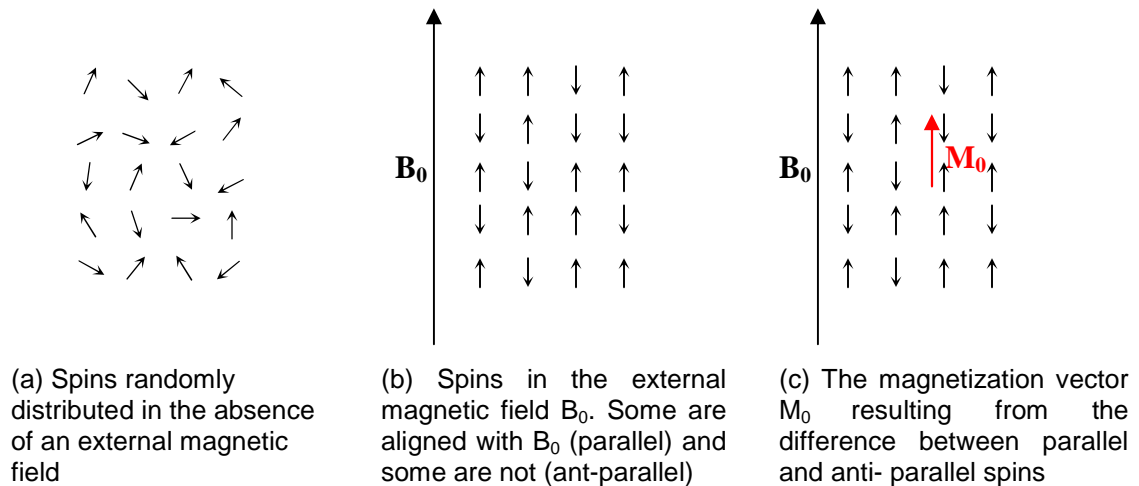


Figure 1.1 Spin behavior in the presence of an external magnetic field

1.3.1.2 Relaxation phenomenon

The magnetization vector can be rotated from its equilibrium orientation (longitudinal) towards the transverse plane by applying a radiofrequency (RF) excitation pulse having the resonance frequency. The overall effect of the RF excitation can be measured by an angle α , which is given by

$$\alpha \cong \gamma B_1 \Delta t . \quad [1.3]$$

In Eq. [1.3] B_1 is the strength of the RF field and Δt is the duration of the RF pulse. If the spin system is left alone at this point, the nuclei will return to their equilibrium state. The return of the nuclei to their equilibrium state does not take place instantaneously, but rather takes place over some time. Two physical processes govern this return: the relaxation back to equilibrium of the longitudinal component of the net magnetization referred as T_1 -relaxation, and the relaxation back to equilibrium of its transversal component known as T_2 -relaxation.

The T_1 -relaxation process is due to interaction of the spins with the surrounding tissue (spin-lattice interaction). The re-growth of the magnetization, after it is rotated from its equilibrium orientation is given by

$$M_z(t) = M_0(1 - e^{-\frac{t}{T_1}}). \quad [1.4]$$

T_1 in human is on the order of 100 – 1000 ms and is specific for every tissue [85, 36, 101].

The T_2 relaxation process is related to the spin-spin interaction. Spins generate their own small magnetic fields. The combination of these micro fields with the main magnetic field leads to local variations of the net field, which is generally referred as magnetic field inhomogeneity. This in turn causes spins to resonate at different frequencies creating phase shift over time, since each spin *experiences* a slightly different magnetic field. Over time, this will diminish the transverse magnetization. This decay of the transverse magnetization is given by

$$M_T(t) = M_0 e^{-\frac{t}{T_2}}. \quad [1.5]$$

A typical T_2 relaxation time for protons in human is 40 – 100ms and is always shorter than T_1 time. Eqs. [1.4] and [1.5] are particular solutions of the generalized Bloch equations [101].

For most soft tissues in the human body, the proton density is somewhat homogeneous and therefore does not contribute in a major way to signal differences seen in an image. However, T_1 and T_2 can be dramatically different for different soft tissues,

and these parameters are responsible for the major contrast between soft tissues. T_1 and T_2 are strongly influenced by the viscosity or rigidity of a tissue. Generally speaking, the greater the viscosity and rigidity, the smaller the value for T_1 and T_2 . It is possible to manipulate the MR signal by changing the way in which the nuclei are initially subjected to electromagnetic energy. This manipulation can change the dependence of the observed signal on three parameters: proton density, T_1 and T_2 . This explains the existence of a number of different MR imaging techniques ("weightings"), which accentuate some tissue properties and not others.

1.3.1.3 The MR signal

At equilibrium, the angle between the proton magnetic moment and the external magnetic field is not exactly zero. The spinning magnetic moment experiences a torque from the constant magnetic field. This torque, which is perpendicular to both the magnetic field and the proton magnetic moment, causes the proton moments (and subsequently the net magnetization vector) to *precess*, around the main magnetic field axis at the Larmor frequency. When the net magnetization is flipped toward the transverse plane by application of an RF pulse, its precessional motion results in a time-varying magnetization in the transverse plane. The oscillating transverse magnetization M_T produces a changing magnetic flux which in turn induces current in a receiver coil placed along the object. The voltage induced around the RF coil can be expressed in terms of a volume integral of M_T ,

$$v(t) \propto \text{Re} \left[\int C(\mathbf{r}) M_T(\mathbf{r}) e^{-i\omega(\mathbf{r})t} d^3r \right]. \quad [1.6]$$

In Eq. [1.6], \mathbf{r} is the 3-dimensional spatial vector and $C(\mathbf{r})$ represents the spatially varying RF coil sensitivity. The complex signal, which is obtained by demodulating the voltage $v(t)$ with $\cos(\omega_0 t)$ and $\sin(\omega_0 t)$ (quadrature demodulation (32)), is given by

$$s(t) = \int C(\mathbf{r}) M_T(\mathbf{r}) e^{-i(\omega(\mathbf{r}) - \omega_0)t} d^3r. \quad [1.7]$$

The following paragraphs describe the two most basic MR experiments possible: the free induction decay (FID) and the spin echo. An understanding of the relaxation mechanism governing a given acquisition is crucial for a given application and the resulting contrast in MR images.

1.3.1.3.1 Free induction decay (FID)

After the application of a 90° RF pulse, spins in the transverse plane are subjected to small magnetic field irregularities of the sample. These irregularities can be caused by magnetic susceptibility differences among tissues composing the sample, especially near tissue interfaces with bone and air. In addition, the main magnetic field may not be perfectly uniform. The overall effect of these irregularities is the variation of the spins' precession frequencies across the sample. This frequency dispersion causes the transverse magnetization to decay faster at a rate determined by the new parameter T_2^* , given by

$$\frac{1}{T_2^*} = \frac{1}{T_2} + \frac{1}{T_2'}, \quad [1.8]$$

where T_2' is the parameter reflecting the local magnetic environment of the sample. The transverse decay given by Eq. [1.5] is now governed by T_2^* . For an FID experiment with

a repetitive excitation by a 90° RF pulse with an interval TR (repetition time) between the excitations, the received signal at steady state is given by

$$s(t) \propto \rho \left(1 - e^{-\frac{TR}{T_1}}\right) e^{-\frac{t}{T_2}}. \quad [1.9]$$

1.3.1.3.2 Spin echo

While T_2' effects dominate every decay curve, there is a possibility of recovering a point in the MR signal with a pure T_2 . This process is instigated by a 180° RF refocusing pulse at some time $TE/2$ after the 90° excitation pulse. This RF refocusing pulse causes the dephasing spins to reverse direction and rewind back through the magnetic environment. At a time point TE (echo time) after the excitation pulse, the magnetization will have recovered completely by T_2' effects but not by T_2 . This process of recalling the magnetization is called spin echo. The steady state received signal for a repetitive spin echo experiment is given by

$$s(t) \propto \rho \left(1 - e^{-\frac{TR}{T_1}}\right) e^{-\frac{TE}{T_2}}. \quad [1.10]$$

1.3.2 Review of MR Imaging

The previous section was devoted to a basic understanding of MR signal generation without much regard how an image is created from the available signal. This section describes how the proton spin system, and subsequently the MR signal, is manipulated in order to produce an MR image.

The traditional diffraction methods to resolve an object within the image cannot be applied to MR signal due to its long wavelength (e.g. 5 m in vacuum at 1.5 Tesla). In MRI, spatial information is encoded into the MR signal prior to acquisition, and the image is reconstructed by properly decoding the spatially encoded MR signal. Substituting Eq. [1.1] and Eq. [1.2] into Eq. [17] and taking into account the dependence of the net magnetization, the external magnetic field, the spin density, and the flip angle on the spatial position, the MR signal can be expressed as

$$s(t) = \frac{\gamma^2 \hbar^2}{4kT_s} \int C(\mathbf{r}) \sin(\alpha(\mathbf{r})) B(\mathbf{r}) e^{-i\gamma(B(\mathbf{r}) - B_0)t} \rho(\mathbf{r}) d^3r. \quad [1.11]$$

where $B(\mathbf{r})$ is the external magnetic field consisting of the sum of the constant term B_0 and a spatial varying component. In Eq. [1.11], the signal modulation by T_2 or T_2^* relaxation is intentionally neglected. Eq. [1.11] contains four spatially dependent functions: the desired spin density, $\rho(\mathbf{r})$, and the other three function, $C(\mathbf{r})$, $\alpha(\mathbf{r})$, and $B(\mathbf{r})$ that can be known *a priori*. These three functions represent spatial encoding at three distinct stages of an MRI experiment: First, the RF pulse provides an excitation pattern, $\alpha(\mathbf{r})$, which localizes the spins to be imaged; Second, the magnetic field, $B(\mathbf{r})$, dictates the phase evolution of the selected spins; Last, the coil sensitivity, $C(\mathbf{r})$, weights the localized spins.

The following sub-sections describe the encoding and decoding methodologies as are performed in existing conventional and parallel MRI techniques.

1.3.2.1 Spatial encoding using RF excitation profile

Localizing the spins prior to imaging is an important step in MRI acquisition. It may help select only a “region of interest” and therefore provides a speed advantage (a smaller volume of tissue can be imaged much faster at a given resolution than a larger extended sample). It also provides the flexibility to MRI to conform to the acquisition procedure (e.g. acquisition in slice) of other modalities such as Computed Tomography (CT) and Positron Emission Tomography (PET).

The localization of the spins can be selective or non-selective. For selective localization, only the spins contained within the selected slice or volume will be interrogated by the imaging sequence. The slice profile is established by creating a linear magnetic field gradient across the sample. The external magnetic field experiencing a linear spatial perturbation can be expressed as the sum of the static component B_0 and the linear magnetic field gradient $G(r)$ given by

$$B(\mathbf{r}) = B_0 + G(\mathbf{r}), \quad G(\mathbf{r}) = \vec{\mathbf{G}}\mathbf{r}. \quad [1.12]$$

Spins experience a slightly different local magnetic field based on their location in the slice gradient. Spins within a certain bandwidth of Larmor frequencies that match the bandwidth of the RF pulse are excited. Slice profiles and RF pulse shapes have an approximate Fourier relationship, so that in order to acquire a rectangular slice, a sinc-shaped RF pulse is required. This localization technique may result to a FID or spin echo signal. Complex volume shapes can also be selected but requires longer RF pulse excitations.

In non-selective localization, all spins falling in the area of sensitivity of the RF and whose resonance frequencies are within the RF excitation bandwidth will be excited. A rectangular shaped RF pulse is required in this case.

1.3.2.2 Spatial encoding using magnetic field gradients

To image the selected volume, conventional MRI relies on the gradient fields for spatial encoding in the remaining spatial directions. The Larmor frequency of a spin is linearly proportional to its position when the static field is augmented with a linearly varying field. This use of a gradient to establish a relationship between the spins along some direction and their precessional rates is referred to as *frequency encoding* along that direction. Assuming that a uniform RF excitation pulse is applied to localize the spins and rotated the magnetization at a flip angle $\alpha(r) = \alpha_0$ and that the coil sensitivity $C(r)$ is combined with the spin density $\rho(r)$ to form the coil-weighted spin density $\rho_c(r)$, Eqs. [1.1], [1.11], and [1.12] can be combined to yield the simplified MR signal equation given by

$$s(t) = \frac{\gamma^2 \hbar^2}{4kT_s} \sin(\alpha_0) B_0 \int e^{-i\gamma G(r)t} \rho_c(\mathbf{r}) d^3 r. \quad [1.13]$$

To obtain Eq. [1.13], the fact that B_0 is typically several orders of magnitude greater than $G(r)$ has been taken into account.

1.3.2.2.1 *k-space and elements of a pulse sequence*

By considering that the field gradient \vec{G} is time-dependent, the phase evolution (due to spin dephasing) over time can be expressed in terms of $\mathbf{k} \cdot \mathbf{r}$ where the vector \mathbf{k} is defined as

$$\mathbf{k} = -\gamma \int_0^{\tau} \vec{G}(t) dt . \quad [1.14]$$

Substituting Eq. [1.14] into Eq. [1.13], the later simplifies to

$$s(\mathbf{k}) = \frac{\gamma^2 \hbar^2}{4kT_s} \sin(\alpha_0) B_0 \int e^{-i\mathbf{k}\cdot\mathbf{r}} \rho_c(\mathbf{r}) d^3r . \quad [1.15]$$

This data space is called k -space (Figure 2b). The spatial encoding functions in Eq. [1.15] are given by

$$E_{\mathbf{k}}(\mathbf{r}) = \beta e^{-i\mathbf{k}\cdot\mathbf{r}} . \quad [1.16]$$

where β is a scalar accounting for the constants outside of the integral of Eq. [1.15]. $E_{\mathbf{k}}$ are Fourier basis functions, and hence this method of spatial encoding is commonly called Fourier encoding.

Encoding is generally accomplished in two steps: point-wise then continuously. In point-wise encoding, gradients are turned on for a short period of time to dephase the spins in the sample. During that time, the spins' phases, represented by $\mathbf{k}\cdot\mathbf{r}$, evolve over time depending their spatial position. This is referred to as phase encoding. The process of turning on the gradient for a short time is equivalent to moving the k -space position away from the center k -space ($\mathbf{k} = 0$) along one direction (phase encoding direction). After a phase encoding step, the signal is continuously sampled with a gradient turned on in the readout direction (frequency encoding direction). This continuous sampling collects an entire line of k -space in one acquisition. The gradient activity as a function of time on each orthogonal axis is typically represented, along with RF activity, in a pulse sequence diagram (Figure 2a).

Although $\rho_c(r)$ is a continuous function, the discretization of the k -space and therefore the continuous position vector r can be applied to $\rho_c(r)$ resulting to a matrix formulation of Eq. [1.15] as

$$\mathbf{s} = \mathbf{E}\boldsymbol{\rho}_c. \quad [1.17]$$

The encoding matrix E contains the Fourier basis embedding the effects of gradient encoding. The elements in the signal vector s are Fourier components of the coil-weighted spin density ρ_c evaluated at the corresponding k -space locations k . An image is reconstructed by applying an inverse Fourier transformation on the acquired dataset. In the special cases of rectilinearly sampled k -space trajectories, the fast Fourier transformation (FFT) algorithm can be applied. Additionally, the Fourier transformation is a unitary transformation that provides an optimal noise averaging benefit. Here, the reconstruction is efficiently accomplished without an explicit effort of determining E , computing E^{-1} .

For non-rectilinearly sampled (non-Cartesian) trajectories, the non-uniform sampling density across k -space prevents using a straightforward inverse Fourier transform to reconstruct the image (33). Rather, gridding (34) is first performed to interpolate the data onto a Cartesian grid before the application of the inverse Fourier transform.

1.3.2.2.2 *Field of view and spatial resolution*

A rectilinear sampling of the k -space trajectories with an infinite impulse chain (i.e. $k = \pm n\Delta k$, $n = 0, 1, 2, \dots, \infty$) results to a periodic replication of the object in the image

domain. If the object is of finite length L and the sampling interval in k -space satisfies the Nyquist criterion for $\Delta k \leq 2\pi/L$, then the object can be fully reconstructed without aliasing. The maximum k -space sampling interval, Δk , that allows reconstruction without aliasing defines the field of view (FOV), which is given by

$$FOV = \frac{2\pi}{\Delta k}. \quad [1.18]$$

In practice, the k -space trajectories are sampled with a finite impulse chain (i.e. $k = \pm n\Delta k$, and $abs(k) \leq k_{max}$). In this case, the voxels reconstructed by discrete Fourier representation are no longer ideal delta functions. Instead, they are sinc functions with zero crossings at integral multiples of π/k_{max} , which typically defines the image pixel size,

$$Pixel\ Size = \frac{\pi}{k_{max}}. \quad [1.19]$$

1.3.2.2.3 Traditional strategies for accelerated acquisition

The sequential encoding of MR signal as described in section 1.3.2.2.1 imposes a significant time penalty in MRI. To give a feeling for the time this process takes, the acquisition of an image with resolution 256×256 acquired with a repetition time (TR) of several hundred milliseconds requires a total time of several minutes. Imaging times of this length have obvious implications. The subject is liable to move during imaging causing artifacts in the images, and dynamic processes changing on a time scale shorter than this are difficult to capture.

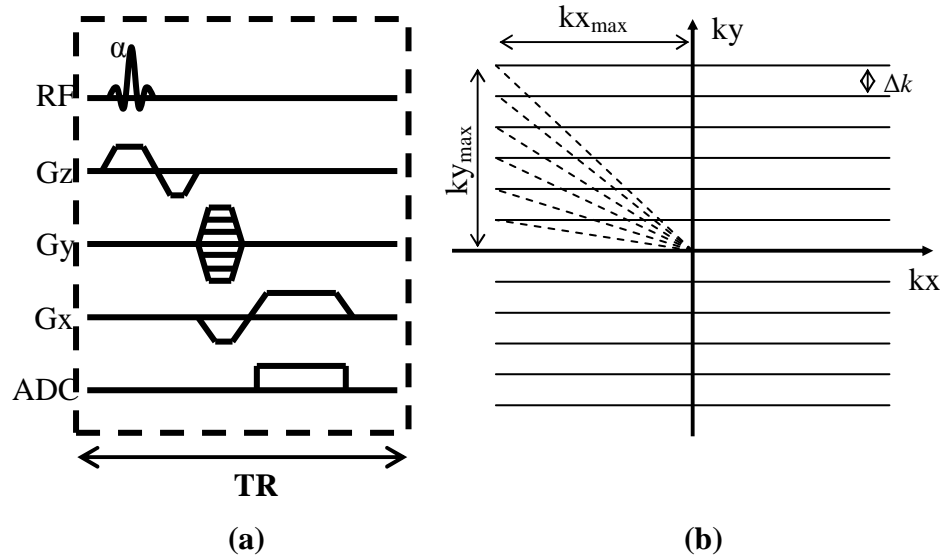


Figure 1.2 Elements of a pulse sequence and k -space

(a) Pulse sequence diagram describing the sequence events involved in the three stages of spatial encoding in conventional MRI. The first action is the RF excitation along with the G_z gradient (first lobe) that select a slice, followed by the refocusing of the slice select gradient (2nd lobe of G_z). The next stage is phase encoding (G_y gradient) and readout pre-phasing gradient (first G_x gradient lobe) that dictate the phase evolution. Finally the frequency-encoding gradient (G_x) is applied while the signal is acquired (ADC). In order to fully encode an image, this sequence is repeated (at time intervals of TR) for different amplitudes of the phase encoding gradient. (b) A schematic representation of k -space. When the phase encoding gradient is zero the pre-winding gradient takes us to the left of k -space and the readout line in k -space along the phase encode direction by an amount Δk . The magnitude of Δk is inversely proportional to the field of view (FOV) and the maximum extent of k -space is inversely proportional to the voxel size.

Many acquisition strategies have been proposed to accelerate MR scans. Minimization of TR by increasing gradient strength can lead to accelerated imaging (e.g. (35)). Although fast acquisitions can be done in this way, limits are quickly reached because of instrumentation cost and human tolerance. Indeed, increasing gradient strength requires more powerful amplifiers and gradient coils capable of taking the increased current and voltage, which adds significantly to the cost of the scanner. More importantly, physiological limits associated with the rate of switching of such gradients

are eventually reached. Exposing the human nervous system to a time dependent magnetic field may lead to spontaneous nerve firing ((36,37)) known as peripheral nerve stimulation (PNS).

An approach that has attracted widespread use due to its favorable temporal properties is to acquire more than one phase encode lines per TR. This approach has led to a family of sequences called echo train imaging that includes echo planar imaging (EPI) (28) and spiral imaging (19). However, such sequences compromise both contrast and resolution, and in some cases, lead to image distortion.

Another strategy is to reduce the field of view without aliasing, which can be done by localizing the region of excitation (38,39). Unfortunately, complex spatial localization often requires long radio frequency (RF) pulse trains and if the RF pulse length is long compared to the relaxation times of the sample being imaged, then the region of excitation will be ill defined.

Partial Fourier imaging (40-42) is another solution. It exploits the theoretical conjugate symmetry of k -space with part of k -space remaining uncollected and then repopulated using various methods. For dynamic imaging where multiple time point images are acquired, there are many methods that improve the temporal resolution by updating different parts of k -space at different frequencies (more often at the center than edges (43)).

The improvements in MR image acquisition speed over the past two decades have allowed significant advances in the visualization and characterization of moving structures. While this is a significant accomplishment, conventional MRI has more or less reached its imaging speed limit imposed by safety guidelines regarding magnetic field gradient switching rate and RF power deposition. In the next section, a safe alternative strategy to accelerate image acquisition is introduced: coil encoding.

1.3.2.3 Spatial encoding using RF receiver coil sensitivities

To image the localized spins, parallel MRI relies on field gradients and the sensitivities of an array of receiver coils for spatial encoding. The spatial encoding resulting from the variations in sensitivities of receiving RF coils is used to reduce the number of gradient encoding steps necessary for a conventional MRI acquisition procedure. By analogy to Eq. [1.15], the MR signal received in individual coil elements can be expressed as

$$s_l(\mathbf{k}) = \frac{\gamma^2 \hbar^2}{4kT_s} \sin(\alpha_0) B_0 \int e^{-i\mathbf{k}\cdot\mathbf{r}} C_l(\mathbf{r}) \rho(\mathbf{r}) d^3r . \quad [1.20]$$

where $s_l(\mathbf{k})$ represents the MR signal received by the l^{th} coil with spatial sensitivity $C_l(\mathbf{r})$. Here, the MR signal is encoded by hybrid encoding functions of magnetic field gradients and the coil sensitivities given by

$$E_{\mathbf{k},l}(\mathbf{r}) = \beta C_l(\mathbf{r}) e^{-i\mathbf{k}\cdot\mathbf{r}} . \quad [1.21]$$

The extra sub-index l as compared to Eq.[1.16] emphasizes that matrix that the number of encoding functions has increased by a factor equal to the number of array elements. Note that if the coil sensitivities can be combined such that the composite sensitivities form

spatial harmonics ($\approx e^{-im\Delta k \cdot r}$, where m is the harmonic number and Δk is the k -space sampling interval), then the hybrid encoding functions become Fourier basis and the reconstruction can benefit from the direct inverse Fourier transform as convention MRI reconstruction for rectilinear sampling trajectories. These spatial harmonics would represent redundant encoding functions. This means that some of the gradient encoding steps can be omitted without affecting the necessary overall encoding steps. Parallel MRI exploits this redundancy in spatial encoding to accelerate the acquisition. Encoding gradient steps may be omitted by a factor (“acceleration factor”) greater than one and less or equal to the number of array elements. In other words, the k -space trajectory only needs to traverse a subset of the original k -space locations, resulting in a proportionally faster acquisition.

1.3.2.3.1 Parallel MRI reconstruction methods

Phased array coil technology was originally developed to improve the intensity uniformity of MR images obtained using surface coils, while preserving their inherent gain of signal-to-noise ratio (SNR). The idea of using multiple RF receivers to accelerate MRI scans was first introduced in the late 1980s (44-46). Additional contributions in that effort were made in the early 1990s (47-49). However, the first successfully accelerated *in vivo* images were demonstrated in 1997 using the SiMultaneous Acquisition of Spatial Harmonic (SMASH) technique (2) following by the SENSitivity Encoding (SENSE) technique in 1999 (3).

Since the inception of SMASH and SENSE, various improvements and variations (4-9,15) have been developed. In all cases, the procedures involve an explicit determination of the encoding matrix E and its inverse E^{-1} , as opposed to conventional MRI. This is generally accomplished with two type of dataset: coil reference data and image data. The coil data is used to determine the encoding matrix E and the image is reconstructed by computing the inverse of E .

1.3.2.3.1.1 Sensitivity calibration

Calibration with coil sensitivity maps

As indicated in Eq. [1.21], knowing the coil sensitivities $C(r)$ is indispensable to determine the encoding matrix E . $C(r)$ can be theoretically calculated using Maxwell's Equations (or the Biot-Savart law for sufficiently low frequencies) in combination with the principle of reciprocity (50) if the coil array geometry and location are known. In practice, however, the performances of coils vary depending on the electromagnetic properties of the subject. As a consequence of the intimate interaction between coil and subject, coil sensitivity information is preferably recalibrated for each subject even for rigid and static coils. The coil sensitivities can be obtained from coil-weighted images obtained using conventional MRI acquisition and reconstruction methods (Eq. [1.17]). These coils images may have lower spatial resolution than the accelerated diagnostic images, but are required to have a sufficient FOV to satisfy the Nyquist criterion. To eliminate the spin density component, an additional image can be acquired at the same contrast using a birdcage body coil designed to have uniform RF spatial reception. A quotient is calculated between each of the array coil images and the birdcage coil image

to obtain a scaled version of the sensitivity of that coil. If a body-coil image is not available, a sum-of-squares combined images of all the array coil images can be used to divide out the spin density.

Calibration data can be obtained from a separate scan before or after the image acquisition. Because of the requirement of external information, this approach is generally known as external calibration. Alternatively, the calibration scan can be incorporated as a part of the image acquisition, and the calibration data can be extracted from the image dataset. This approach is called auto-calibration or self-calibration. The crucial difference between the external- and self-calibration approaches lies in the timing of the acquisition of calibration data relative to the image acquisition.

Calibration without coil sensitivity maps

Typically a self-calibration method, this method allows coil sensitivity calibration without explicitly reconstructing the calibration images. A fit can be performed to determine the coefficients (weights) relating the reference k -space data, referred as calibrating signals, to the main data acquired from all coils. These weights, implicitly containing the coils sensitivity information, are used to reconstruct the image. The calibrating signals can be collected separately or integrally to the acquisition. However, they occur within the same scan and therefore are referred to as auto-calibrating signals (ACS).

1.3.2.3.1.2 Solving the linear inverse problem

One distinguish feature between various parallel MRI reconstruction techniques currently available is the specific way of posing and solving the common generalized linear inverse problem $s = E\rho$. In this section, two major classes of parallel image reconstruction are discussed and allied methods are referenced in each case. The two classes are direct and indirect inversion reconstructions.

Direct inversion reconstruction

This approach appears in the case where the encoding matrix E is known and the reconstruction entails finding a matrix inverse E^{-1} such that $E^{-1}E = I$ and thus $\rho = E^{-1}s$, where I is an identity matrix. In general, the encoding matrix has full rank and more rows (i.e. encodings) than columns (i.e. pixels to resolve), i.e E is over-determined. As a result, the Moore-Penrose pseudo-inverse is generally used to provide a least squares solution. To take into account possible differences in noise levels and the correlation between different coil channels, the receiver noise matrix Ψ is included in the reconstruction:

$$\rho = (E^H \Psi^{-1} E)^{-1} E^H \Psi^{-1} s, \quad [1.22]$$

where the superscript $(\cdot)^H$ denotes Hermitian conjugation. SENSE (3) is a notable representative of this approach. In SENSE, both the coil reference data and the undersampled data are operated in the image domain.

Block-by-block inversion performed through matrix diagonalization is a variant to the direct inversion strategy. Since the coil sensitivities are in general band-limited, by

Fourier transforming the encoding matrix E along the fully sampled dimension, the resulting encoding matrix, E_{FT} , in that hybrid space is approximately band-diagonal. An inverse $(E_{FT})^{-1}_{block-diag}$ can be determined efficiently by applying block-by-block inversion. E^{-1} is obtained by performing another Fourier transformation of $(E_{FT})^{-1}_{block-diag}$. g-SMASH (9) and Space-RIP (4) are representative of this approach. In g-SMASH, the reconstruction is performed with the coil data in k -space and this constitutes the main difference with SPACE-RIP in which the coil data are kept in the image domain. While this block-by-block inversion provides a numerical stability and computation efficiency advantage over the full matrix inversion, it makes the inversion inexact, $E^{-1}E \approx I$.

By allowing for more general sampling schemes, where every pixel of the undersampled image may potentially alias with all the others, higher computational costs are incurred with direct inversion as it becomes necessary to invert larger matrices. However, while it may be numerically unstable and computationally intensive to calculate the pseudo-inverse, the direct inverse reconstruction has the appeal of a theoretically exact solution. Various regularization techniques (14) have been effectively utilized to mitigate the instability of this reconstruction strategy. With direct inversion, however, an explicit determination of the coil sensitivity maps is required and in cases where obtaining precise coil sensitivity data may be difficult, the inversion can constrain the solutions to produce more benign errors in the final reconstructed image.

Indirect inversion reconstruction

The inverse problem can be solved without an explicit determination of E. Indeed, coil sensitivity is in general band-limited in k -space. The effect of multiplication of the imaged object by these coil sensitivities is therefore a finite-kernel convolution in k -space. The original Fourier components of the object of interest are locally spread in the acquired data. The indirect inversion approach estimates the missing datum by linearly interpolating a few local k -space data. This procedure in its simplified form is represented by

$$s(\mathbf{k} + m\Delta\mathbf{k}) = \sum_l w_l^m s_l(\mathbf{k}), \quad [1.23]$$

where $s_l(\mathbf{k})$ represents the acquired signal at the location \mathbf{k} received in the coil l , $s(\mathbf{k} + m\Delta\mathbf{k})$ is the reconstructed signal at the location $(\mathbf{k} + m\Delta\mathbf{k})$, $\Delta\mathbf{k}$ is the sampling interval along \mathbf{k} . For the m^{th} spatial harmonic (or the number of $\Delta\mathbf{k}$ offset of the missing line from the nearby acquired lines, counting according to an originally defined direction), w_l^m is the interpolation weight associated to $s_l(\mathbf{k})$. For Cartesian sampled k -space, the interpolation weights are assumed to be shift invariant in the entire k -space, providing a significant computational efficiency to the indirect inversion strategy. Notable representatives of this strategy include SMASH (2), AUTO-SMASH (51), VD-SMASH (52), and GRAPPA (8).

In SMASH, an explicit estimate of the coil sensitivity maps is required and the weights are derived by fitting the sensitivities to spatial harmonic as follows:

$$\sum_l w_l^m C_l(\mathbf{r}) = e^{-m\Delta\mathbf{k} \cdot \mathbf{r}}. \quad [1.24]$$

These weights are then used to combine the signals measured in each coil (Eq. [1.23]) and generate a composite signal at both sampled and originally omitted locations. This

approach only works well with a linear coil array and is not valid for general coil geometries.

AUTO-SMASH, VD-SMASH, and GRAPPA do not explicitly determine the sensitivity maps. Instead, the interpolation weights are obtained by fitting the auto-calibrating signals (ACS) to the main data acquired from all coils. A simplified representative of this process is given by

$$\sum_l s_l^{ACS}(\mathbf{k} + m\Delta\mathbf{k}) = \sum_l w_l^m s_l(\mathbf{k}). \quad [1.25]$$

The main differences between the implementation procedures of these three methods reside in the number of ACS used, the number of interpolated data per coil, and the way the composite final image is generated. GRAPPA, which is an improved version of SMASH, allows arbitrary coil geometries. A more detail description of its procedure is provided in chapter 2.

Although the indirect inversion approach provides the advantages of numerical stability and computational efficiency over the direct inversion strategy, the indirect inversion represents an approximate solution to the inverse problem. While the role played by regularization is explicit for direct inversion reconstruction, the conditioning of the indirect inversion reconstruction is largely implicit in the approximation made in the reconstruction. Regularization generally reduces noise at the expenses of increased artifact (53). Tradeoffs between inexactness (artifact) and numerical stability are important subjects of Chapters 2, 3, and 4.

For non-Cartesian sampled k -space, the interpolation weights can be dependent on the k -space location. As a result, the interpolation weights ideally need to be determined for each k -space point, which can lead to significant reconstruction time penalty. PARS (15) is a representative of the indirect inversion reconstruction for non-Cartesian sampled k -space. A strategy to alleviate the time penalty associate with the indirect inversion reconstruction of non-Cartesian undersampled k -space data is an important subject of Chapter 5.

1.3.2.3.2 Limits of parallel MRI

Parallel MRI is achieved at the cost of reduced signal-to-noise ratio (SNR). The reduction in SNR stems from two factors: the reduced number of data samples, and the instability in the reconstruction due to correlations in the spatial information as determined by the geometrical arrangement of the array coil. The first factor is intrinsic to parallel MRI philosophy, which is to acquire less k -space samples in order to reduce scan time, and is therefore inevitable. A strategy that mitigates this issue in some applications is discussed in Chapter 6. The second factor may be alleviated by optimizing coil geometry (54,55) or by improving the stability and accuracy of the reconstruction algorithm. The noise amplification, which occurs as a result of the reconstruction process, is generally quantified by the g-factor. Given this, the relationship between SNR of an undersampled MRI reconstructed image (SNR^{red}) and that of the same fully sampled reconstructed image (SNR^{full}) is given by

$$SNR^{red} = \frac{SNR^{full}}{g\sqrt{R}}, \quad [1.26]$$

where R is the acceleration factor. The g -factor depends on the spatial correlations between the coils and to some extent on the number of coils (3). It seems to increase abruptly if higher acceleration factors are attempted and so the g -factor is thought to represent an intrinsic limit to parallel MRI speed. In practice, the accelerator factor used is largely lower than the number of coil. This provides a vastly over-determined system of equations and therefore improves the numerical condition of the matrix inversion process.

1.3.2.3.3 Parallel transmit

Localizing the spins (as discussed in chapter 1.3.2.1) falling within a complex volume shape requires long RF pulse trains and if the pulse length is long compared to the relaxation times of the sample then the region of excitation will be ill defined. Parallel transmit is a recently introduced strategy inspired from parallel imaging technique which may now be making possible the excitation of complex volume within realistic time scales (56,57). An in-depth exposition on this topic is beyond the scope of this dissertation. Nonetheless, transmit encoding is a niche method.

1.4 General Summary

This chapter has briefly described basic principles pertinent to the understanding of parallel MRI in order to provide a platform for discussion of the following chapters. Challenges that still hinder some aspects of clinical and research applications of parallel MRI have been outlined. Chapters 2-6 are the main contributions of the thesis and are

designed to be individually self-contained. Chapter 2 establishes an accurate method for choosing the optimal reconstruction kernel that balances the conflicting demands between fit accuracy and stability in parallel MRI reconstruction in k -space. Along the same line, Chapter 3 introduces a simple and robust quantitative metric that can be used for multiple purposes including reconstruction performance assessment, comparison of reconstruction algorithms, and optimization of the tradeoff between artifact and SNR. Examples of the use of the metric to select reconstruction parameters in GRAPPA and TGRAPPA(18) are provided. Chapter 4 introduces a new strategy to improve reconstruction efficiency in real time dynamic parallel MRI. This strategy is based on an automatic passive tracking of the frame-to-frame coil sensitivity information change. Chapter 5 proposes an efficient method for non-Cartesian parallel MRI reconstruction, which is based on successive convolutions in k -space. Chapter 6 concludes the thesis by introducing a simple and convenient method for improving SNR in parallel DTI acquisition.

1.5 Chapter 1 References

1. Lauterbur PC. Image formation by induced local interactions. Examples employing nuclear magnetic resonance. *Nature* 1973;242:190.
2. Sodickson DK, Manning WJ. Simultaneous acquisition of spatial harmonics (SMASH): fast imaging with radiofrequency coil arrays. *Magn Reson Med* 1997;38(4):591-603.
3. Pruessmann KP, Weiger M, Scheidegger MB, Boesiger P. SENSE: sensitivity encoding for fast MRI. *Magn Reson Med* 1999;42(5):952-962.

4. Kyriakos WE, Panych LP, Kacher DF, Westin CF, Bao SM, Mulkern RV, Jolesz FA. Sensitivity profiles from an array of coils for encoding and reconstruction in parallel (SPACE RIP). *Magn Reson Med* 2000;44(2):301-308.
5. Griswold MA, Jakob PM, Nittka M, Goldfarb JW, Haase A. Partially parallel imaging with localized sensitivities (PILS). *Magn Reson Med* 2000;44(4):602-609.
6. McKenzie CA, Yeh EN, Sodickson DK. Improved spatial harmonic selection for SMASH image reconstructions. *Magn Reson Med* 2001;46(4):831-836.
7. Sodickson DK, McKenzie CA. A generalized approach to parallel magnetic resonance imaging. *Med Phys* 2001;28(8):1629-1643.
8. Griswold MA, Jakob PM, Heidemann RM, Nittka M, Jellus V, Wang J, Kiefer B, Haase A. Generalized autocalibrating partially parallel acquisitions (GRAPPA). *Magn Reson Med* 2002;47(6):1202-1210.
9. Bydder M, Larkman DJ, Hajnal JV. Generalized SMASH imaging. *Magn Reson Med* 2002;47(1):160-170.
10. Bloch F, Hanson WW, Packard ME. Nuclear induction. *Physical review* 1946;69(2):127.
11. Purcell EM, Torrey HC, Pound RV. Resonance absorption by nuclear magnetic moments in solid. *Physical review* 1946;69(1):37.
12. Manfield P, Grannell PK. NMR 'diffraction' in solids. *J Phys C: Solid State Phys* 1973;6:L422.
13. Larkman DJ, Nunes RG. Parallel magnetic resonance imaging. *Phys Med Biol* 2007;52(7):R15-55.

14. Hoge WS, Brooks DH, Madore B, Kyriakos WE. A tour of accelerated parallel MR imaging from a linear systems perspective. *Concepts in Magnetic Resonance Part A* 2005;27A(1):17-37.
15. Yeh EN, McKenzie CA, Ohliger MA, Sodickson DK. Parallel magnetic resonance imaging with adaptive radius in k -space (PARS): constrained image reconstruction using k -space locality in radiofrequency coil encoded data. *Magn Reson Med* 2005;53(6):1383-1392.
16. Nana R, Zhao T, Hu T. Automatic kernel selection for optimal GRAPPA reconstruction. 2007; Berlin. p 747.
17. Nana R, Zhao T, Heberlein K, Laconte SM, Hu X. Cross-validation-based kernel support selection for improved GRAPPA reconstruction. *Magn Reson Med* 2008;59(4):819-825.
18. Blaimer M, Kellman P, Griswold MA. Dynamic parallel MRI using the temporal GRAPPA-operator (TGRAPPA-Operator). 2007; Berlin.
19. Ahn CB, Kim JH, Cho ZH. High speed spiral-scan echo planar imaging. *IEEE Trans Med Imag* 1986;MI-5:2.
20. Kubo T, Horii M, Harada Y, Noguchi Y, Yutani Y, Ohashi H, Hachiya Y, Miyaoka H, Naruse S, Hirasawa Y. Radial-sequence magnetic resonance imaging in evaluation of acetabular labrum. *J Orthop Sci* 1999;4(5):328-332.
21. Pruessmann KP, Weiger M, Bornert P, Boesiger P. Advances in sensitivity encoding with arbitrary k -space trajectories. *Magn Reson Med* 2001;46(4):638-651.

22. Heberlein K, Hu X. Self-calibrated parallel spiral imaging. In: Proc of 2nd International Workshop on Parallel MRI, Zurich 2004:59.
23. Heidemann RM, Griswold MA, Seiberlich N, Kruger G, Kannengiesser SA, Kiefer B, Wiggins G, Wald LL, Jakob PM. Direct parallel image reconstructions for spiral trajectories using GRAPPA. *Magn Reson Med* 2006;56(2):317-326.
24. Samsonov AA, Block WF, Arunachalam A, Field AS. Advances in locally constrained k -space-based parallel MRI. *Magn Reson Med* 2006;55(2):431-438.
25. Ogawa S, Lee TM, Nayak AS, Glynn P. Oxygenation-sensitive contrast in magnetic resonance image of rodent brain at high magnetic fields. *Magn Reson Med* 1990;14(1):68-78.
26. Calamante F, Thomas DL, Pell GS, Wiersma J, Turner R. Measuring cerebral blood flow using magnetic resonance imaging techniques. *J Cereb Blood Flow Metab* 1999;19:701-735.
27. Basser PJ, Mattiello J, LeBihan D. MR diffusion tensor spectroscopy and imaging. *Biophys J* 1994;66(1):259-267.
28. Mansfield P, Maudsley AA, Baines T. Fast scan proton density imaging by NMR. *J Phys E: Scient Instrum* 1976;9:271.
29. Farzaneh F, Riederer SJ, Pelc NJ. Analysis of T2 limitations and off-resonance effects on spatial resolution and artifacts in echo-planar imaging. *Magn Reson Med* 1990;14(1):123-139.
30. Haacke EM, Brown RW, Thompson MR, Venkatesan R. *Magnetic Resonance Imaging: Physical Principles and Sequence Design*: Wiley & Sons; 1999.

31. Smith RC, Lange RC. Understanding magnetic resonance imaging. CRC Press LCC 1998.
32. Hoult DI, Chen CN, Sank VJ. Quadrature detection in the laboratory frame. Magn Reson Med 1984;1(3):339-353.
33. Pipe JG. Reconstructing MR images from undersampled data: data-weighting considerations. Magn Reson Med 2000;43(6):867-875.
34. Jackson JI, Meyer CH, Nishimura DG, Macovski A. Selection of a Convolution Function for Fourier Inversion Using Gridding. Ieee T Med Imaging 1991;10(3):473-478.
35. Hasse A, Frahm D, Mattaei. Flashing imaging: rapid NMR imaging using low flip angle pulses. J Magn Reson 1989;67:388-397.
36. Schaefer DJ, Bourland JD, Nyenhuis JA. Reviews of patient safety in time-varying gradient fields. J Magn Reson Imaging 2000;12:20-29.
37. Nyenhuis JA, Bourland JD, Kildishev AV, Schaefer DJ, editors. Health effects and safety of intense MRI gradient fields. 1st Edition ed. Cleveland: CRC Press; 2001. 31-52 p.
38. Hardy CJ, Cline HE. Spatial localization in two dimensions using NMR designer pulses. J Magn Reson 1989;82:647-654.
39. Pauly JM, Nishimura DG, Macovski A. A k -space analysis of small-tip-angle excitation. J Magn Reson 1989;81:43-56.
40. Haacke EM, Lindskog ED, Lin W. A fast, iterative partial Fourier technique capable of local phase recovery. J Magn Reson 1991;92:126.

41. Liang ZP, Boada FE, Constable RT, Haacke EM, Lauterbur PC, Smith MR. Constrained reconstruction methods in MR imaging. *Reviews of Magn Reson Med* 1992;4:67.
42. Margosian P, Schmitt F, Purdy DE. Faster MR imaging: imaging with half the data. *Health Care Instrum* 1986;1:195.
43. van Vaals JJ, Brummer ME, Dixon WT, Tuithof HH, Engels H, Nelson RC, Gerety BM, Chezmar JL, den Boer JA. 'Keyhole' method for accelerating imaging of contrast agent uptake. *J Magn Reson Imaging* 1993;3:671-675.
44. Carlson JW. An algorithm for NMR imaging reconstruction based on multiple Rf receiver coils. *J Magn Reson* 1987;74:376-380.
45. Hutchinson M, Raff U. Fast MRI data acquisition using multiple detectors. *Magn Reson Med* 1988;6(1):87-91.
46. Kelton JR, Magin RL, Wright SM. An algorithm for rapid image acquisition using multiple receiver coils. In: *Proc of 8h Annual Meeting SMRM, Amsterdam* 1989:1172.
47. Kwiat D, Einav S, Navon G. A decoupled coil detector array for fast image acquisition in magnetic resonance imaging. *Med Phys* 1991;18(2):251-265.
48. Carlson JW, Minemura T. Imaging time reduction through multiple receiver coil data acquisition and image reconstruction. *Magn Reson Med* 1993;29(5):681-687.
49. Ra JB, Rim CY. Fast imaging using subencoding data sets from multiple detectors. *Magn Reson Med* 1993;30(1):142-145.

50. Hoult DI, Chen CN, Sank VJ. The field dependence of NMR imaging. II. Arguments concerning an optimal field strength. *Magn Reson Med* 1986;3(5):730-746.
51. Jakob PM, Griswold MA, Edelman RR, Sodickson DK. AUTO-SMASH: a self-calibrating technique for SMASH imaging. *SiMultaneous Acquisition of Spatial Harmonics*. *Magma* 1998;7(1):42-54.
52. Heidemann RM, Griswold MA, Haase A, Jakob PM. VD-AUTO-SMASH imaging. *Magn Reson Med* 2001;45(6):1066-1074.
53. Qu P, Wang C, Shen GX. Discrepancy-based adaptive regularization for GRAPPA reconstruction. *J Magn Reson Imaging* 2006;24(1):248-255.
54. Weiger M, Pruessmann KP, Leussler C, Roschmann P, Boesiger P. Specific coil design for SENSE: a six-element cardiac array. *Magn Reson Med* 2001;45(3):495-504.
55. de Zwart JA, Ledden PJ, Kellman P, van Gelderen P, Duyn JH. Design of a SENSE-optimized high-sensitivity MRI receive coil for brain imaging. *Magn Reson Med* 2002;47(6):1218-1227.
56. Katscher U, Bornert P, Leussler C, van den Brink JS. Transmit SENSE. *Magn Reson Med* 2003;49(1):144-150.
57. Zhu Y. Parallel excitation with an array of transmit coils. *Magn Reson Med* 2004;51(4):775-784.

CHAPTER 2. CROSS-VALIDATION-BASED KERNEL SUPPORT SELECTION FOR IMPROVED PARALLEL MRI RECONSTRUCTION IN k -SPACE⁴

This chapter introduces a cross-validation based method for selecting the reconstruction kernel that balances between the conflicting demands of fit accuracy and stability in simply k -space based parallel MRI reconstruction. The result is an optimized tradeoff between artifacts and noise. The development presented here is based on GRAPPA reconstruction algorithm although it can be readily extended to other reconstruction methods. As demonstrated with experimental data, the method improves image reconstruction with GRAPPA. Because the method is simple and applied in post-processing, it can be used with GRAPPA routinely.

2.1 Introduction

In parallel MRI employing indirect inversion reconstruction (1-9), the missing k -space data are estimated by interpolation between the measured k -space data points. The interpolation kernel (or matrix) for each coil can be determined for a given acquisition

⁴ The work in this chapter has been published as “Nana R, Zhao T, Heberlein K, Laconte SM, Hu X. *Cross-validation-based Kernel Support Selection for Improved GRAPPA Reconstruction*. Magn Reson Med 2008; 59(4):819-825”

scheme if coil sensitivity maps are known (10). With the generalized auto-calibrating partially parallel acquisition (GRAPPA) technique (8), the interpolation kernel is estimated using calibration lines by assuming a small kernel size and k -space invariance of the kernel. A recent extension of GRAPPA includes k -space data in the readout direction in the interpolation to improve reconstruction (11).

The GRAPPA procedure can be viewed as a special case of k -space interpolation in which a truncated version of the interpolation kernel support is used. The kernel weights are estimated through the least squares solution of a linear system of equations relating the acquired signals to auto-calibrating signal (ACS) lines. It can be inferred from this procedure that two main categories of error exist with the GRAPPA technique: model error and noise-related error. Model error has two components: one from using a limited number (as well as position) of ACS lines instead of the true coil sensitivity maps and the other from using a limited kernel size. Noise-related error arises from noise in the measured data and includes noise-induced errors that occur during kernel weights estimation, mainly due to the matrix inversion process (inversion error (10)), and errors that result from the application of the weights to noisy measured data. It is well recognized that the number and position of ACS lines used in the parameter estimation and the size and shape (or configuration) of the GRAPPA reconstruction kernel support significantly affect the reconstruction quality available with GRAPPA (12). For a given data set, the error due to the use of limited ACS line is predefined (i.e. the number and position of ACS lines are given) and only the kernel support can be varied to influence the model error and the noise-related error. As with any fitting approach, the model error

is expected to decrease with increasing kernel size while the noise-related error is expected to increase with the kernel size. To date, the problem of how to choose a kernel support that optimizes the tradeoff between these errors has not been fully addressed. The choice of the kernel support has been shown to depend on the coil configuration, noise level in the acquired data, imaging FOV and orientation, and number and position of ACS lines (13). Therefore, GRAPPA implementations employing a fixed kernel support for all situations, as commonly used, are unlikely optimal.

Recently, a rank-revealing QR factorization was used to select the most linearly independent columns in the coefficient matrix of fit formed from alignment of ACS points and including a larger range of local acquired signals around each ACS point (13). In doing so, the kernel support shape (or configuration) that minimizes the noise amplification during weights estimation is automatically selected whereas the kernel size is intuitively chosen as in common implementation of GRAPPA. Unfortunately, this strategy only focuses on minimizing error in the inversion process without taking into account other errors. A more general strategy that considers all types of errors is therefore of interest.

This work presents a method based on cross-validation (CV) (14) for selecting the optimal kernel support in GRAPPA reconstruction. In this method, the GRAPPA kernel selection problem is framed as a model selection problem and cross-validation is used for selecting a regression model among a group of candidate models. Unlike other methods such as Akaike (15), cross-validation does not rely on specific statistical properties of the

data or models being used (16). For a given accelerated data set, our method automatically selects the kernel support in GRAPPA reconstruction that minimizes the CV error and therefore provides an optimal compromise between the model error and error arising from noise, i.e. a tradeoff between bias and variance. Computer simulations and experimental results are provided to demonstrate that a minimum exists in the CV error as a function of kernel size for several acquisition schemes. The effectiveness of CV-selected kernel support in image reconstruction is evaluated with experimental data.

2.2 Methods

2.2.1 Review of GRAPPA

For simplicity, the following description assumes 2-dimensional sampling on a rectilinear grid although it can be readily generalized to the 3-dimensional case. In GRAPPA, data acquired in both phase (k_y) and frequency (k_x) encoding directions from all coils are interpolated to estimate the missing data for each coil, and images of the individual coils are reconstructed and combined, often using the square root of the sum of the squares, to derive the final image. Following the terminology used by others (11), we define a block to consist of one acquired line of data and the neighboring $R-1$ missing lines (R is the acceleration factor) along the accelerated direction (k_y). The fitting process, as shown in Figure 2.1, can be represented mathematically by (11),

$$S_j(k_y + r\Delta k_y, k_x) = \sum_{l=1}^L \sum_{b=-N_b}^{N_a} \sum_{h=-H_l}^{H_r} W_{j,r}(l, b, h) \times S_l(k_y + bR\Delta k_y, k_x + h\Delta k_x), \quad [2.1]$$

where S represents the k -space signal, (k_x, k_y) is the k -space coordinate, and Δk_y and Δk_x are the sampling intervals along k_y and k_x , respectively. In Eq. (1), j and l represents the

coil number, r ($r \leq R$) is the number of Δk_y offset of the missing datum in a block, N_a and N_b are the number of blocks before and after the current block to which the missing data belongs, H_l and H_r are the number of left and right neighboring columns, respectively, used in the reconstruction, L is the number of coils in the array, and $W_{j,r}$ refers to the weights of the r -th line of coil j .

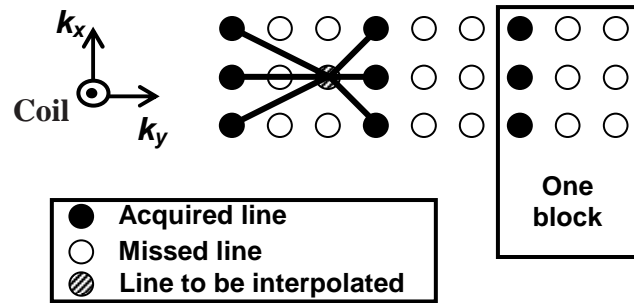


Figure 2.1 GRAPPA fitting procedure

Acquired data from multiple blocks (along k_y), multiple columns (along k_x), and from all coils are used to fit a single missing datum

The weights are obtained by solving the above equation in which the signals of the left side are replaced by ACS lines. The equation can be formulated as a least-squares problem in the matrix notation,

$$\mathbf{Ax} = \mathbf{b}, \quad [2.2]$$

where \mathbf{b} is the vector formed from vertical concatenation of the ACS points recorded by the individual coils, \mathbf{x} is the vector of kernel weights, and matrix \mathbf{A} consists of the vertical columns of the acquired data used to predict each ACS point with the kernel weights. For a given data set, the choice of kernel support dictates the tradeoff between the bias and noise (12). Therefore, a kernel support that minimizes reconstruction error, thereby resulting in an optimal tradeoff between SNR and artifact, is desired.

2.2.2 Cross-validation in GRAPPA reconstruction

In our implementation of CV for kernel support selection in GRAPPA, the available samples (ACS blocks) are divided into K disjoint partitions of approximately equal size (referred here as K -fold cross-validation), as illustrated in the example in Figure 2.2 for an outer reduction factor (ORF) of 3. Note that in the example, one partition corresponds to one block although in general, depending on the value of K , a partition may consist of several blocks. Weights for each of the possible kernel supports are determined K times, each time using a different combination of $K-1$ partitions, and the prediction error is calculated, K times, by predicting the data for the partition left out (note that only the lines that would be omitted in a truly accelerated acquisition are predicted) and comparing with the corresponding measurement of the partition. The cross-validation error (ϵ_{CV}) for a given kernel support is simply the average of the K prediction errors given by

$$\epsilon_{CV} = \frac{1}{K} \sum_{j=1}^K \frac{1}{N_j} \sum_{i \in S_j} (b_j - A_j * x_j)^2, \quad [2.3]$$

where x_j , b_j , and A_j are the estimated weights, the testing data (i.e., the measured set of ACS lines left out), and the encoding matrix, respectively, at the j th step in the partitioning. S_j is the j th subset of the samples and N_j is the number of elements in that subset. The case where K is equal to the number of ACS blocks is known as the leave-one-out cross-validation. For this work, leave-one-out cross-validation is used. For simplicity of illustrating the concepts of our method, we did not use other values of K in this work.

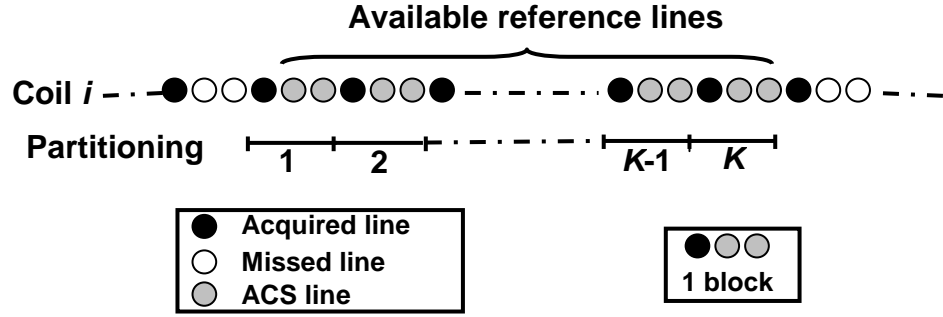


Figure 2.2 Cross-validation re-sampling strategy used for kernel support selection

The available ACS blocks are divided into K disjoint partitions of approximately equal size. In this example, an acquisition scheme with acceleration factor of 3 is illustrated. Weights for each of the possible kernel supports are determined K times, each time using a different combination of $K-1$ partitions, and the prediction error is calculated, K times, by predicting the data for the partition left out and comparing with the corresponding measurement of the partition. The cross-validation error (ϵ_{CV}) for a given kernel support is simply the average of the K prediction errors.

2.2.3 Selection of kernel support

For a given number of kernel support points, say $i \times j$ (i along k_y and j along k_x), there are a number of kernel shapes (configurations) to be considered. An exhaustive search of all possible number of support points and their corresponding configurations would require a large number of kernels to be examined and be computationally impractical. For example, with a matrix size of 256×256 (as the one used in Figure 2.7) accelerated with an ORF of 2, even the smallest kernel size (1×1) would have $128 \times 256 = 32768$ configurations. Here we only examine rectangular kernels whose support is contiguous in the k -space, consisting of only acquired lines neighboring the missing datum (this restricted search has been termed k -space locality criterion (9)). In this case, either 1, 2 or 4 kernel support configurations were considered for each kernel size, depending the values of i and j ; the multiple configurations arose because when i is an odd number there are two possible configurations along the phase-encoding direction,

and when j is an even number there are two possible configurations along the readout direction. An example of kernel support consideration is illustrated in Figure 2.3 for a 2×2 kernel and a 3×3 kernel. The examination process, as implemented in this study, starts from the minimum kernel size (1×1) and proceed iteratively to kernels that are incrementally expanded in each direction. The process stops when the maximum dimensions in each direction allowed by the data or user-defined limits are reached. In the cross-validation, ϵ_{CV} is computed for each of the kernels considered, and the kernel support that generates the overall minimum ϵ_{CV} is retained for GRAPPA reconstruction.

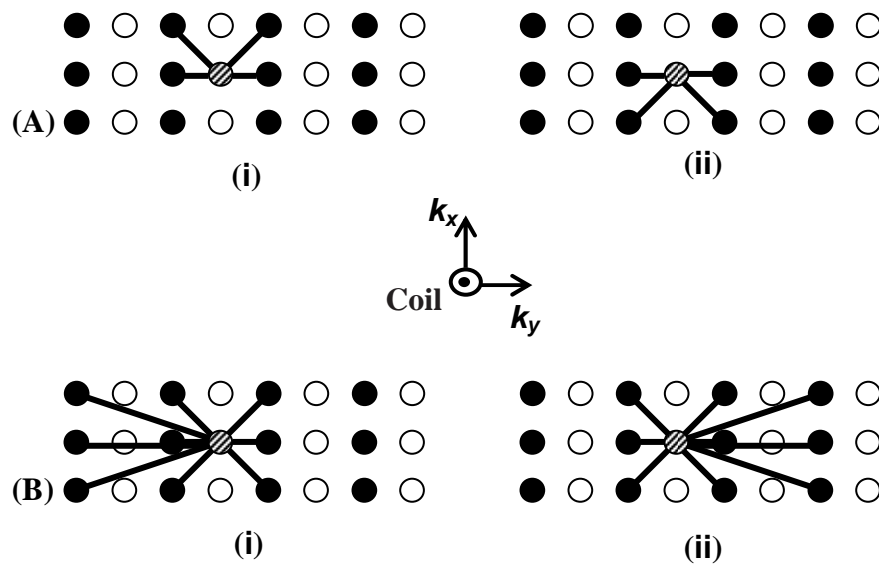


Figure 2.3 Configuration of the kernel supports to be examined by cross-validation

Examples for a kernel size of (A) 2×2 ($k_y \times k_x$) and (B) 3×3 considering only kernels consisting of only acquired lines neighboring the missing datum. For each of these kernel sizes, two possible configurations ((i) and (ii)) exist. In all cases, the shaded circle is the point to be interpolated. In this example, an acquisition scheme with acceleration factor of 2 is illustrated.

2.2.4 Computer simulation

Computer simulations were performed in Matlab (MathWorks, Natick, MA), using a standard Shepp-Logan phantom, to examine the cross-validation error as a function of kernel size for several acquisition schemes. Only kernel supports that were formed according to the k -space locality criterion were considered although it is expected that with each kernel size, the CV error may vary slightly also with the kernel support shape.

An eight-element coil was simulated by means of an analytical Biot-Savart integration (Figure 2.4). Each coil element had a circular loop shape and the elements are placed 45° apart (with no gaps in between coils) on a cylinder of 320 mm diameter and 300 mm in length. The 2D sensitivity map of each coil at the position $z = 0$ along the cylinder axis was applied to a 128×128 Shepp-Logan phantom of FOV $240 \times 240 \text{ mm}^2$ to generate the full versions of k -space data sets, which were later downsampled to emulate the parallel imaging acquisition. Gaussian noise was added to the raw data (both the undersampled data and the ACS data). The variance of the noise ($\delta = 10^{-4}$) chosen corresponded to an average SNR of 100. Here the average SNR is defined as the ratio of the mean intensity of the entire Shepp-Logan phantom to the variance of the noise. Different sets of ACS lines taken at the center of the k -space were considered for the fitting. Two different reconstruction strategies were performed on the same simulated data set and their performances were compared. The first is a standard GRAPPA reconstruction that uses a 4×5 fixed kernel support, where kernel support elements are

formed by considering the k -space locality criterion. The second is a GRAPPA reconstruction using CV selected kernel support.

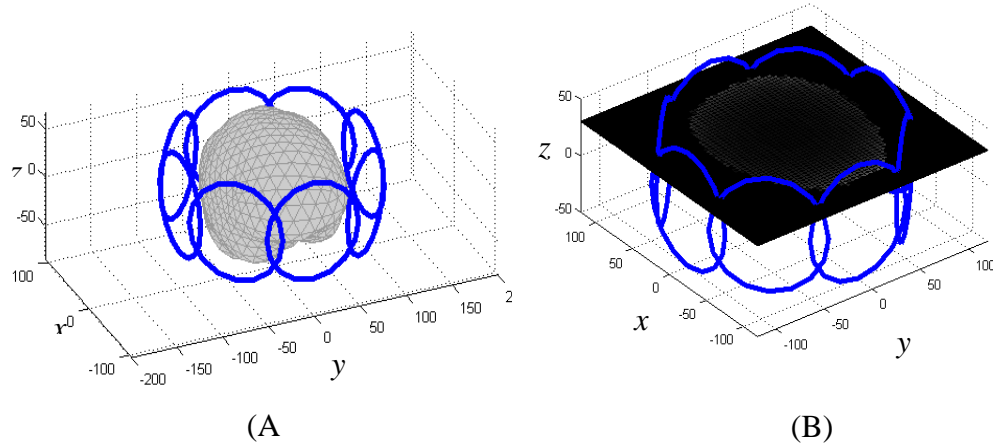


Figure 2.4 Sketch of the 8-element head array coil used to generate for simulation (A) indicating a brain mask within the array and (B) indicating the slicing procedure for axial imaging

2.2.5 Data acquisition and reconstruction

Two different sets of experimental data were acquired. Specifically we demonstrate our approach with 3 T anatomical brain data and 1.5 T dynamic cardiac imaging data. All data were collected with participants' written informed consent in accordance with institutional review board policies. The anatomical brain experiments were performed on a 3T Siemens Tim™ Trio whole-body MR scanner (Siemens Medical Solutions, Erlangen, Germany) with a 12-channel head matrix coil for reception and a volume body coil used as the transmit coil. Axial brain scans were acquired from healthy adult human volunteers using a gradient-echo sequence (TR = 300 ms, TE = 4 ms, flip angle = 80°, slice thickness = 5 mm, FOV = 256 mm, matrix = 256 × 256 × 12). The cardiac imaging data sets were acquired on a 1.5T Siemens Avanto with a 12-channel

cardiac matrix coil. Four-chamber view scans were acquired using a retrospectively gated segmented TrueFISP cine sequence in a single breath-hold (TR = 20.56 ms, TE = 1.09 ms, flip angle = 72°, slice thickness = 6 mm, FOV = 360 × 326.25 mm, matrix = 192 × 144 × 12). In both experiments, non-accelerated multi-coil data were collected and later downsampled to emulate the parallel imaging acquisition procedure. Three parallel imaging data sets were synthesized with ORFs of 2, 3, and 4, respectively. Different numbers of ACS lines were considered for each ORF.

Leave-one-out cross-validation was applied to undersampled data sets to identify their respective optimal kernel supports. GRAPPA was applied to each data set twice, once using its CV-derived optimal kernel support and another time with a common kernel support of 4 × 5. A quantitative assessment of the difference between the reconstructed images was performed by computing the reconstruction error defined by $\varepsilon = \sum_n^N |I(n) - I_{ref}(n)| / N$ where I represents the GRAPPA reconstructed image, I_{ref} is the full-data reconstructed image, N is the total number of pixels, and n is the pixel index. As in standard GRAPPA, ACS lines were included in the reconstruction of the final image. All algorithms were implemented in MATLAB (The Mathworks Inc., Natick MA, USA) on a Pentium 4 CPU 2.00 GHz computer with 1GB RAM.

2.3 Results

Figure 2.5 presents plots of cross-validation error of (A) Shepp-Logan phantom and (B) human brain data as a function of kernel size along the phase encoding direction

for $ORF = 2$, with 4, 8, and 12 ACS lines, respectively. The kernel size along the readout direction was fixed at one (similar to the original GRAPPA (8)) for simplicity as the purpose of the plot was to demonstrate the “U-shape” behavior of the CV error. A similar U-shape was seen when other kernel sizes along the readout direction were used. The plots in Figure 2.5A and Figure 2.5B have been scaled differently as their shapes are of more relevance here. In each figure, the three plots share the same trend: as the model complexity increases, the CV error decreases, reaches a minimum and then increases.

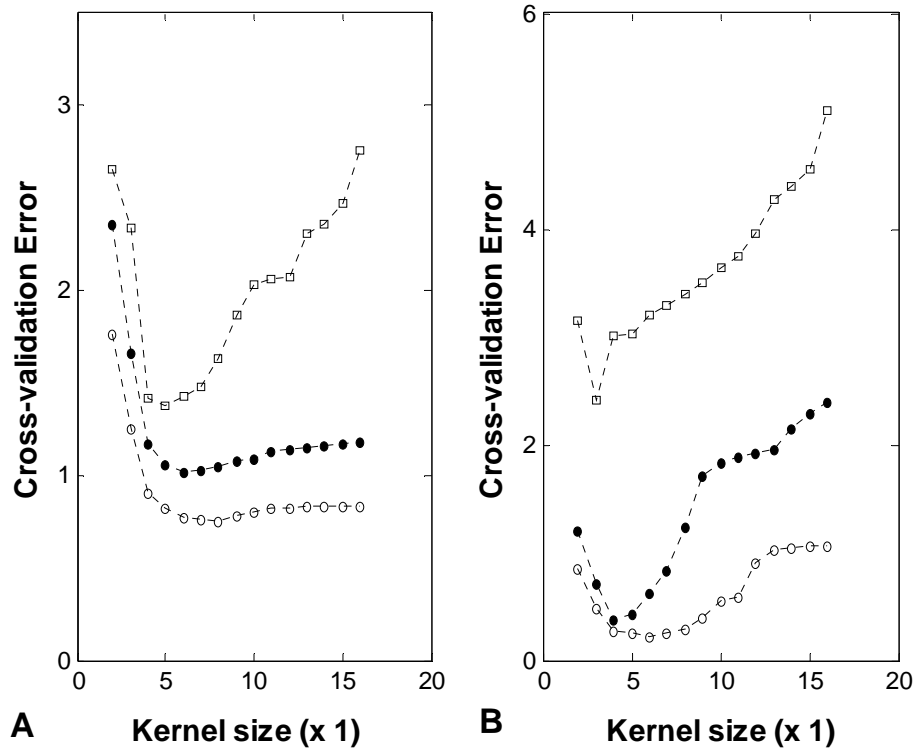


Figure 2.5 Simulated and experimental plots of cross-validation errors

(A) Shepp-Logan phantom and (B) human brain data vs. kernel size along the phase encoding for $OR = 2$. In all plots, squares indicate the use of 4 ACS lines, dark filled circles 8 ACS lines, and empty circles 12 ACS lines.

Phantom images reconstructed using GRAPPA with a fixed 4×5 kernel support and CV identified kernel support, with acceleration factors of 2 and 3 and a very limited number of ACS lines (2 for ORF = 2, and 6 for ORF =3) are presented in Figure 2.6B. The non-accelerated image is also shown in Figure 2.6A for comparison. The reconstructions are presented in the same manner as in Figure 2.7. The reconstructed images are displayed with the same windowing setting for comparison. To the right of each reconstructed image, its absolute difference from the non-accelerated image is displayed, with a windowing setting that is much lower than that for the reconstructed image. On each difference image, the average absolute difference of a region with pronounced aliasing visible in the fixed kernel reconstruction (indicated by a rectangle) is given in an oval annotation. Fixed kernel GRAPPA reconstruction (left column) suffers from noticeable aliasing artifacts. Note that the CV identified kernel supports for ORF = 2 and ORF = 3, $[-1 \ 1] \times [-1 \ 0 \ 1]$ (along $k_y \times$ along k_x , relative to the k -space point to be interpolated) and $[-1 \ 1] \times [-2 \ -1 \ 0 \ 1 \ 2]$, respectively, are smaller than 4×5 . The numbers in the brackets representing the kernel supports indicate, for each direction, the position of acquired point used in the interpolation relative to the missing datum under consideration.

Figure 2.7 presents a series of human brain images: (A) the non-accelerated image and (B) GRAPPA reconstructed images using a fixed 4×5 kernel support and CV identified kernel support. GRAPPA reconstruction was applied for different acquisition schemes: (a) ORF = 2 with 2 ACS lines, (b) ORF = 3 with 6 ACS lines, and (c) ORF = 4 with 9 ACS lines. The reconstructions are presented in the same manner as in Figure 2.6.

The overall mean-squared difference between the non-accelerated and reconstructed images is shown in Table 1 and discussed later. The kernel supports identified were $[-1 \ 1] \times [-1 \ 0 \ 1]$ (along $k_y \times$ along k_x), $[-1 \ 2] \times [-2 \ -1 \ 0 \ 1 \ 2]$, and $[-1 \ 3] \times [-2 \ -1 \ 0 \ 1 \ 2]$ for ORF = 2, ORF = 3, and ORF = 4, respectively.

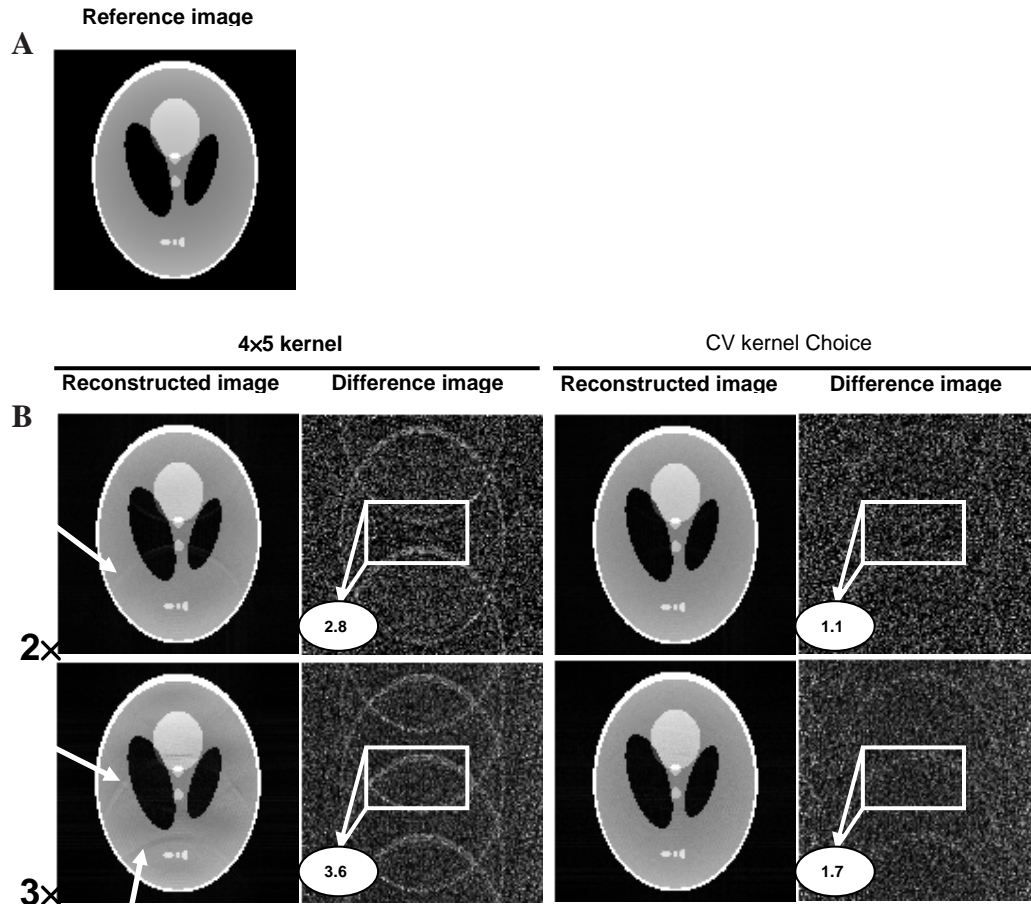


Figure 2.6 Reconstructed Shepp-Logan phantom images

(A) non-accelerated image used as reference, and (B) GRAPPA reconstructed images using a 4×5 kernel (left) and using kernel supports determined by CV (right). In (B), the two rows correspond to 2 parallel imaging settings (from the top to bottom): $R = 2$ with 3 reference lines and $R = 3$ with 9 reference lines. To the right of each reconstructed image, its absolute difference with the non-accelerated image is shown. The average absolute difference in the ROI indicated by the rectangular box is shown in an oval inset in each difference image.

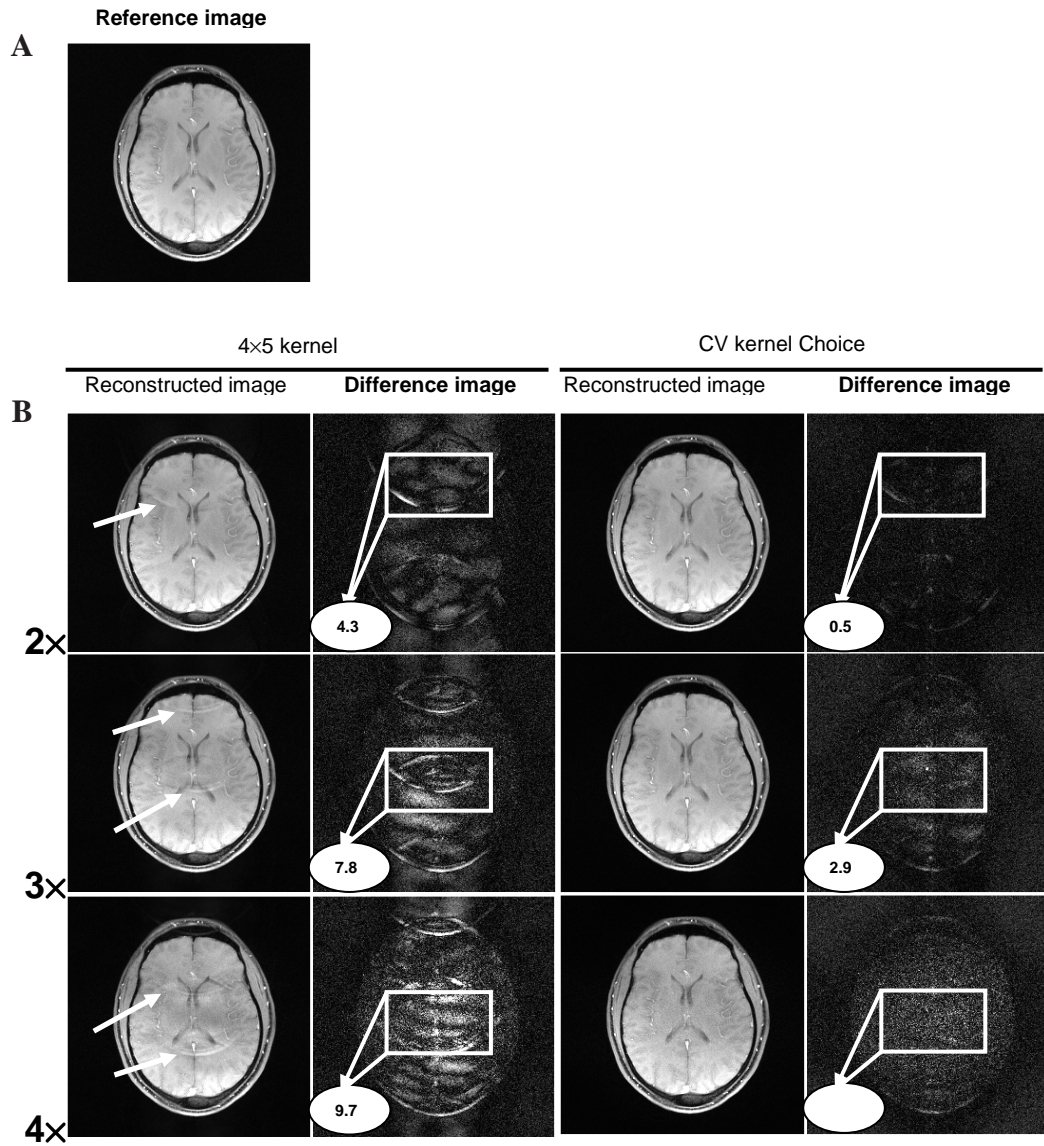


Figure 2.7 Reconstructed brain data images

(A) non-accelerated image used as reference, and (B) GRAPPA reconstructed images using a 4×5 kernel (left) and using kernel supports determined by CV (right). In (B), the three rows correspond to 3 parallel imaging settings (from the top to bottom): ORF = 2 with 2 ACS lines, ORF = 3 with 6 ACS lines, and ORF = 4 with 9 ACS lines. To the right of each reconstructed image, its absolute difference with the non-accelerated image is shown. On each difference image, the average pixel intensity of a region with pronounced aliasing visible in the fixed kernel reconstruction (indicated by a rectangle) is given in an oval annotation to illustrate the difference in ghosting between the two reconstructions.

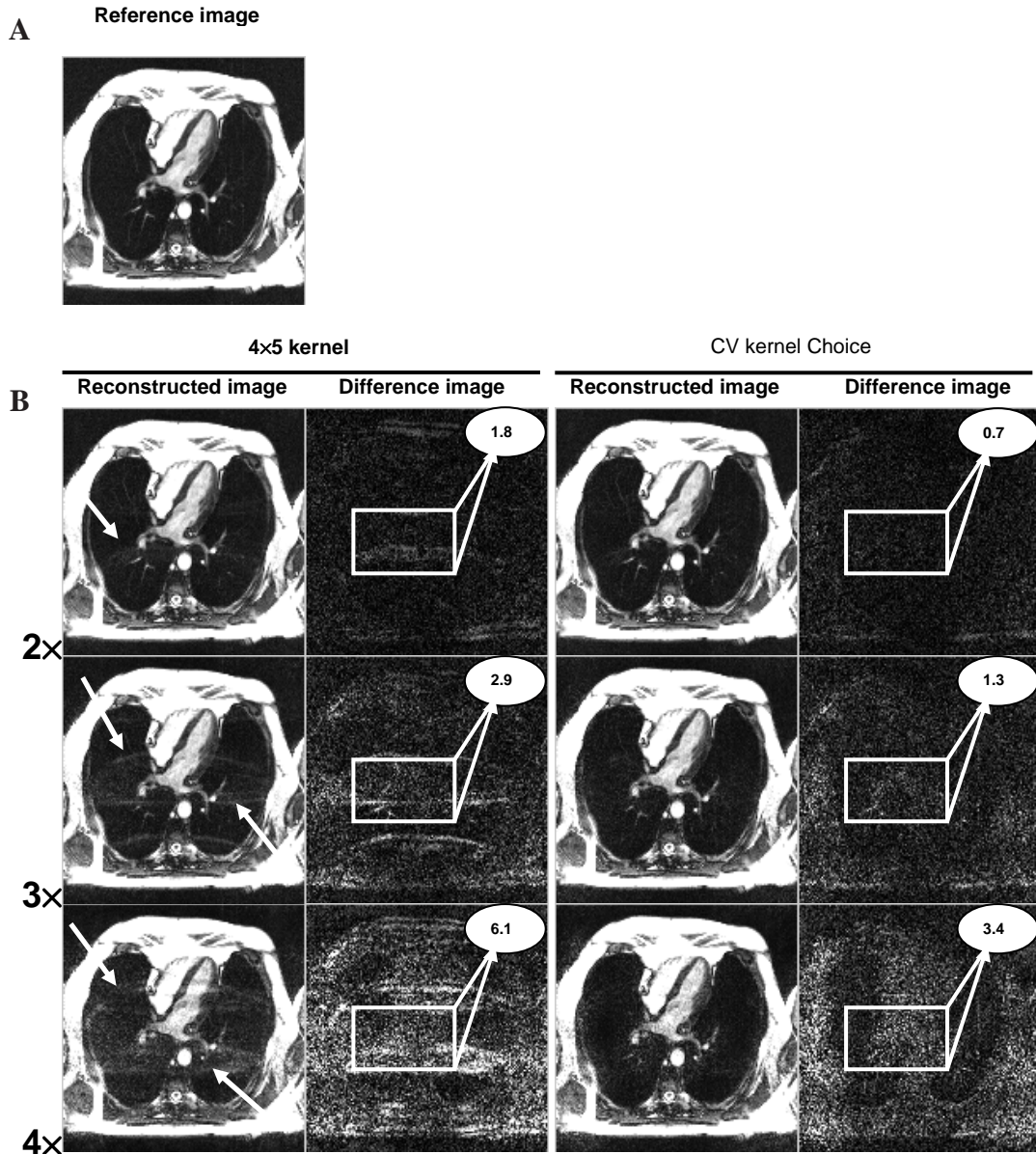


Figure 2.8 Reconstructed cardiac images

(A) non-accelerated image used as reference, and (B) GRAPPA images reconstructed with a 4×5 kernel support (left) and CV-identified kernel supports (right). From the top to bottom, the three rows in (B) correspond to 3 parallel image settings: ORF = 2 with 4 ACS lines, ORF = 3 with 8 ACS lines, and ORF = 4 with 12 ACS lines. To the right of each reconstructed image, its absolute difference with the non-accelerated image is shown. On each difference image, the average pixel intensity of a region with pronounced aliasing visible in the fixed kernel reconstruction (indicated by a rectangle) is given in an oval annotation to illustrate the difference in ghosting between the two reconstructions.

GRAPPA reconstruction errors, as defined in the section “Methods”, were also computed for situations with more ACS lines and compared across the two reconstruction strategies for different acquisition schemes. These results are summarized in Table 1. Note that this is not the ε_{CV} used to obtain the optimal kernel from the ACS data.

Figure 2.8 presents a series of four-chamber view cardiac images of a single frame TrueFISP cine sequence reconstructed from the two strategies. The images are organized in the same manner as in Figure 2.6.

2.4 Discussion

2.4.1 CV error and optimal kernel support

In both Figure 2.5A and Figure 2.5B, all three cross-validation error plots share the same trend: as the model complexity increases, the CV error decreases, reaches a minimum and then increases. In other words, if the model is too simple, it does not capture the complexity of the data sufficiently. If the model is too complex, it becomes too sensitive to the errors in the data and over-fits the calibration data. The kernel support with minimum CV error corresponds to a suitable compromise for model complexity. This feature reflects the combined effect of model error and noise-related error in GRAPPA reconstruction. It should also be noted that the CV error decreases with increasing number of ACS lines, owing to increased knowledge regarding the coil sensitivity implicitly provided by the ACS lines. The behavior of the CV error seen here is in good agreement with that of the total error power discussed by Yeh *et al.* (9), who

measured the combined effect of kernel size truncation (through the k -space locality approximation) and noise amplification. In fact, since the testing data is the set of ACS lines, it can be stated that the CV error is the k -space version of the error power (9) calculated at the resolution represented by the ACS lines. In most cases, this would correspond to an error at low resolution. In cases where a full reference calibration scan is available, the CV error would not be limited to low-resolution. In general, CV operates on a dataset for which the calibration lines are already predefined. In cases where the ACS lines located at the low frequency do not capture the relationship needed for interpolation in the high frequency region (which may occur when the true sensitivity maps are not smooth enough ((10)), neither CV nor any other method that solely exploits these ACS lines would guarantee an artifact free reconstruction.

In generating the plots shown in Figure 2.5, only kernel supports formed from acquired signals nearest to the fitted datum were considered. However, the observations regarding trading off model complexity with noise should be valid in general although it is expected that with each kernel size, the CV error may vary also with the kernel shape. For a fix 4×5 kernel size, we examined the CV error for different kernel shapes. With this exhaustive search (data not shown here), the best kernel support corresponded to the one that met the locality criterion. While this result cannot be generalized, it indicates that the k -space locality criterion is a good approximation.

Table 2-1 Reconstruction mean square error

Brain image errors of GRAPPA reconstructions obtained: using a 4×5 support and the CV derived supports, respectively.

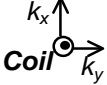
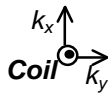


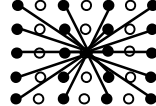
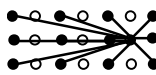
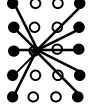
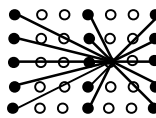
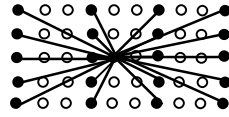
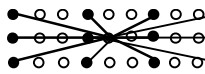
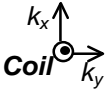
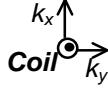
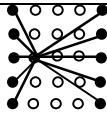
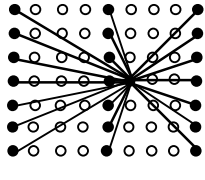
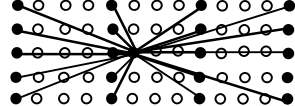
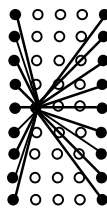
ORF	# of ACS lines	Recon error (ϵ) (4×5)	Recon error (ϵ) (CV kernel)	CV identified kernel support 	4×5 kernel support 
2x	2	1459	560	 [-1 1] \times [-1 0 1]	
	6	468	431	 [-3 -1 1] \times [-1 0 1]	 [-3 -1 1 3] \times [-2 -1 0 1 2]
	12	426	412	 [-5 -3 -1 1] \times [-1 0 1]	
3x	6	1066	569	 [-1 3] \times [-2 -1 0 1 2]	
	12	497	470	 [-4 -1 2] \times [-2 -1 0 1 2]	 [-4 -1 2 5] \times [-2 -1 0 1 2]
	16	477	459	 [-4 -1 2 5] \times [-1 0 1]	

Table 2-1 Continued

ORF	# of ACS lines	Recon error (ϵ) (4x5)	Recon error (ϵ) (CV kernel)	CV identified kernel support 	4 x 5 kernel support 
	9	1345	616	 [-1 3] x [-2 -1 0 1 2]	
4x	15	677	573	 [-5 -1 3] x [-3 -2 -1 0 1 2 3]	 [-5 -1 3 7] x [-2 -1 0 1 2]
	18	617	559	 [-1 3] x [-4 -3 -2 -1 0 1 2 3 4]	

Reconstructions for 2x outer reduction with 2 ACS lines, 3x outer reduction with 6 ACS lines, and 4x outer reduction with 9 ACS lines are shown in Figure 2.7.

2.4.2 Qualitative image comparisons

The results of Figure 2.6 suggest with the simulated data used, the 4 x 5 kernel likely corresponds to a model that is too complex and therefore is unable to accurately predict the missing data. In contrast, the CV identified the proper kernel supports to use in the reconstruction and led to virtually artifact free images (right column of Figure 2.6)

Figure 2.7 illustrates the *in vivo* data reconstruction results for the two reconstruction strategies described above, with different acquisition schemes: 2, 6, and 9 ACS lines for outer reduction factors of 2, 3, and 4, respectively. GRAPPA with the fixed kernel support (left column) led to images with significant aliasing artifacts (as indicated on both reconstructed images (arrows) and difference images), whereas the CV guided GRAPPA reconstruction produced images exhibiting minimal aliasing (right column). Residual aliasing artifacts in the CV images, which are inevitable given the limited number of ACS lines, can only be observed in the difference images and are significantly lower (reduced by 2-3 folds in the aliases) than those in the fixed kernel reconstruction.

Similar observations can be made in Figure 2.8 which shows GRAPPA reconstructions, with a 4×5 fixed kernel support and CV identified kernel supports, of four-chamber view TrueFISP cardiac images. While the difference images for the fixed kernel show pronounced residual aliasing, the difference images for reconstructions with the CV kernels only exhibit background noise with no noticeable residual aliasing. This result again demonstrates the effectiveness of the CV method in identifying a proper kernel support for GRAPPA reconstruction for a given coil configuration, imaging orientation, and noise level in the data

2.4.3 Implication on temporal resolution in cardiac imaging

As the number of ACS lines increases, the difference between the images reconstructed by the fixed kernel support and CV identified kernel supports becomes less

visually apparent and needs to be assessed quantitatively. As illustrated in Table 1 for the case of brain data, the reconstruction error computed at different parallel imaging settings indicate that the CV identified kernel supports consistently outperforms the fixed 4×5 kernel support. Interestingly, at the acceleration factor of 3, the CV method with 18 reference lines produced better reconstruction than GRAPPA with a 4×5 kernel with 24 reference lines. Similar behavior is also seen at the acceleration factor of 4. This observation suggests that in some cases the CV method produces comparable results as GRAPPA with a fixed window but with fewer number of ACS. It is also worth noting the large variation in the kernel supports identified by the CV. These kernel supports are not obvious and may not be intuitively identified. Similar results were obtained (not shown) for the cardiac data suggesting that GRAPPA can be calibrated with fewer number of ACS lines in cardiac imaging while preserving a high quality image even at high outer reduction factor. The ability to reduce the ACS lines needed is expected to be beneficial for cardiac imaging where temporal resolution is important.

2.4.4 Computational considerations

With a maximum search size set to 10×10 , slightly larger than what is used in a previous paper (13), the CV algorithm adds an additional computational time of 13 ~ 29 seconds to conventional GRAPPA reconstruction time. Using k-fold cross-validation (rather than the leave-one-out approach used here) can reduce this time. Also, the computational time for CV kernel support selection can be further shorted by distributed computing. In practice, if computation time is of concern, the user can choose a set of kernel supports to be examined by CV based on computational considerations. For

example, restricting the search to kernel size using the k -space locality criterion (17), for a fixed configuration, seemed to have produced better results compared to the use of 4×5 kernel size of same configuration in all cases examined in this work. In general the cross-validation presented can be applied in conjunction with any GRAPPA reconstruction for improved performance.

2.5 Conclusions

In this work, cross-validation is introduced for optimal kernel support selection in GRAPPA reconstruction for a given accelerated data set. Cross-validation error was first demonstrated to vary with GRAPPA reconstruction kernel support. Subsequently, GRAPPA reconstructions of experimental data were performed with cross-validation selected kernels and a fixed 4×5 kernel. Comparison of results demonstrated that CV selection led to GRAPPA results with significantly reduced aliasing artifacts. The method is simple and applied in post-processing and can be used with GRAPPA routinely.

2.6 Chapter 2 References

1. Sodickson DK, Manning WJ. Simultaneous acquisition of spatial harmonics (SMASH): fast imaging with radiofrequency coil arrays. Magn Reson Med 1997;38(4):591-603.

2. Jakob PM, Griswold MA, Edelman RR, Sodickson DK. AUTO-SMASH: a self-calibrating technique for SMASH imaging. *SiMultaneous Acquisition of Spatial Harmonics. Magma* 1998;7(1):42-54.
3. Lee RF, Westgate CR, Weiss RG, Bottomley PA. An analytical SMASH procedure (ASP) for sensitivity-encoded MRI. *Magn Reson Med* 2000;43(5):716-725.
4. Sodickson DK. Tailored SMASH image reconstructions for robust in vivo parallel MR imaging. *Magn Reson Med* 2000;44(2):243-251.
5. Heidemann RM, Griswold MA, Haase A, Jakob PM. VD-AUTO-SMASH imaging. *Magn Reson Med* 2001;45(6):1066-1074.
6. Bydder M, Larkman DJ, Hajnal JV. Generalized SMASH imaging. *Magn Reson Med* 2002;47(1):160-170.
7. McKenzie CA, Ohliger MA, Yeh EN, Price MD, Sodickson DK. Coil-by-coil image reconstruction with SMASH. *Magn Reson Med* 2001;46(3):619-623.
8. Griswold MA, Jakob PM, Heidemann RM, Nittka M, Jellus V, Wang J, Kiefer B, Haase A. Generalized autocalibrating partially parallel acquisitions (GRAPPA). *Magn Reson Med* 2002;47(6):1202-1210.
9. Yeh EN, McKenzie CA, Ohliger MA, Sodickson DK. Parallel magnetic resonance imaging with adaptive radius in k -space (PARS): constrained image reconstruction using k -space locality in radiofrequency coil encoded data. *Magn Reson Med* 2005;53(6):1383-1392.
10. Huang F, Duensing GR. A theoretical analysis of errors in GRAPPA. In: *Proceedings of the 14th Annual Meeting of ISMRM, Seattle* 2006:2468.

11. Wang Z, Wang J, Detre JA. Improved data reconstruction method for GRAPPA. *Magn Reson Med* 2005;54(3):738-742.
12. Hoge WS, Brooks DH, Madore B, Kyriakos WE. A tour of accelerated parallel MR imaging from a linear systems perspective. *Concepts in Magnetic Resonance Part A* 2005;27A(1):17-37
13. Qu P, Shen GX, Wang C, Wu B, Yuan J. Tailored utilization of acquired k -space points for GRAPPA reconstruction. *J Magn Reson* 2005;174(1):60-67.
14. Stone M. Cross-validatory choice and assessment of statistical predictions. *Journal of the Royal Statistical Society: Series B* 1974;B36:111-147.
15. Akaike H. Statistical predictor identification. *Ann Inst Stat Math* 1970;22:203-217.
16. Cherkassky V, Mulier F. *Learning from data: Concepts, theory, and methods*. New York: John Wiley & Sons; 1998.
17. Nana R, Zhao T, Hu T. Automatic kernel selection for optimal GRAPPA reconstruction. In: *Proc of the Annual Meeting of ISMRM 2007*; Berlin. p 747.

CHAPTER 3. A SIMPLE AND ROBUST METRIC FOR SELECTING OPTIMAL RECONSTRUCTION PARAMETERS IN k -SPACE BASED PARALLEL IMAGING⁵

In this chapter, a data consistency error (DCE) function, that exploits the shift invariance requirement of the kernel, is introduced to provide a goodness measure of k -space based parallel MRI reconstruction algorithms. The DCE is derived from the difference between the acquired signals and their estimates obtained based on the interpolation of the estimated missing data. Simulation with experimental data shows a strong correspondence between the DCE and the mean square error in the reconstructed image, demonstrating its potential as a metric for comparing or choosing reconstructions. The DCE is then applied for automatically selecting the optimal kernel support for the generalized auto-calibrating partially parallel acquisition (GRAPPA) reconstruction and the optimal set of data frames for calibration in temporal GRAPPA reconstruction, leading to improved reconstructions compared to existing methods. The DCE is efficient to evaluate, robust for selecting reconstruction parameters, and suitable for characterizing and optimizing k -space based reconstruction in parallel imaging.

⁵ The work in this chapter has been adapted for publication as “Nana R, Hu X. *A simple and Robust Metric for Selecting Optimal Reconstruction Parameters in k -space Based Parallel Imaging*. Magn Reson Med. (Under Review).

3.1 Introduction

Fundamentally, parallel MRI reconstruction in k -space assumes that only a limited number of acquired k -space data contribute to the interpolation of a missing datum (1). For Cartesian sampling methods, it is further assumed that the reconstruction kernel (or simply kernel) is shift invariant in the k -space. In general, the reconstruction performance strongly depends on the selection of settings (e.g. kernel support size, kernel support configuration, calibration dataset) that influence the kernel. For example, small kernels may be inadequate in capturing the complexity of the k -space interpolation while large kernels tend to be overly sensitive to errors in the data, both of which result in poor reconstruction (2,3). A good choice of kernel support size (or simply kernel size), which has been shown to depend on coil array configuration, noise level in the acquired data, imaging configuration, and calibration data, must provide a suitable compromise between the two extremes. Methods for automatically determining the optimal kernel parameters for a given parallel-acquired dataset have been intensively sought (3-5).

The work of Qu et al. (4) presents an improved generalized auto-calibrating partially parallel acquisition (GRAPPA (6)) in which a rank-revealing QR factorization is used to select the most linearly independent columns of the encoding matrix formed from a large local k -space subset. The linear independence criterion here permits the selection of the kernel support configuration, given a fixed kernel size, which minimizes the noise amplification in GRAPPA weights estimation. However, their optimization criterion targets noise performance rather than reconstruction performance.

Samsonov (5) introduced a formalism in which k -space based parallel MRI reconstruction is framed as a way to approximate the inverse of the encoding matrix with a sparse matrix, with the error of this approximation used as a criterion for optimizing the kernel. In contrast to Qu's approach (4), the optimization criterion targets the model accuracy. Although conditioning of the matrix inversion using truncated singular value decomposition (7) was able to reduce the noise related errors, it also reduced model accuracy. Unfortunately, the method described by Samsonov (5) did not provide a means to simultaneously minimize both the model error and noise related error.

In a recently published approach, the selection of the kernel support for GRAPPA was posed as a model selection problem and cross-validation was used to select the optimal kernel support among a group of kernel support candidates (3). Unlike the previous methods, the cross-validation approach targets the total error, minimizing both the model error and noise related errors in GRAPPA. However, it can be computationally expensive, as K -fold cross-validation requires each kernel support candidate to be trained K times ($K > 1$). Additionally, the performance of cross-validation may vary with the choice of K . For example, the bias of the true error rate estimator (the estimator accuracy) decreases whereas the variance of the true error rate estimator increases with increasing values of K . Selection of the optimal K for a given situation is still an open question (8). Furthermore, because the validation is performed only on reference k -space lines near the origin, the cross-validation approach focuses on errors in the low k -space. Therefore, a

computationally efficient, robust and balanced metric that facilitates the selection of reconstruction kernel settings which balances between artifacts and SNR is still desirable.

In this work, we present a data consistency error (DCE) function that exploits the shift invariance requirement of the kernel to provide a simple measure of reconstruction error of k -space interpolation for Cartesian parallel imaging. This DCE is derived from the difference between the acquired signals and their estimates obtained from the interpolations of the estimated missing data. It is shown experimentally that this DCE can be used as an optimization criterion, which targets the total error, for selecting the kernel settings that balance between artifacts and SNR. Specifically, the DCE was used to automatically select the kernel support for GRAPPA and the set of calibrating frames for temporal GRAPPA (TGRAPPA (9)) that result to an optimal reconstruction. The performance of DCE-optimized reconstruction is compared to existing methods using experimental data with different amounts of the reference k -space data.

3.2 Theory

The development presented here is based on GRAPPA interpolation procedure and can be readily extended to other k -space based parallel MRI reconstruction algorithms. It is assumed that the data are undersampled along the phase encoding direction by a factor of R . In GRAPPA, a missing k -space point in a single coil is reconstructed by linearly combining data acquired in both phase (k_y) and frequency (k_x) encoding directions from

all coils. In a blockwise notation (Figure 3.1a), the GRAPPA reconstruction can be written as (10)

$$S_j(k_y + r\Delta k_y, k_x) = \sum_{l=1}^L \sum_{b=-N_b}^{N_a} \sum_{h=-H_l}^{H_r} W_{j,r}(l, b, h) \times S_l(k_y + bR\Delta k_y, k_x + h\Delta k_x) \quad [3.1]$$

where S_j represents the k -space signal for the j th coil at the k -space coordinates (k_x, k_y) , and Δk_y and Δk_x are the sampling intervals along k_y and k_x , respectively, r ($r \leq R$) is the number of Δk_y offset of the missing datum in a block, N_a and N_b are the number of blocks before and after the current block to which the missing data belongs, H_l and H_r are the number of left and right neighboring columns, respectively, used in the reconstruction, L is the number of coils in the array, and $W_{j,r}$ refers to the weights of the r -th line of coil j . A block consists of one acquired line of data and the neighboring $R-1$ missing lines. The reconstruction weights are obtained by solving equation [1] in which the left side is filled by auto-calibrating data.

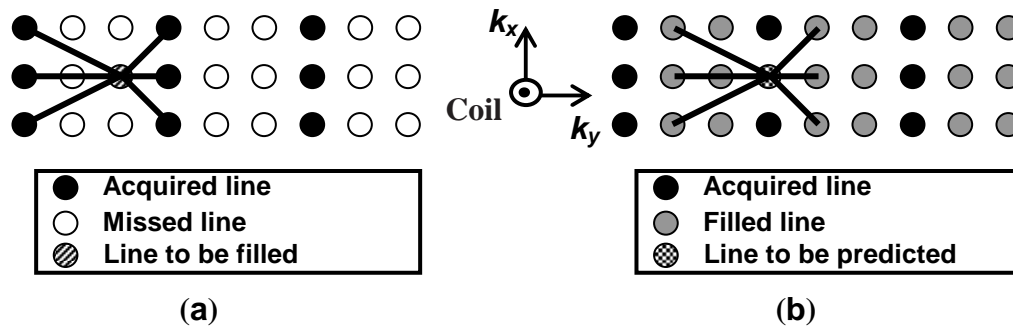


Figure 3.1 Shift invariance property of the GRAPPA kernel

(a) A missed line is interpolated from acquired lines from all coils; (b) an acquired line should be predictable from the estimated missing lines. In this illustration, $R = 3$ and a kernel of 2×3 is used.

Since GRAPPA kernel should ideally be shift invariant in the k -space, the estimated missing lines should be capable of predicting the acquired lines as depicted in Figure 3.1b, allowing one to write

$$S_j(k_y, k_x) = \sum_{l=1}^L \sum_{b=-N_b}^{N_a} \sum_{h=-H_l}^{H_r} W_{j,r}(l, b, h) \times S_l(k_y + bR\Delta k_y + \Delta k_y, k_x + h\Delta k_x) \quad [3.2]$$

It is reasonable to hypothesize that the optimal set of weights minimizes the difference between the original acquired signals and their estimates. Therefore, a reconstruction parameter setting m (e.g. kernel size, kernel support configuration, calibration dataset) of the kernel results in an optimal reconstruction if it minimizes the data consistency error function given by

$$DCE(m) = \frac{\|A - \tilde{A}(m)\|^2}{K_A} \quad [3.3]$$

where $\|\cdot\|$ is the Euclidean norm, A is a vector containing the original data, \tilde{A} is the vector consisting of estimated data obtained using the parameter m , and K_A is the size of A . DCE takes into account both fitting and prediction errors and therefore considers the total error (model error plus noise related errors) during kernel settings optimization.

The practical implementation steps for determining DCE of a given setting is as follows:

- Step 1.* Derive the GRAPPA weights using the calibration information,
- Step 2.* Fill in the missing data of all coils according to Eq. [1],
- Step 3.* Predict the acquired data using the same GRAPPA weights using (Eq. [2]),
- Step 4.* Compute DCE using Eq. [3].

3.3 Methods

The effectiveness of the proposed data consistency error was experimentally evaluated on GRAPPA and TGRAPPA reconstructions. The DCE was applied to automatically select the kernel setting that resulted in an optimal reconstruction. In both applications, the selection process started by forming the collection of kernel settings to be examined by DCE followed by the evaluation of DCE of each setting and the identification of the setting with the minimum DCE. At the same time, GRAPPA or TGRAPPA reconstruction was also carried out for each kernel setting examined by DCE in order to compute the reconstruction mean square error (MSE) for comparison. Here MSE is defined by $MSE = \sum_n^N |I(n) - I_{ref}(n)|^2 / N$ where I represents the GRAPPA or TGRAPPA reconstructed image, I_{ref} is the full-data reconstructed image, N is the total number of pixels, and n is the pixel index.

GRAPPA reconstruction using DCE-identified kernel setting was compared to those using a $4 \times 5 \times 12$ kernel, the sparse-optimized kernel (5), and the cross-validation-identified kernel (3). The first, second, and third numbers of the kernel notation represent the kernel dimensions along k_y , k_x , and coil, respectively. The coil dimension is assumed constant for cross-validation and DCE selected kernels and will be omitted in the kernel representation hereafter for simplicity. As the sparse approximation method given by Samsonov (5) did not specify a means for selecting the stopping criterion in the optimization process, the target k -space subset size was chosen to match the number of

points contained in the DCE-identified kernel in order to make a fair comparison between the two methods. In each case, we verified that the sparse approximation error as a function of k -space subset size decreased down to the desired size (as described in Samsonov's paper (5)). Additionally the impact of applying Tikhonov regularization (11) on the 4×5 kernel was investigated and compared to the DCE-optimized reconstruction. L-curve method (11) was used for optimal regularization parameter selection. The optimal regularization parameter (the corner of the L-curve) was selected as the one where the product of abscissa and ordinate is a minimum (12). Experimental data were collected with participants' written informed consent in accordance with institutional review board policies. All algorithms were implemented in MATLAB (The Mathworks Inc., Natick MA, USA) on a Quad Core Intel Xeon CPU 2.4 GHz computer with 8GB RAM.

3.3.1 Application to GRAPPA

The aspect of the kernel to select here was the kernel support. The set of kernel supports to be examined by DCE was formed by following the procedure described previously (3) which considers only rectangular kernels designed according to the k -space locality criterion (2). The kernel support that minimized DCE was taken as the optimal one.

Axial brain imaging was performed on a 3T Siemens TimTM Trio whole-body MR scanner (Siemens Medical Solutions, Erlangen, Germany) equipped with a 12-channel head matrix coil. Fully sampled scans were acquired from healthy adult human

volunteers using a gradient-echo sequence (TR = 300 ms, TE = 4 ms, flip angle = 80°, slice thickness = 5 mm, FOV = 256 mm, matrix = 256 × 256 × 12) and later downsampled to emulate the parallel imaging acquisition procedure. Parallel imaging datasets were generated with outer reduction factors (ORF) of 2, 3, and 4, respectively, and different numbers of ACS lines.

3.3.2 Application to TGRAPPA

In TGRAPPA (9), adjacent undersampled time frames are used as the calibration data in the GRAPPA reconstruction process of a given time frame. Since different time frames may carry different sensitivity information in real time cardiac imaging, the number of calibrating frames should be, in principle as minimal as possible (i.e. equals the acceleration factor) to minimize the effect of sensitivity mismatch and temporal blurring. In the original TGRAPPA implementation, more than the minimum number is used to improve the SNR with averaging of calibration data. In the present work, DCE was applied to select the number of calibrating frames and the kernel support in order to achieve an optimal TGRAPPA reconstruction. Since the procedure for the selection of kernel support is the same as described in the previous subsection, only the calibrating frames selection is described here.

It was assumed (as per original implementation of TGRAPPA) that the optimal set is comprised of consecutive frames nearest the frame to be reconstructed. For the reconstruction of each frame, DCE was calculated for calibration data sets formed by its neighboring frames, starting from the one with the minimum number of frames needed

for calibration (i.e., the parallel imaging acceleration factor including the frame under consideration) to a preset maximum. The minimum calibration data sets for $R = 2, 3,$ and $4,$ respectively are shown in Figure 3.2a and their possible increments are illustrated in Figure 3.2b. This process was repeated for all kernel supports to be examined. The combination of kernel support and number of calibrating frames that minimized DCE was taken as the optimal kernel parameter set.

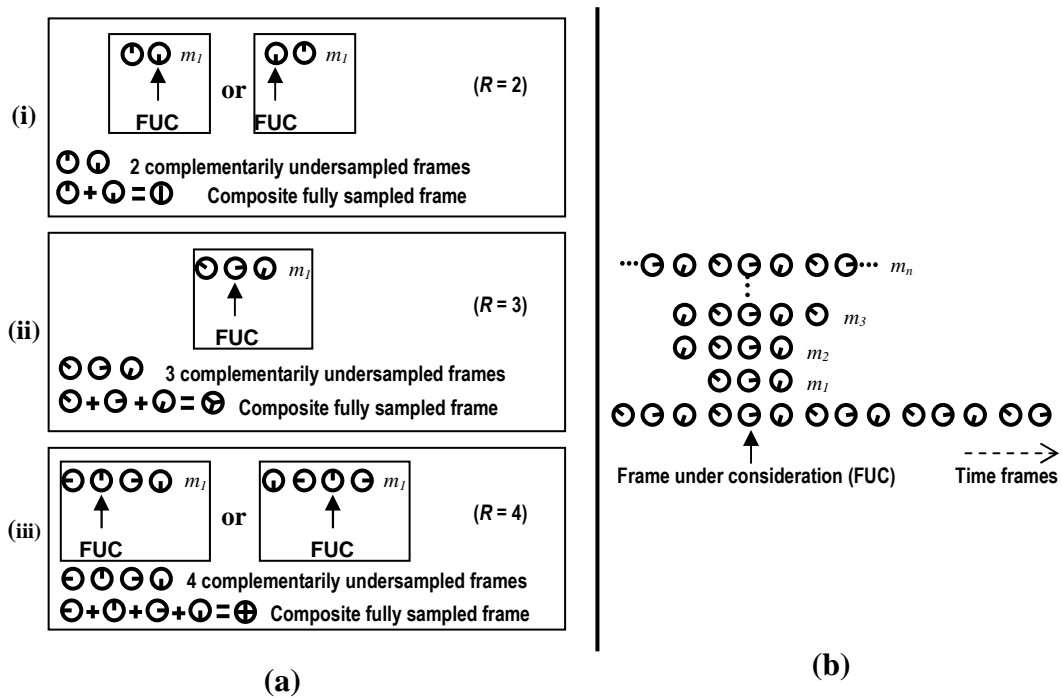


Figure 3.2 Formation of the set of frames to be examined by DCE

The initial set (m_1) is formed with the minimum number of adjacent undersampled frames necessary to form a complete dataset for calibration, which equals R (including the frame under consideration). (a) Possible configurations of m_1 assuming that only frames nearest to the frame to be reconstructed contribute to the calibration process. (b) Formation of other sets m_i by addition of one frame at the time up to the maximum number allowed by the dataset or user-defined number.

Real-time non-gated, non-breath-hold cardiac imaging was performed on a 1.5T Siemens Avanto with a 15-channel cardiac matrix coil using a trueFISP sequence. Fully sampled short-axis view cardiac data were acquired at a rate of 7 fps on healthy subjects (TR = 2.29 ms, TE = 1.15 ms, flip angle = 70° , slice thickness = 8 mm, FOV = 360×264.38 mm, matrix = $256 \times 56 \times 15$) and later downsampled in a time-interleaved phase-encoding scheme as described by Breuer *et al.* (9). Three parallel MRI datasets were synthesized with acceleration factors (R) 2, 3, and 4, respectively. In all TGRAPPA reconstructions performed here, the full extent of the k -space calibration data was used to derive the GRAPPA weights.

3.4 Results

The dependence of DCE on the GRAPPA kernel size along the phase encoding direction and the number of ACS lines for three axial brain datasets downsampled with ORF = 2 (top-left), ORF = 3 (top-center), and ORF = 4 (top-right), respectively, is presented in Figure 3.3a. For all plots in Figure 3.3, the kernel size along the readout direction was set to five. The asymmetric “U-shape” and location of the minimum along the kernel size axis of each DCE plot virtually match those of the corresponding MSE plot (Figure 3.3b) obtained under the same conditions. The observed trends were consistent for other kernel sizes along the readout direction.

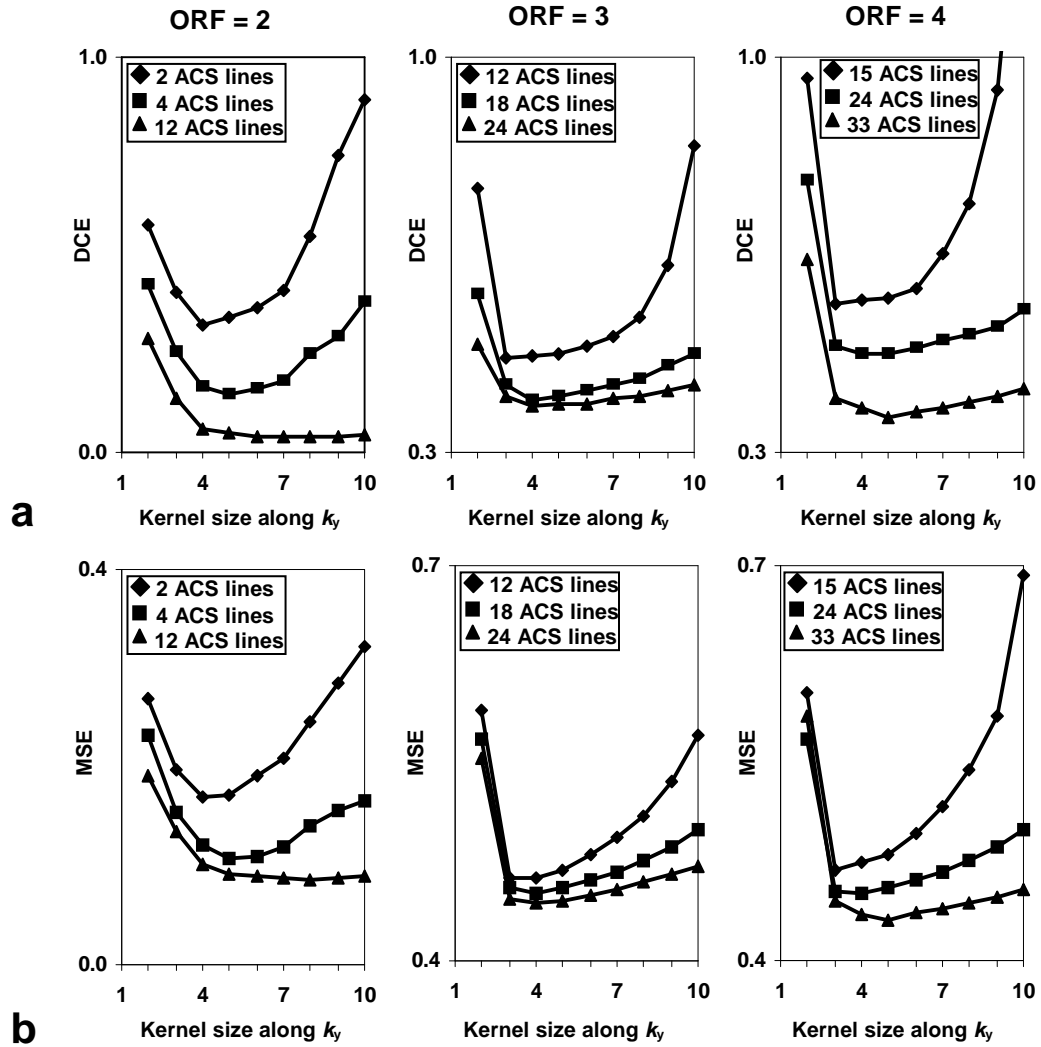


Figure 3.3 Dependence of DCE and MSE on the kernel size

Plots of (a) DCE and (b) MSE of human brain data vs. kernel size along k_y (when the kernel size along k_x is fixed to 5) for different ORFs as indicated at the top of each figure. The legends specify the number of ACS lines used in each case.

Figure 3.4 presents GRAPPA reconstructed images using (a) a 4×5 kernel, (b) the 4×5 kernel with regularization, (c) the sparse optimized subset, and (d) the DCE-identified kernel for 9 and 24 of ACS lines at ORF = 4 (Note that 24 ACS lines are a little more than that used in Refs. (4,10)). The cross-validation identified kernels for these

datasets were the same as those selected by DCE and therefore produced the same images. The DCE-identified kernel supports were 2×7 (along $k_y \times$ along k_x) and 3×11 for 9 ACS lines and 24 ACS lines, respectively. A graphical representation of these kernels is given in Figure 3.4. The sparse-selected kernel support configurations varied in all three dimensions (along k_y , k_x , and coil) and could not be represented graphically in a readily visualized form. The reconstruction with DCE-identified kernel exhibits reduced artifacts and noise level compared to other methods as indicated by the difference images. When considerably large numbers of ACS lines were used, the images generated by the different methods are comparable but, as described below, exhibit slightly different amounts of error. Table 3.11 lists the error of these reconstructions for situations with different ACS lines. In all cases, the DCE-selected kernel resulted in a smaller reconstruction error than other methods. The DCE-selected kernel size (CV-selected kernel as well) increases with increasing number of ACS lines. The DCE-kernel size reaches a ceiling, due to the maximum number of ACS lines that can be used for a given k -space data matrix size. For example, at $R = 4$, the optimal kernel identified by DCE for 147 ACS lines (16×26) is the same as that for 196 ACS lines (full ACS lines) since the maximum number of ACS lines that can be used for a 16×26 kernel size at $R = 4$ with a 256×256 data matrix is 147.

At $R = 4$, the DCE-selected kernel support (16×26) for maximum ACS lines was used to reconstruct images with various sets of fewer ACS lines and the results are presented in Fig 3.5. It is evident that the DCE-identified kernel support for a large

number of ACS lines leads to significant reconstruction noise when applied to data with fewer ACS lines.

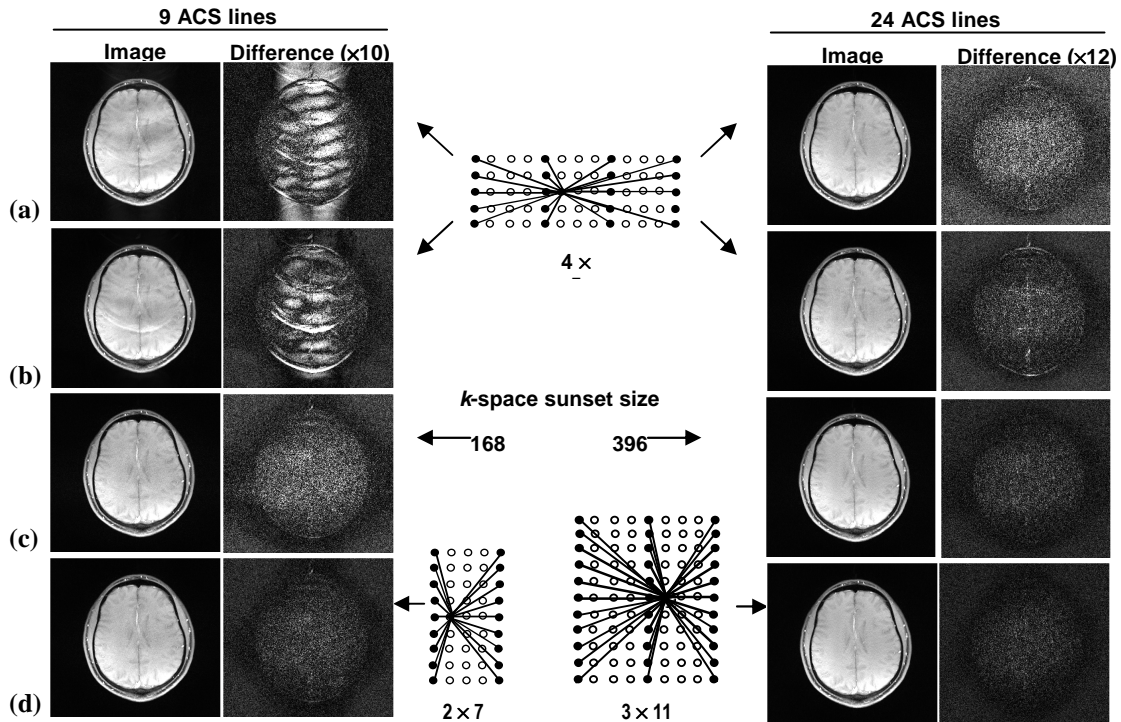


Figure 3.4 Comparison between reconstruction methods on brain data

(a) 4×5 kernel, (b) 4×5 kernel with Tikhonov regularization, (c) sparse-optimized k -space subset, and (d) DCE-identified kernel support. To the right of each reconstructed image, its absolute difference with the non-accelerated image (not shown) is shown. An ORF = 4 and two different number of ACS lines (9 and 45) as indicated on the top of the two main columns were used. The kernel diagrams used by the reconstructions are shown and the arrows are used to associate each kernel to the corresponding reconstruction. The configurations of the k -space subsets used by the sparse method are complex since it varies along the 3 dimensions (k_x , k_y , and coil) and are not represented. The k -space subset size has been chosen to match the size of the DCE-identified kernel.

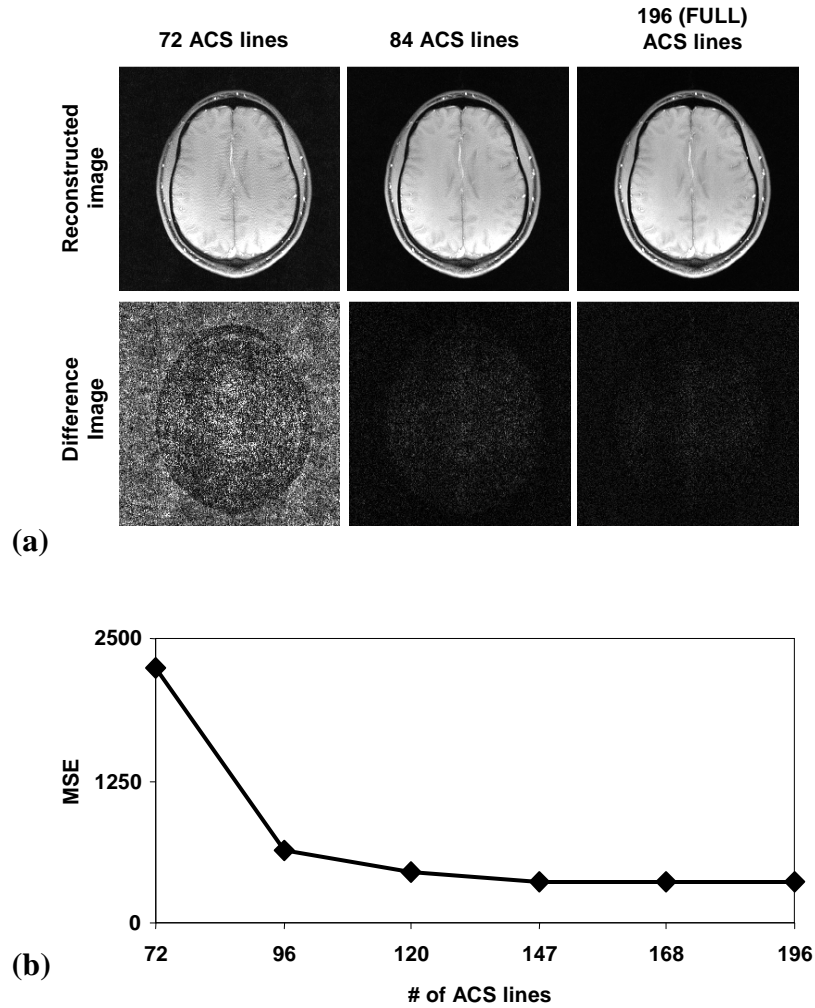


Figure 3.5 Influence of the ACS lines number on the optimal kernel

Reconstruction performance of the DCE-identified kernel when full ACS lines are used versus different lower number of ACS lines: (a) Reconstructed images and corresponding absolute difference with the non-accelerated image, and (b) mean square error.

The dependence of DCE on three TGRAPPA kernel variables (kernel size along k_y , kernel size along k_x , and number of calibrating frames) obtained from the real-time cardiac dataset downsampled at $R = 3$ is shown in Figure 3.6a. In each plot, two variables were set to their optimal values while the other was varied. For frames 2, 43, and 75, the optimal parameters were $\{4, 21, 5\}$, $\{3, 23, 8\}$, and $\{4, 17, 3\}$, respectively. The

parameters in the bracket denote the optimal kernel size along k_y , the optimal kernel size along k_x , and the optimal number of calibrating frames, respectively. There is a virtually identical match in the asymmetric “U-shape” and location of the minimum between each DCE plot and its corresponding MSE plot (Figure 3.6b) obtained under the same conditions.

Because the comparison between the different kernel optimization methods was already made above for GRAPPA, the DCE-optimized TGRAPPA was only compared to the original TGRAPPA which uses 6 (for $R = 2$), 9 (for $R = 3$), or 12 (for $R = 4$) calibrating frames and a 4×5 kernel. Figure 3.7 presents short-axis view cardiac images reconstructed ($R = 3$) using: (b) a 4×5 kernel support and nine adjacent calibrating frames as described in the original TGRAPPA (9), and (c) the DCE-identified numbers of calibrating frames and the DCE-identified kernel supports. The reconstructed images are displayed with the same windowing setting for comparison. Below each reconstructed image, its absolute difference from the full-data derived image (a) is displayed, with a windowing setting that is much lower than that for the reconstructed image. A quantitative comparison of the two TGRAPPA reconstructions in terms of MSE is shown in Figure 3.8 for three different acquisition schemes: (a) $R = 2$, (b) $R = 3$, and (c) $R = 4$, computed for all frames. All plots have the same scale.

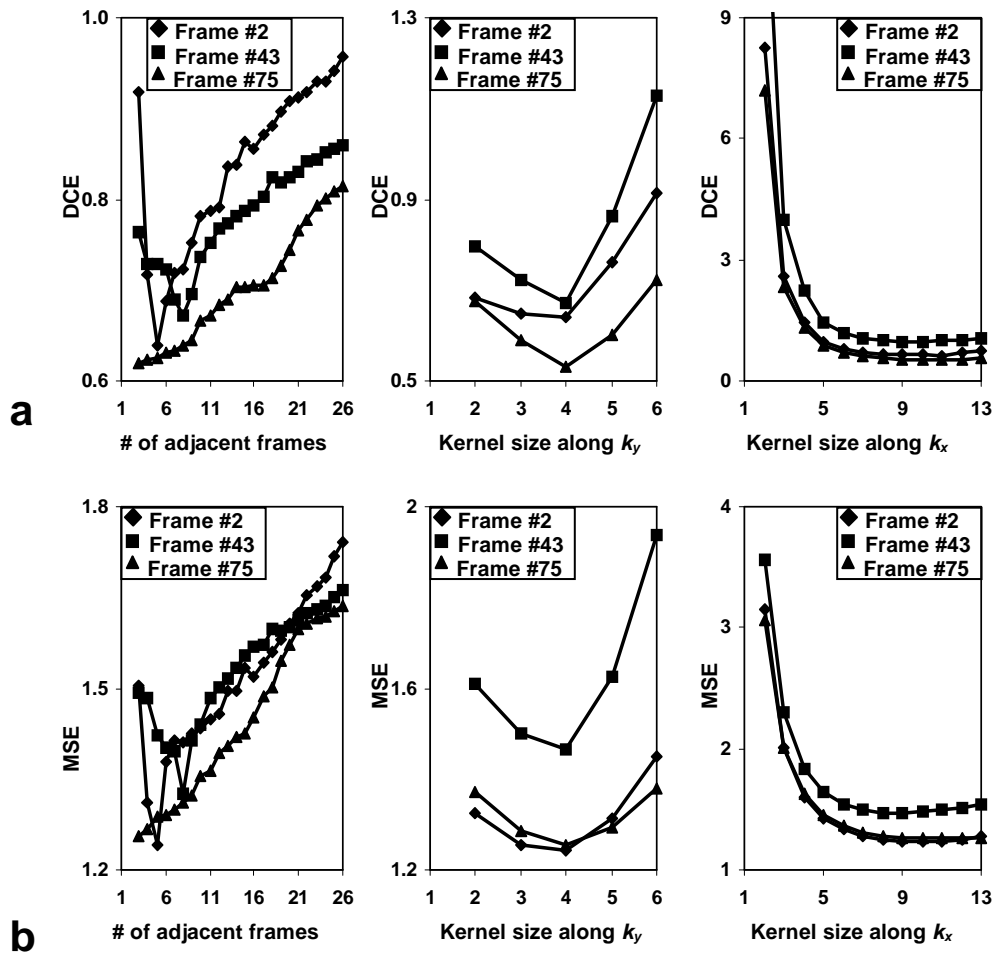


Figure 3.6 Dependence of DCE and MSE on the number of calibrating frames

Plots of (a) DCE and (b) MSE of dynamic cardiac data accelerated at $R = 3$ vs. number of calibrating frames (left), kernel size along k_y (center), and kernel size along k_x (right). In each plot, two variables were set at their optimal values and only one was varied. The legends specify the frame number in each case.

3.5 Discussion

The shift invariance property of the reconstruction kernel in k -space-based Cartesian parallel imaging has been essential for the development of other parallel MRI reconstruction algorithms such as GRAPPA operator formalism (13) and iterative

GRAPPA (14), both of which have found several applications (15-17). In this work, a different exploitation of this shift invariance property is demonstrated with the purpose of optimizing and characterizing current reconstructions in parallel imaging.

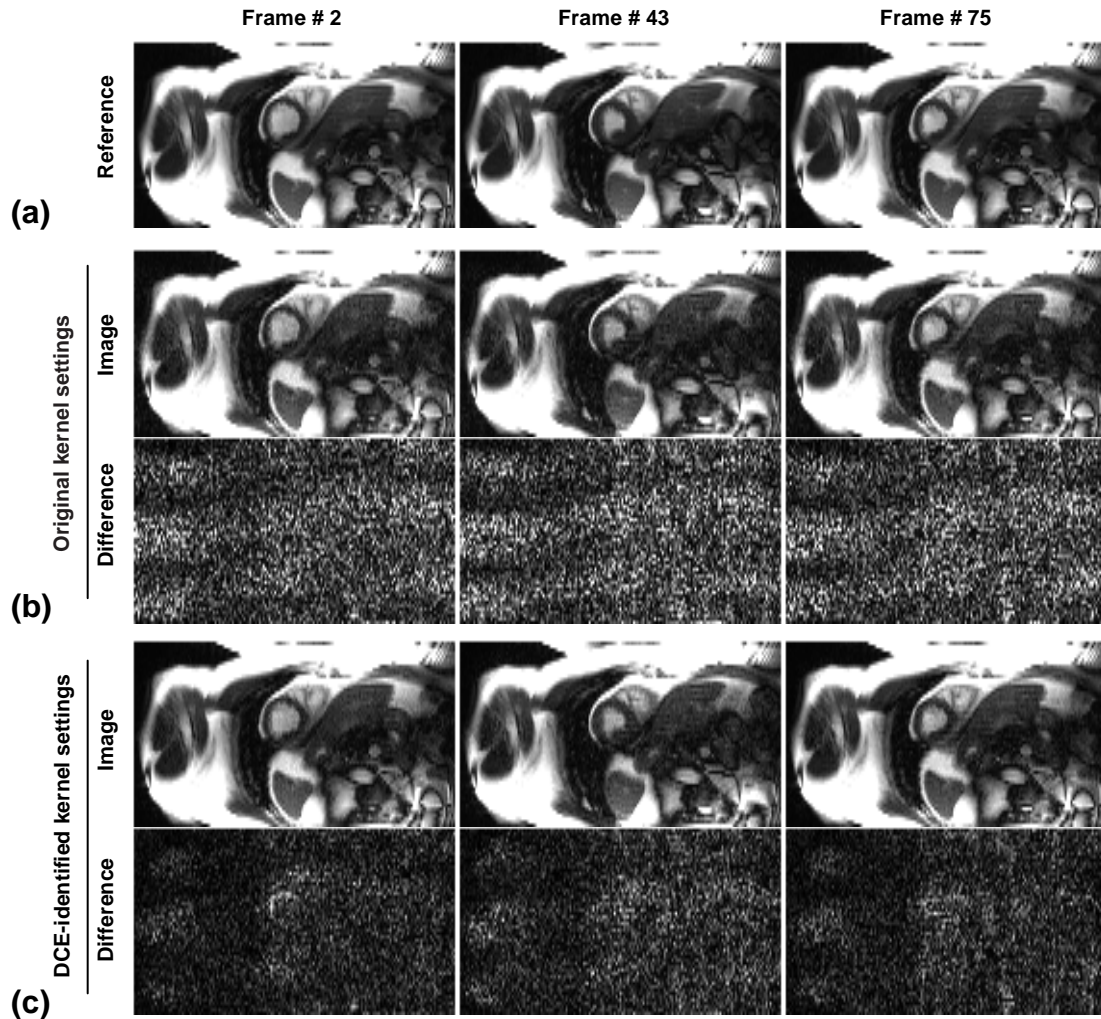


Figure 3.7 Comparison between reconstructions on dynamic cardiac data

(a) Nonaccelerated images used as reference, and TGRAPPA reconstructed images using (b) original parameters, (c) DCE-identified parameters. The absolute difference of each reconstructed image with the non-accelerated image is shown right below the reconstructed image.

The mean square error as defined in this study has been widely used to assess the performance of parallel MRI reconstruction algorithms but requires the full-data reconstructed image (3,5,18,19). The plots in Figs. 3.3 and 3.6 show a strong correspondence between our proposed data consistency error and MSE, suggesting that the DCE is a suitable candidate for characterizing errors in k -space-based parallel MRI reconstruction algorithms. Unlike MSE, DCE does not need the full-data set. This unique feature makes DCE an effective tool for optimizing reconstruction in parallel imaging. The good correspondence between DCE and MSE also indicates that DCE targets the total error in the kernel optimization process.

The shapes of DCE and MSE plots as a function of kernel size of Figure 3.3 and Figure 3.6a demonstrate the conflicting demand between reconstruction model accuracy and stability in GRAPPA reconstruction and are consistent with the results reported previously (2,3). GRAPPA reconstruction using the kernel support that generated the minimum DCE value shows a better tradeoff between artifact and SNR than reconstruction using other methods (Figure 3.4, Table 3.1). The 4×5 kernel was chosen as a representative kernel used for GRAPPA. The sparse approximation method targets the GRAPPA model error rather than the total error and therefore results in a larger reconstruction error as compared to DCE method for all the data examined in this study. The sparse optimized k -space subsets of sizes 168 and 396, respectively, used for the reconstructions in Figure 3.4 were determined in 137 s and 349 s, respectively, using the initial larger k -space subset of $7 \times 18 \times 12$ (similar to that is used by Samsonov (5) with

the exception of the number of coils). As a comparison, the corresponding DCE-identified kernels were identified in 9 s and 11 s, respectively, with a maximum search size of 7×18 . Although these computation times should not be directly compared as the DCE method explicitly utilizes the locality criterion (2) and does not vary the kernel support with coils whereas the sparse method allows the kernel to vary along three dimensions and uses the locality criterion only when defining the search space, they are indicative of the computational efficiency of these methods. Note that the DCE-identified kernel support led to smaller reconstruction errors on all the data examined in this study, suggesting that the locality criterion is a good approximation.

For image space based reconstructions such as the sensitivity encoding (SENSE (20)), which has the appeal of a theoretical exact solution to the parallel imaging problem, the role played by regularization is explicit since it can considerably mitigate the issue of noise amplification during matrix inversion (21). In k -space based parallel imaging reconstructions which are theoretically approximate (22), the conditioning of the reconstruction is largely implicit in the approximation made in the reconstruction. Regularization generally reduces noise at the cost of increased artifacts ((5,19)). This is confirmed by Figure 3.4b which shows a net noise reduction but with pronounced artifacts as compared to the images without regularization (Figure 3.4a). It is evident that the 4×5 kernel is too large for the case where 9 ACS lines are used (Fig .3.4b, first reconstructed image in the row), but the result suggests that regularization cannot overcome this limitation whereas DCE can identify the kernel that mitigate the problem. On the other hand, the comparable quality of the regularized and non-regularized

reconstructions with a 4×5 kernel for situations with abundant ACS lines (Table 3.1) indicates the limited benefits of regularization in k -space based parallel imaging (23).

In some cases with large number of ACS lines, the cross-validation kernel choice deviates from that of DCE (Table 1). This is likely due to the increase of the variance of the true error rate estimator when leave-one-out cross-validation (as used throughout this study) is used in situations with large numbers of samples (8). Unfortunately, the optimal K -fold for a given dataset is yet to be determined.

One difference between the method described here and the cross-validation approach we reported earlier (3) is that the former examines data consistency with all sampled k -space data and the latter only looks at the data consistency for ACS lines which are usually centered in the k -space. In other words, cross-validation generally focuses on low-resolution reconstruction error as dictated by the ACS lines residing near the k -space center, whereas DCE examines the reconstruction error at all acquired resolutions. This difference resulted in a small improvement in the DCE based reconstruction in some cases.

A K -fold cross-validation ($K>1$), as described in (3), requires a computation time of approximately $K-1$ times that of DCE search to produce results that are at most comparable. For example, with a maximum search size set to 10×10 , the kernel size searching algorithm using leave-on-out cross-validation on the anatomical data shown in Figure 3.5 adds an additional time of 13-29 sec to conventional GRAPPA reconstruction

whereas the same search using DCE adds only 6-8 sec. This time difference increases with the number of ACS lines and the maximum kernel size to be examined. The computation time of DCE can be further improved by selectively choosing the set of acquired data needed for the determination of DCE.

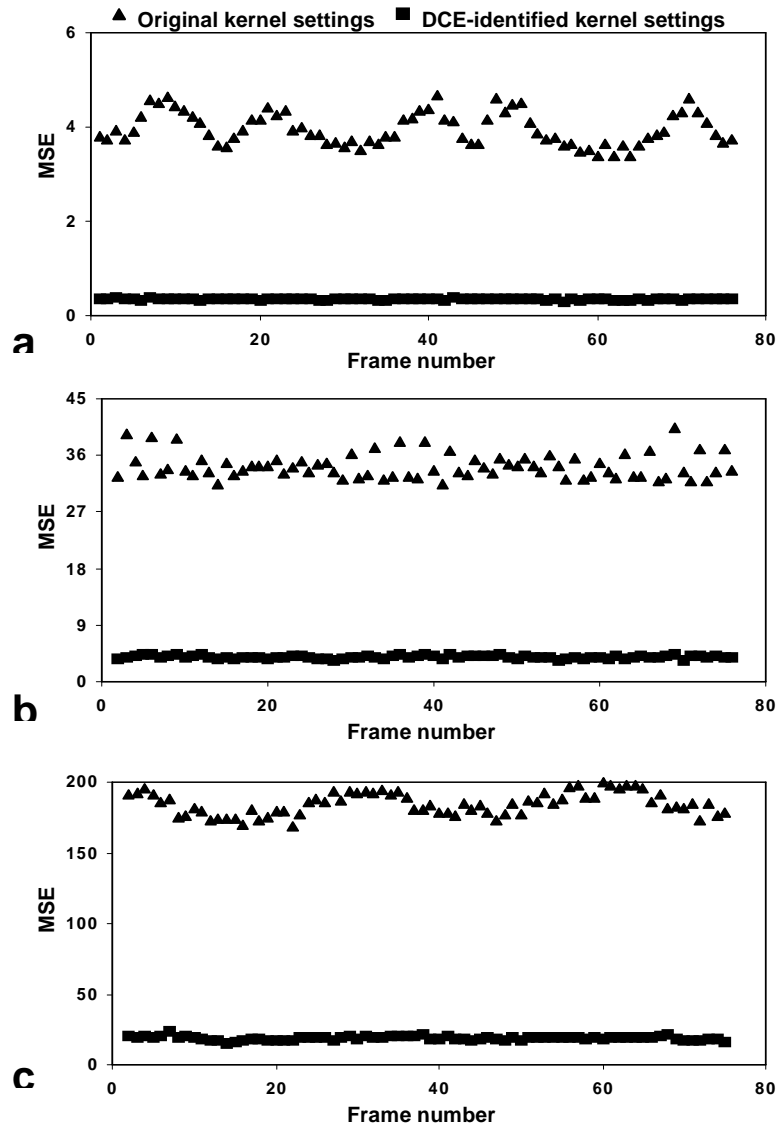


Figure 3.8 Quantitative comparison between TGRAPPA reconstructions

MSE is plotted as a function of frame number in each case and for three parallel MRI settings (a) $R = 2$, (b) $R = 3$, (c) $R = 4$.

The DCE-selected kernel size was shown to increase with increasing number of ACS lines (Table 3.1). On the other hand, significant reconstruction noise occurred when the DCE-selected kernel support for maximum ACS lines was used to reconstruct images with fewer ACS lines. This suggests that the set of kernel supports to be examined by DCE may be adjusted according to the number of ACS lines in order to improve the efficiency of the search.

At the acceleration factor of 3, the DCE method with 18 ACS lines produced better reconstruction than GRAPPA with a 4×5 kernel with 36 ACS lines. Similar behavior is also seen at the acceleration factor of 4. This observation suggests that GRAPPA can be performed with a fewer number of ACS lines while preserving reconstruction quality even at high outer reduction factor. The ability to reduce the ACS lines needed is expected to be beneficial for application requiring internal calibrating lines and where temporal resolution is important.

A limitation of the searching strategy adopted here is the assumptions of locality criterion (2) in forming the set of kernel candidates as described by Nana et al. (3) and the fixed configuration of the kernel along the coil dimension. Although all possible kernel configurations could be examined with DCE in principle, it is impractical due to computational burden. Nonetheless, the DCE-identified kernel shows a better or at least equal performance compared to other methods for all data tested in this study, suggesting that these assumptions are reasonable.

DCE and MSE plots in Figure 3.6 (left column) demonstrate the influence of the number of adjacent calibrating frames on TGRAPPA reconstruction performance. In most cases, the plots exhibit an asymmetric “U-shape” demonstrating a conflicting demand between reconstruction accuracy and stability as a result of including different number frames in the calibration data set. The increase in the number of calibrating frames reduces the effect of noise (as a result of averaging) during the GRAPPA weights estimation but at the same time increases the error due to sensitivity mismatch between different calibrating frames. The number of calibrating frames that generated the minimum DCE corresponds to a suitable compromise between these two errors. The variation of the location of the minimum of DCE plot for different frames indicates that the use of a fixed number of calibrating frames for all frames (as it is the case for original TGRAPPA) is unlikely optimal. The variation of the optimal number of calibrating frames with the frame number may be explained by respiration-induced chest wall excursions. The images reconstructed using the DCE-identified kernel support and the DCE-identified number of calibrating frames exhibit a significant reduction in noise and artifacts compared to those using the original TGRAPPA reconstruction parameters as indicated by the difference images of Figure 3.7. A quantitative assessment of the performances of these three strategies using MSE, shown in Figure 3.8, clearly demonstrates that the reconstruction using the DCE-identified kernel parameters outperforms the original TGRAPPA. The considerable difference between the two reconstructions is likely due to fact that 1) the kernel support was also optimized in the DCE optimized reconstruction and 2) our experimental dataset was acquired at a

relatively low rate (7 frames per second), making frame to frame variations more substantial and possible errors due to using more frames in the reconstruction larger.

Table 3-1 Comparison between reconstruction mean square error

Brain image errors of GRAPPA reconstructions obtained using: 4×5 support, 4×5 support with Tikhonov regularization, sparse-optimized k -space subset, CV-identified kernel, and the DCE-derived kernel supports, respectively.

ORF	# of ACS lines	Recon error (4x5)	Recon error (4x5 with regularization)	Recon error (SPARSE kernel)	Recon error (CV kernel)	Recon error (DCE kernel)	CV-identified kernel size	DCE-identified kernel size
2	2	1762	1026	808	690	690	2x3	2x3
	12	433	428	417	405	405	2x6	2x6
	24	395	394	383	362	362	4x7	4x7
	FULL	356	353	322	329	313	20x23	20x30
3	6	1109	937	546	502	502	2x5	2x5
	18	489	473	445	433	433	2x10	2x10
	36	440	438	428	419	414	4x9	4x12
	FULL	422	421	367	351	340	16x21	16x30
4	9	1501	1134	657	572	572	2x7	2x7
	24	649	583	521	483	483	3x11	3x11
	48	534	531	455	443	423	4x11	4x13
	FULL	503	501	386	370	356	16x19	16x26

The data consistency error introduced here is appropriate for characterizing and optimizing all k -space based parallel MRI reconstruction algorithms that assume the kernel to be partially or totally shift invariant in k -space. For example, DCE procedure can be applied to non-Cartesian reconstruction algorithms that divide the k -space into

sectors and assume shift-invariant sector-specific reconstruction kernels (24-28). In this case, the kernel parameters need to be optimized sector-wise and the sum of the resultant DCE values may be used.

3.6 Conclusions

In this paper, we have introduced a new data consistency error (DCE) that can be used for validating, characterizing, and optimizing k -space-based reconstruction in parallel imaging. DCE was applied to automatically select the optimal kernel support for GRAPPA reconstruction and the optimal set of frames for calibration process in TGARPPA reconstruction. Compared to existing kernel optimization methods, the result is an optimized tradeoff between artifacts and noise in the reconstructed images. The new data consistency error is easy to evaluate, robust for selecting reconstruction parameters, and can be applied to all k -space based parallel MRI reconstruction algorithms that assume the kernel to be partially or totally shift invariant in k -space.

3.7 Chapter 3 References

1. Larkman DJ, Nunes RG. Parallel magnetic resonance imaging. *Phys Med Biol* 2007; 52(7):R15-55.
2. Yeh EN, McKenzie CA, Ohliger MA, Sodickson DK. Parallel magnetic resonance imaging with adaptive radius in k -space (PARS): constrained image reconstruction using k -space locality in radiofrequency coil encoded data. *Magn Reson Med* 2005; 53(6):1383-1392.

3. Nana R, Zhao T, Heberlein K, Laconte SM, Hu X. Cross-validation-based kernel support selection for improved GRAPPA reconstruction. *Magn Reson Med* 2008; 59(4):819-825.
4. Qu P, Shen GX, Wang C, Wu B, Yuan J. Tailored utilization of acquired k -space points for GRAPPA reconstruction. *J Magn Reson* 2005; 174(1):60-67.
5. Samsonov AA. On optimality of parallel MRI reconstruction in k -space. *Magn Reson Med* 2008; 59(1):156-164.
6. Griswold MA, Jakob PM, Heidemann RM, Nittka M, Jellus V, Wang J, Kiefer B, Haase A. Generalized autocalibrating partially parallel acquisitions (GRAPPA). *Magn Reson Med* 2002; 47(6):1202-1210.
7. Golub G, Van Loan C. *Matrix computations*. Baltimore: Johns Hopkins University Press; 1983.
8. Cawley G. Leave-one-out cross-validation based model selection criteria for weighted LS-SVMs. *IEEE, Neural Networks, IJCNN '06 International Joint Conference on* 2006:1661-1668.
9. Breuer FA, Kellman P, Griswold MA, Jakob PM. Dynamic autocalibrated parallel imaging using temporal GRAPPA (TGRAPPA). *Magn Reson Med* 2005; 53(4):981-985.
10. Wang Z, Wang J, Detre JA. Improved data reconstruction method for GRAPPA. *Magn Reson Med* 2005; 54(3):738-742.
11. Hansen P. *Rank-deficient and discrete ill posed problems: numerical aspects of linear inversion*. Philadelphia: SIAM; 1998.

12. Johnston PR, Gulrajani RM. Selecting the corner in the L-curve approach to Tikhonov regularization. *IEEE Trans Biomed Eng* 2000; 47(9):1293-1296.
13. Griswold MA, Blaimer M, Breuer F, Heidemann RM, Mueller M, Jakob PM. Parallel magnetic resonance imaging using the GRAPPA operator formalism. *Magn Reson Med* 2005; 54(6):1553-1556.
14. Zhao T, Hu X. Iterative GRAPPA (iGRAPPA) for improved parallel imaging reconstruction. *Magn Reson Med* 2008; 59(4):903-907.
15. Blaimer M, Breuer FA, Mueller M, Seiberlich N, Ebel D, Heidemann RM, Griswold MA, Jakob PM. 2D-GRAPPA-operator for faster 3D parallel MRI. *Magn Reson Med* 2006; 56(6):1359-1364.
16. Blaimer M, Kellman P, Griswold MA. Dynamic parallel MRI using the temporal GRAPPA-operator (TGRAPPA-Operator). In: *Proceedings of the 15th Annual Meeting of ISRMRM, Berlin, Germany, 2007.* p.3339.
17. Nana R, Zhao T, Heberlein K, Zuehlsdorff S, Jerecic R, Hu X. Iterative GRAPPA (iGRAPPA) for dynamic parallel imaging. In: *Proceedings of the 16th Annual Meeting of ISRMRM, Toronto, Canada, 2008.* p.3668.
18. Willig-Onwuachi JD, Yeh EN, Grant AK, Ohliger MA, McKenzie CA, Sodickson DK. Phase-constrained parallel MR image reconstruction. *J Magn Reson* 2005; 176(2):187-198.
19. Qu P, Wang C, Shen GX. Discrepancy-based adaptive regularization for GRAPPA reconstruction. *J Magn Reson Imaging* 2006; 24(1):248-255.
20. Pruessmann KP, Weiger M, Scheidegger MB, Boesiger P. SENSE: sensitivity encoding for fast MRI. *Magn Reson Med* 1999; 42(5):952-962.

21. Lin FH, Kwong KK, Belliveau JW, Wald LL. Parallel imaging reconstruction using automatic regularization. *Magn Reson Med* 2004; 51(3):559-567.
22. Sodickson DK. Tailored SMASH image reconstructions for robust in vivo parallel MR imaging. *Magn Reson Med* 2000; 44(2):243-251.
23. Hoge WS, Brooks DH, Madore B, Kyriakos WE. A tour of accelerated parallel MR imaging from a linear systems perspective. *Concept Magn Reson A* 2005; 27A(1):17-37.
24. Samsonov AA, Block WF, Arunachalam A, Field AS. Advances in locally constrained k -space-based parallel MRI. *Magn Reson Med* 2006; 55(2):431-438.
25. Heberlein K, Hu X. Auto-calibrated parallel spiral imaging. *Magn Reson Med* 2006; 55(3):619-625.
26. Heidemann RM, Griswold MA, Seiberlich N, Kruger G, Kannengiesser SA, Kiefer B, Wiggins G, Wald LL, Jakob PM. Direct parallel image reconstructions for spiral trajectories using GRAPPA. *Magn Reson Med* 2006; 56(2):317-326.
27. Huang F, Vijayakumar S, Li Y, Hertel S, Reza S, Duensing GR. Self-calibration method for radial GRAPPA/k-t GRAPPA. *Magn Reson Med* 2007; 57(6):1075-1085.
28. Arunachalam A, Samsonov A, Block WF. Self-calibrated GRAPPA method for 2D and 3D radial data. *Magn Reson Med* 2007; 57(5):931-938.

**CHAPTER 4. PASSIVE TRACKING OF THE CALIBRATION
INFORMATION CHANGE USING DATA CONSISTENCY
ERROR TO IMPROVE RECONSTRUCTION EFFICIENCY
AND ACCURACY IN DYNAMIC PARALLEL IMAGING⁶**

In parallel dynamic imaging such as TGRAPPA [1], multiple adjacent time frames are merged to form the calibration dataset for the reconstruction of a given frame. In the TGRAPPA implementation, the reconstruction weights are determined for every time frame, which may result in long reconstruction times. In applications such as free breathing cardiac and abdominal imaging, the respiration induced coil sensitivity change is cyclic in time suggesting that multiple frames along the time course may have approximately the same calibration information. This chapter presents a simple passive approach that utilizes the data consistency error (DCE) introduced in chapter 3 to provide a goodness measure of the frame-to-frame coil sensitivity information change in parallel dynamic imaging. This tracking information is subsequently used to identify the frames sharing calibration dataset and avoiding using inconsistent calibrating frames, leading to an efficient and accurate reconstruction. The method is demonstrated using *in vivo* cardiac imaging data.

⁶ A manuscript has been prepared for the work in this chapter for publication in Magn Med Reson as “*Nana R, Hu X. Automatic Passive Tracking of the Frame-to-Frame Calibration Information Change To Improve Reconstruction Efficiency in Dynamic Parallel Imaging*”.

4.1 Introduction

Imaging a moving object with MRI often poses non-trivial challenges, as high acquisition speeds may be required to resolve or freeze its temporal variations. Parallel imaging (1) has been proposed to increase the imaging speed by acquiring just a fraction of needed data. Parallel imaging reconstructs the image from the reduced dataset by relying on prior knowledge about the array of receiver coil sensitivities. The coil sensitivity information is generally obtained through an additional reference experiment, thereby degrading the efficiency of the parallel imaging experiment. In dynamic application such as free breathing cardiac imaging with flexible cardiac matrix coils, the coil sensitivities change in time due to respiration induced chest wall movement. This poses an additional challenge to parallel imaging since sensitivity mismatch may be present between the reference data and the data of each time frame.

The generalized auto-calibrating partially parallel acquisition (2,3) has been recently extended to dynamic experiments that are performed with an interleaved acquisition scheme (4,5) such that the sensitivity information necessary for reconstruction is directly obtained from the actual accelerated data. This so called temporal GRAPPA (6) permits the realization of the full image acceleration since several adjacent undersampled time frames can be merged to form the full calibration dataset for the GRAPPA reconstruction of a given frame. In this original implementation of TGRAPPA, the reconstruction weights are determined for every time frame, which may result in long

total reconstruction times. Since respiration induced coil motion generally occurs more slowly as compared to the frame acquisition rate, it has been suggested that the reconstruction coefficients may be updated much less frequently in order to improve the overall reconstruction time without significant degradation of the image quality (6). However, finding how often the weights need to be updated may not be a simple task as this may vary with acquisition conditions. In principle, the knowledge of the respiratory induced chest displacement, generally cyclic, may help improve both the calibration and the total reconstruction time since many frames along the time course may carry approximately the same sensitivity information.

This chapter presents a method that utilizes a recently introduced data consistency error (DCE) metric (7), which provide a simple measure of reconstruction error of k -space interpolation for Cartesian parallel imaging, to provide a consistency measure of the frame-to-frame calibration information in parallel dynamic imaging. This tracking information is subsequently used to identify the frames sharing calibration dataset and avoiding using inconsistent calibrating frames, leading to an efficient and accurate reconstruction. The method is demonstrated using *in vivo* cardiac imaging data.

4.2 Methods

4.2.1 Review of DCE

DCE was recently introduced to provide a simple measure of reconstruction error of k -space interpolation for Cartesian parallel imaging (7). It has been proven useful to

select parameters for an optimal reconstruction. It is defined as the mean square difference between the acquired data and their estimates obtained by interpolation of the estimated missing data. The missing data and the predicted acquired data are interpolated using the same kernel (shift invariance property of the kernel). The implementation steps for computing GRAPPA-type DCE are as follows: (I) Derive the GRAPPA weights using the calibration information; (II) Fill in the missing lines of all coils; (III) Predict the acquired lines from the filled missing lines using the same GRAPPA weights; (IV) Compute the mean square difference between the acquired lines and their estimates. In this study, the calibration dataset is the varying information used to track the coil sensitivity information relative changes in time using DCE.

4.2.2 Segmenting the time frames based on their calibration information

In our implementation of the frame-to-frame calibration information tracking procedure, the set of interleave-undersampled frames is divided into blocks starting from a designated reference frame and expanding along the time course as indicated in Fig. 4.1. A block consists of R consecutive frames with distinct sampling patterns. DCE values of the reference frame are calculated for each block used as the calibration dataset. We assume that each DCE value provides a simple measure of the sensitivity mismatch that exists between the reference frame and the frames of a given block and therefore reflects the coil sensitivity changes. During the calculation of DCE, the mean square error between the images reconstructed from the under-sampled and fully sampled reference frame, respectively, is output for comparison. Assuming the coil sensitivity changes smoothly in time and that the acquisition rate is constant, the DCE values reflecting the

sensitivity mismatch between a given frame and the reference frame is determined by linear interpolation of the block-based DCE values of the reference frame. The relative change of DCE values within which the frames are assumed to share the same calibration information is chosen empirically to be the average of the differences between the DCE values of two consecutive frames in the time course. The time frames sharing the calibration information are merged to derive the reconstruction weights which are subsequently used to reconstruct each of them.

4.2.3 Data acquisition and reconstruction

Non-gated free breathing cardiac experiments were performed on a 1.5T Siemens Avanto with a 15-channel cardiac matrix coil using a trueFISP sequence. Fully sampled short-axis view cardiac data were acquired at a rate of 7.80 fps on healthy subjects (TR = 2.29 ms, TE = 1.15 ms, flip angle = 70° , slice thickness = 8 mm, FOV = 360×264.38 mm, matrix = $256 \times 56 \times 15$) and later downsampled in a time-interleaved phase-encoding (PE) scheme as described in (6). Additionally, truly accelerated outflow track cardiac view data were acquired at rates 10.73 fps (R = 2), 16.09 fps (R = 3), and 21.45 fps (R = 4). The common acquisition parameters for the accelerated data were: TR = 2.39 ms, TE = 1.02 ms, flip angle = 71° , slice thickness = 6 mm, FOV = 350×263 mm, and matrix size = $176 \times 78 \times 15$.

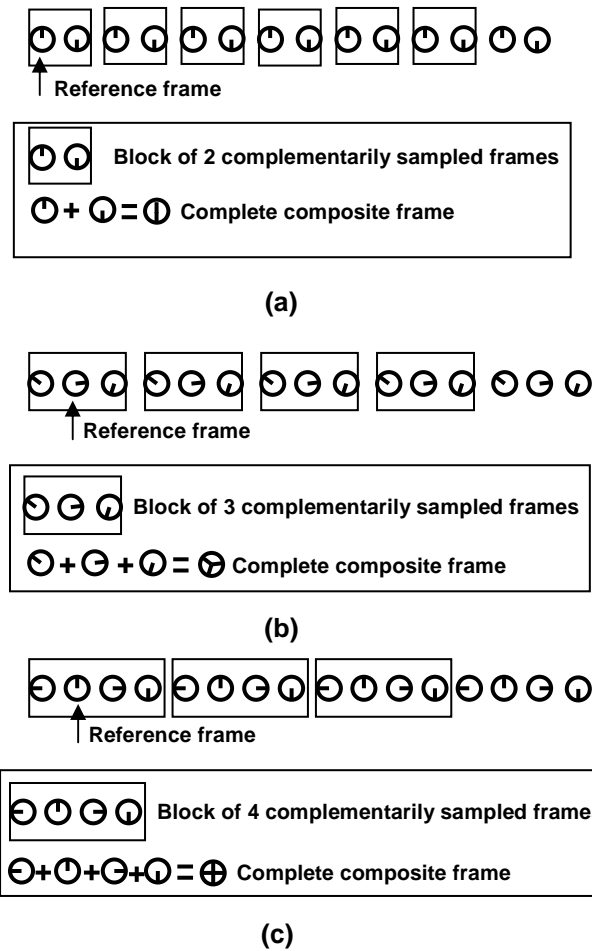


Figure 4.1 Formation of the blocks of frames to be examined by DCE

(a) $R = 2$; (b) $R = 3$; (c) $R = 4$. $R-1$ complimentary sampled frames neighboring the reference frame are selected to form the reference block of R consecutive frames. Depending the position of the reference frame, this process is repeated by expanding along the time course in both directions. Other configurations of the block are possible (position of the reference frame within the reference block).

The sensitivity tracking procedure described previously was applied to the accelerated cardiac datasets to identify the frames that share approximately the same calibration information. For the offline-accelerated dataset, the reconstruction mean square error (MSE) was output during the DCE computation for comparison. Here MSE

is defined by $MSE = \sum_n^N |I(n) - I_{ref}(n)|^2 / N$ where I represents the GRAPPA

reconstructed image, I_{ref} is the full-data reconstructed image, N is the total number of pixels, and n is the pixel index. The optimized TGRAPPA reconstruction was compared to the original TGRAPPA. In all TGRAPPA reconstructions, the full extent of the k -space calibration data was used to derive the GRAPPA weights. All algorithms were implemented in MATLAB (The Mathworks Inc., Natick MA, USA) on a Pentium 4 CPU 2.00 GHz computer with 1GB RAM.

4.3 Results

Figures 2a, 2c, and 2e present the dependence of DCE values on the block of frames generated according to Figure 4.1 for cardiac datasets offline downsampled at $R = 2$, $R = 3$, and $R = 4$ respectively. The plots were generated using four different kernel supports corresponding to 2×5 , 2×9 , 4×5 and 4×9 as indicated by the legend. The shape and locations of the peaks and valleys along the block of frames axis of each DCE plot virtually match those of the corresponding MSE plot (Figs. 3b, 3d, and 3f) obtained under the same conditions.

Application of our frame segmentation procedure on the DCE plot of any of the kernel support results to 14 groups of frames for $R = 2$, 9 groups of frames for $R = 3$, and 7 groups of frames for $R = 4$. Figure 4.3 presents short axis view cardiac images reconstructed using (b) the original and the (c) optimized TGRAPPA. These frame images were picked from the same group but are located at different phases of the DCE plots. In all cases, a 4×5 kernel was used. The reconstructed images are displayed with

the same windowing setting for comparison. Below each reconstructed image, its absolute difference from the full-data reconstructed image (a) is displayed, with a windowing setting that is much lower than that for the reconstructed image. A quantitative comparison between the two reconstructions is illustrated by the MSE plots of Figure 4.4 generated for all frames and for different acquisition schemes: (a) $R = 2$, (b) $R = 3$, and (c) $R = 4$.

The dependence of DCE on the block of frames for a truly accelerated data is shown in Figure 4.5 for three acceleration factors and for four kernel supports. Examples of images reconstructed by the two strategies are illustrated in Figure 4.6. Below each reconstructed image, a magnified copy of the image is shown to demonstrate the significant reduction in the background artifacts from undersampling when the optimized reconstruction is used. The segmentation of the frames using our tracking strategy lead to 13, 11, and 14 groups for acceleration factor of 2, 3, and 4 respectively for all four kernel supports used. The total computation times of these two strategies are summarized in table 4.1.

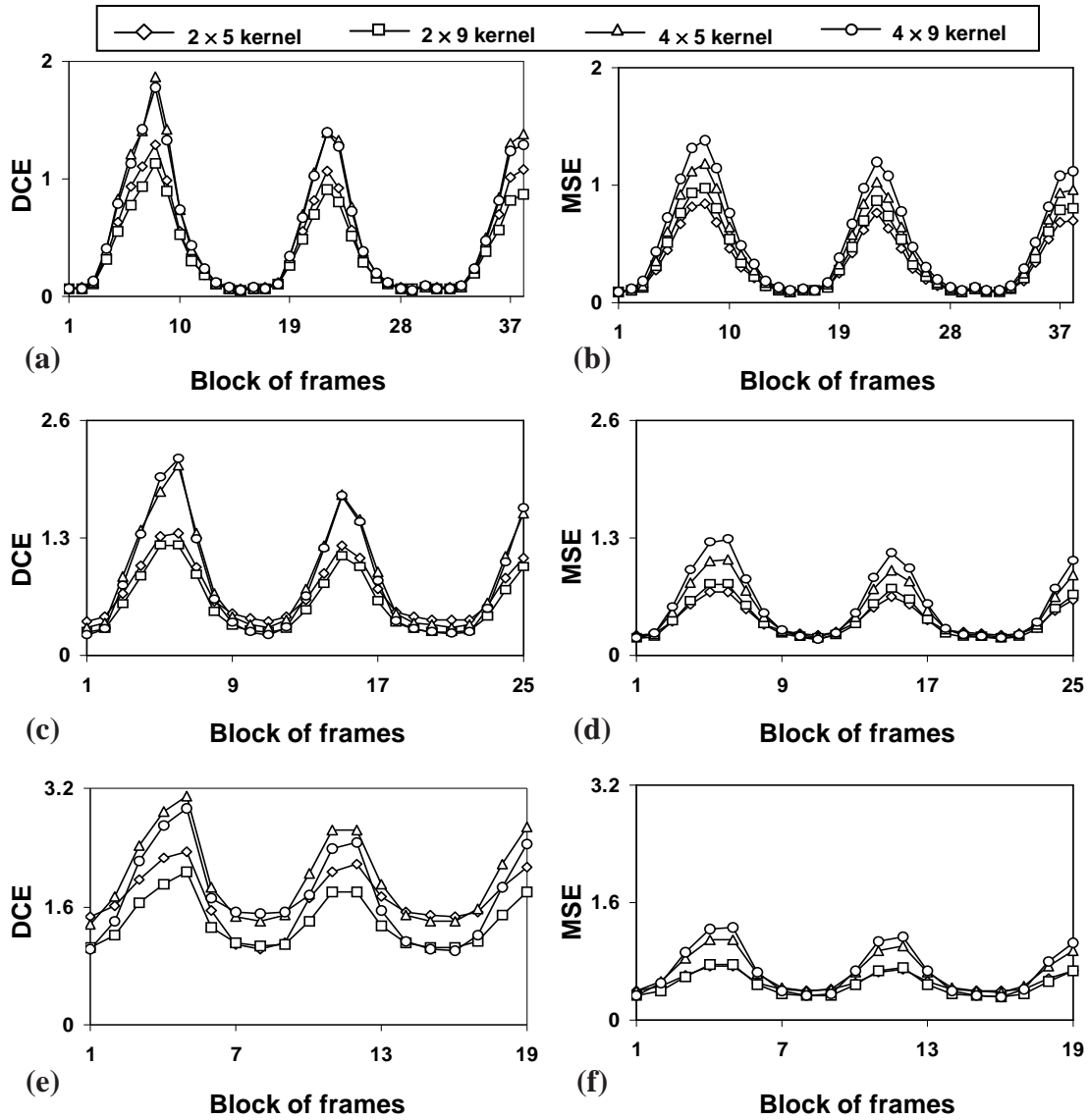


Figure 4.2 Dependence of DCE and MSE on the block of frames

Plots of DCE (a, c, and e) and MSE (b, d, and f) computed on the offline downsampled dynamic dataset as a function of block of frames. The three rows correspond to 3 parallel MRI settings, $R = 2$ (top), $R = 3$ (center), and $R = 4$ (bottom). Four different kernel supports corresponding to 2×5 , 2×9 , 4×5 and 4×9 were used as indicated by the legend.

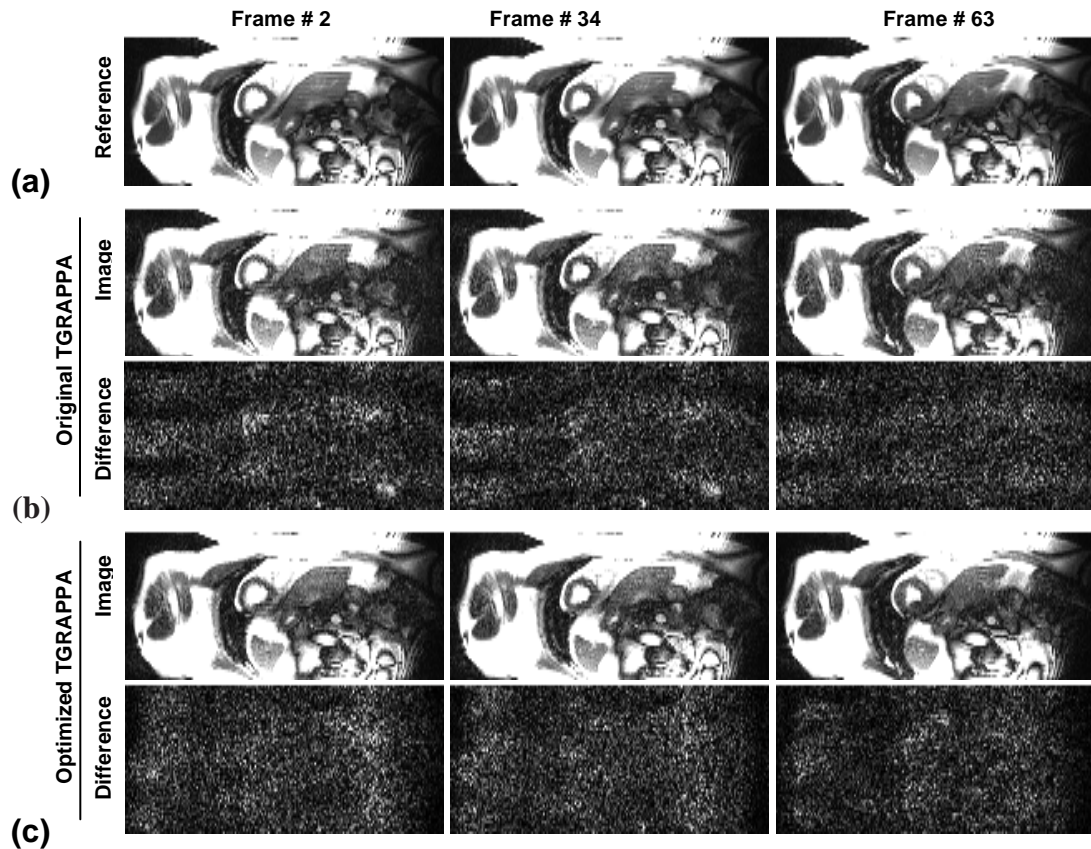


Figure 4.3 Comparison between reconstructed images

(a) Non-accelerated images used as reference, (b) original, and (c) optimized TGRAPPA reconstructed images ($R = 3$). The absolute difference of each reconstructed image with the non-accelerated image is shown right below the reconstructed image.

4.4 Discussion

The plots of Figs. 2 show a strong correspondence between DCE and MSE, a similarity consistent throughout the data used in this study and also consistent with the observations reported in ref. (7). These plots exhibit a cyclic pattern, indicative of respiration-induced changes. Additionally, the numbers of cycles (≈ 2.25) on all plots of Figure 4.2 are identical, indicating that our time frames arrangement strategy of the

offline downsampled datasets does not affect the number of respiration cycles with which the original fully sampled data were acquired. Furthermore, there is a strong similarity between the shapes of the plots generated using different kernel supports as indicated by the plots of Figs. 2 and 5, suggesting that our tracking strategy is independent of the kernel support. All these findings corroborate with our assumption that the DCE values of the reference frame reflect the sensitivity mismatches that exist between the reference frame and the block of frames.

The images reconstructed using the optimized TGRAPPA show a noticeable quality improvement over those reconstructed using the original TGRAPPA as indicated by the difference images of Figure 4.3 and the zoomed regions of reconstructed images of Figure 4.6. This performance is further confirmed by the results of Figure 4.4 which compares the MSE of the two strategies on the entire dynamic datasets. It is important to mention the overall low quality reconstructed images from the offline downsampled datasets as compared to that of the truly accelerated datasets for both reconstruction strategies. The smoothness of DCE plots of the truly accelerated datasets as compared to those downsampled offline goes along with this observation. This is understandable because downsampling dynamic datasets offline does not change the sensitivity mismatches that already exist between fully acquired frames (and eventually between lines of a frame) but, instead, can only complicate this sensitivity mismatch when the undersampled data are merged (even with a minimal number of frames) to derive the calibration information. The offline datasets were used just for simulation to confirm the correspondence between DCE and MSE in the present context and to provide a quantitative comparison of the image qualities obtained by the two strategies.

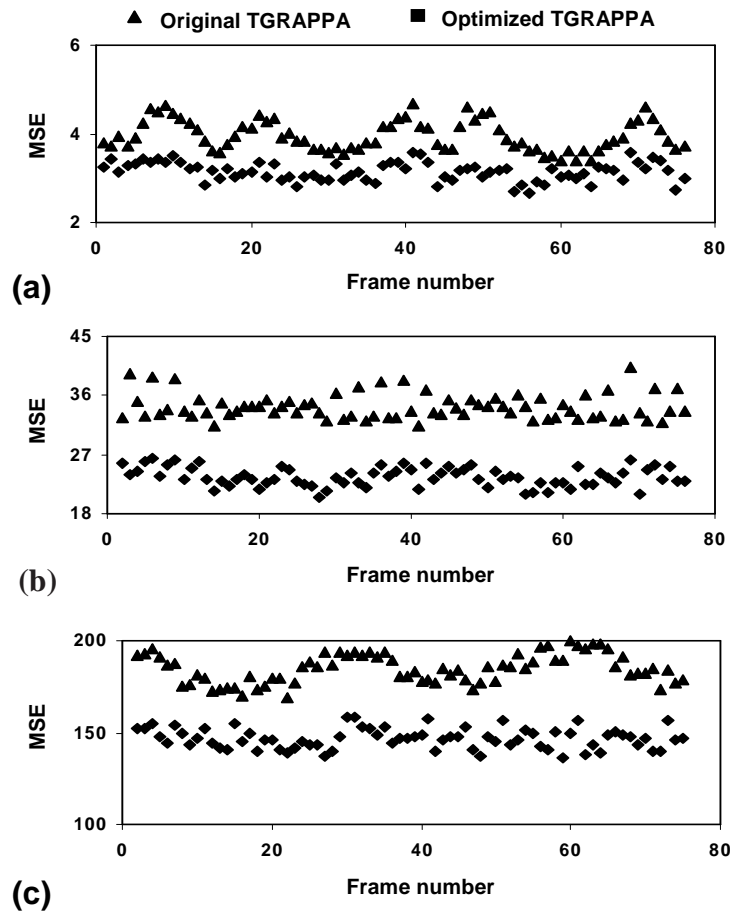


Figure 4.4 Quantitative comparison between TGRAPPA reconstructions

MSE is plotted as a function of frame number for three parallel MRI settings

(a) $R = 2$, (b) $R = 3$, (c) $R = 4$.

The optimized TGRAPPA results in considerably reduced total reconstruction times compared to the original TGRAPPA as indicated in table 1. In the original TGRAPPA, more time is spent in the reconstruction weights estimation which normally increases with kernel size, acceleration factor, and number of ACS lines. This justifies the increase of the difference in computational time at higher acceleration factors. The optimized TGRAPPA total reconstruction time can be considerably reduced by restricting

the computation of DCE in the center part of k -space (as opposed to the entire k -space as done in study) or/and by increasing the range of DCE values within which the frames are assumed to share the same sensitivity information, provided that this increase does not adversely affect the quality of the images. The computational time difference between these two strategies is expected to increase with increasing number of frames.

The DCE range within which the frames are assumed to share the same sensitivity information has been chosen empirically to be the average of the differences between the DCE values two consecutive frames the time course. This choice prioritizes blocks of frames located at different phases along the time course over neighbor consecutive blocks. This choice also takes into account the variability that may exist in the respiration rate and is therefore adaptable to a given dynamic dataset. Other ranges may be envisioned. For example, choosing the range to be 5% of the dynamic range of all DCE values seemed to produce comparable results (not shown) for all the data analyzed in this study. However, this fixed percentage may be inappropriate for datasets acquired under other conditions.

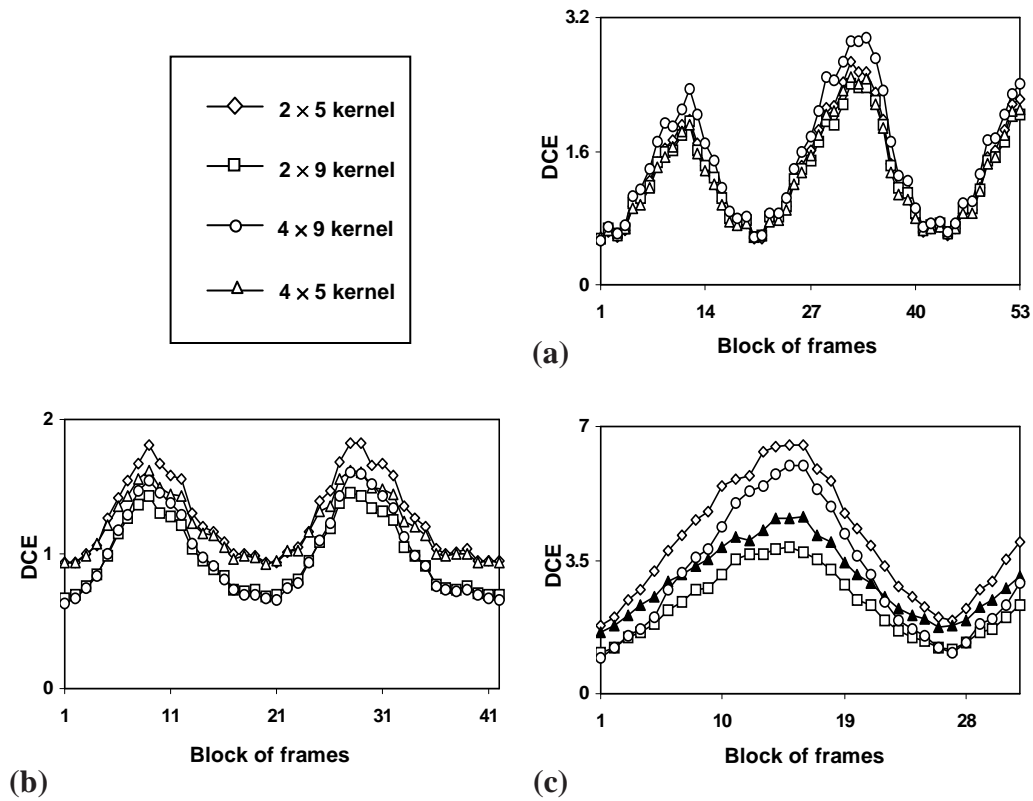


Figure 4.5 Dependence of DCE on block of frames on the truly-accelerated outflow track cardiac view dataset

The three rows correspond to 3 parallel MRI settings, $R = 2$ (top), $R = 3$ (center), and $R = 4$ (bottom). Four different kernel supports corresponding to 2×5 , 2×9 , 4×5 and 4×9 .

Table 4-1 Comparison between the total reconstruction times (in sec)

	R = 2 107 frames	R = 3 128 frames	R = 4 128 frames
Original TGRAPPA	312	461	514
Optimized TGRAPPA	213	267	243

It is important to note that the use of any other frame (except the last frame for $R = 2$, the first frame and the last frame for $R = 3$, and the first frame and the last two

frames for $R = 4$, due to our proposed block configuration) as the reference frame did not significantly affect the results presented in this study. However, it should also be noted that once the reference frame is chosen there may be many possible block configurations (different positions possible of the reference frame in the reference block). Our proposed block configuration follows a locality criterion, which suggests that the sensitivity mismatch between two frames within the same respiration phase diminishes with decreasing distance (in time) between the two frames, i.e. selected frames that make up the reference block should be as close as possible to the reference frame. This is understandable because the frame acquisition rate is generally constant and coil motion caused by respiration varies smoothly. Nonetheless, we have investigated all other possible configurations and did not see any advantage over the proposed configuration.

The number of frames carrying approximately the same sensitivity information increases with the number of respiratory cycles covered during data acquisition, potentially leading to better reconstruction as a result of improved SNR of the calibration dataset. However it is important to point out that if a dynamic dataset is acquired during less than half of a respiration cycle, the calibration dataset may only contain the strict minimum number of frames (equal to the acceleration factor), and in this case there is no guarantee that our propose method can produce better result than the original TGRAPPA. In such a rare situation, the original TGRAPPA reconstruction is advised. Additionally, for real-time on-the-fly image reconstruction, our method would require a delay of at least a respiration cycle. If online reconstruction is the main interest (i.e. no need to improve the image quality), then our proposed sensitivity tracking strategy can be

coupled with the original TGRAPPA just to determine how often the reconstruction weights need to be updated. In this case the knowledge of the preset threshold DCE value, under which the reconstruction weights do not need to be updated, is required. This threshold could be a percentage change of the DCE value of the block from which the new set of reconstruction weights is derived.

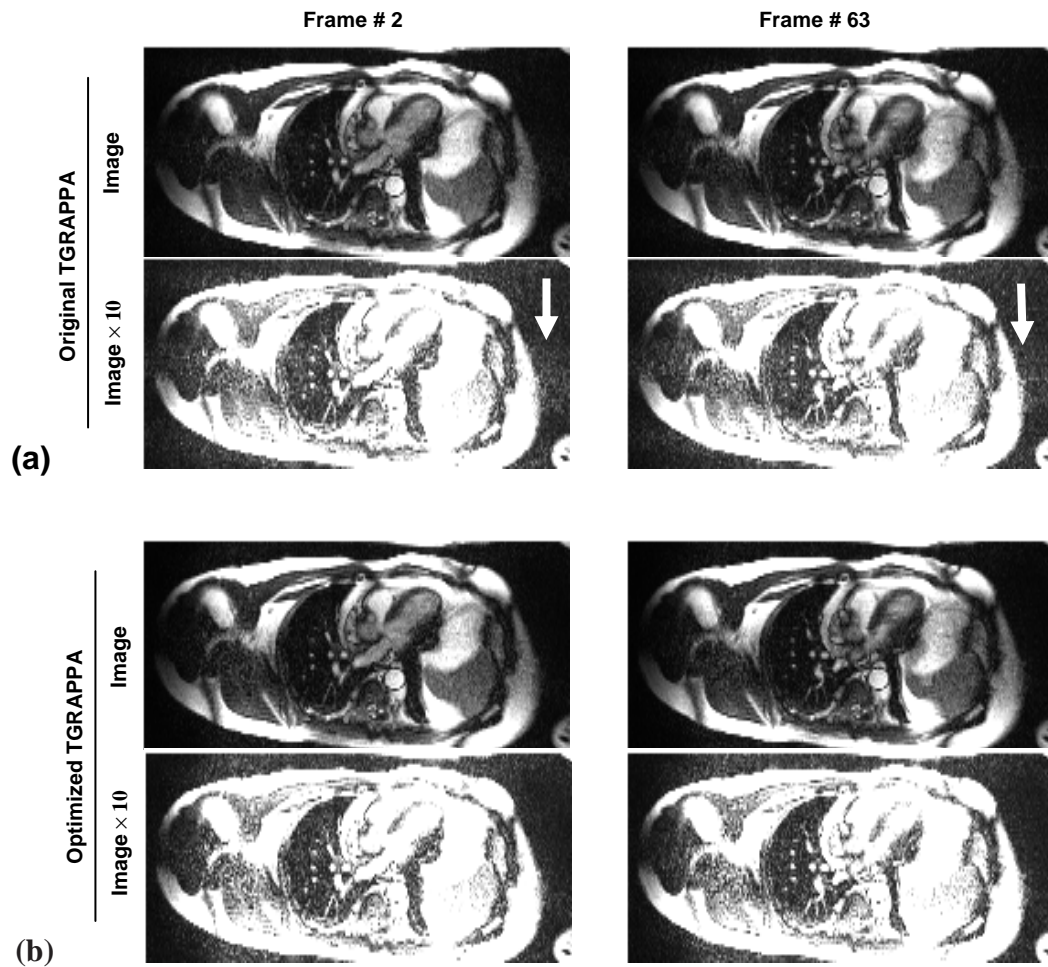


Figure 4.6 Reconstruction results of two different outflow track view frames ($R = 3$)

(a) original and (b) optimized TGRAPPA reconstructed images. Below each reconstructed image, a magnified copy of the image is shown to demonstrate the significant reduction in the background artifacts (indicated by the arrows) from undersampling.

An alternative to our blockwise arrangement of the dynamic dataset, which only considers R consecutive frames along the time course, is to form the set of blocks without any restriction by combining the reference frame with all possible combinations of $R-1$ complimentary frames that exist within the dynamic dataset. The implementation of this strategy did not show any noticeable image quality improvement on our proposed method but added a considerable computational time penalty. This is understandable because the respiration occurs much more slowly than the actual frame acquisition rate.

4.5 Conclusions

We have introduced and demonstrated a strategy that can be used to passively extract a goodness measure of the frame-to-frame relative sensitivity information change in order to improve reconstruction efficiency of TGRAPPA in free breathing cardiac imaging. Compared to the original TGRAPPA reconstruction, the proposed method results to a considerably reduced total reconstruction time while improving or at least maintaining the image quality.

4.6 Chapter 4 References

1. Larkman DJ, Nunes RG. Parallel magnetic resonance imaging. *Phys Med Biol* 2007;52(7):R15-55.

2. Griswold MA, Jakob PM, Heidemann RM, Nittka M, Jellus V, Wang J, Kiefer B, Haase A. Generalized autocalibrating partially parallel acquisitions (GRAPPA). *Magn Reson Med* 2002;47(6):1202-1210.
3. Wang Z, Wang J, Detre JA. Improved data reconstruction method for GRAPPA. *Magn Reson Med* 2005;54(3):738-742.
4. Madore B, Glover GH, Pelc NJ. Unaliasing by fourier-encoding the overlaps using the temporal dimension (UNFOLD), applied to cardiac imaging and fMRI. *Magn Reson Med* 1999;42(5):813-828.
5. Kellman P, Epstein FH, McVeigh ER. Adaptive sensitivity encoding incorporating temporal filtering (TSENSE). *Magn Reson Med* 2001;45(5):846-852.
6. Breuer FA, Kellman P, Griswold MA, Jakob PM. Dynamic autocalibrated parallel imaging using temporal GRAPPA (TGRAPPA). *Magn Reson Med* 2005;53(4):981-985.
7. Nana R, Xiaoping H. Automatic time frames subset selection for improved TGRAPPA reconstruction. In: *Proceeding of the ISMRM, Toronto; 2008; p 1266.*

CHAPTER 5. NON-CARTESIAN PARALLEL IMAGE RECONSTRUCTION WITH DECONVOLUTION OF UNDER-SAMPLED GRIDDING (DUG) IN k -SPACE⁷

In this chapter, a new algorithm is introduced to further improvements in computation times and reconstruction efficiency for parallel imaging using non-Cartesian trajectories. The new method, non-Cartesian parallel image reconstruction with deconvolution of under-sampled gridding (DUG), operates on gridded k -space and exploits the energy distribution during the gridding process to segment the gridded data for an efficient k -space interpolation. Compared to existing methods, DUG results in an improved and faster reconstruction. The effectiveness of the method is demonstrated with *in vivo* spiral and radial data.

5.1 Introduction

Parallel imaging is currently an integral part of magnetic resonance imaging owing to its ability to increase the acquisition speed while reducing imaging artifacts and the specific absorption rate (SAR). To date, most parallel imaging approaches are based on

⁷ A manuscript has been prepared for the work in this chapter for publication in Magn Reson Med as “Nana R, Zhao T, Hu X. *An Efficient and Reliable GRAPPA Reconstruction method for non-Cartesian Parallel Imaging*”. Preliminary results have been presented as “Zhao T, Nana R, Hu X. *An efficient and General GRAPPA method for non-Cartesian Parallel Imaging*. 15th Annual Meeting ISMRM; 2007; Berlin, Germany. P 337.” TZ was responsible for implementing the main idea while RN was responsible for developing the theory and simulation that support the idea, optimizing the GRAPPA reconstruction weights, and applying the strategy to radial trajectory.

sampling on Cartesian grid in the k -space and the sampling reduction is applied mostly along the phase-encoding direction(s) (1). Depending on the applications, non-Cartesian trajectories may be advantageous and desired (2-7). For parallel imaging, non-Cartesian trajectory has the added advantage in that the reduction in spatial encoding can be achieved in multiple directions naturally. However, parallel imaging with non-Cartesian trajectories is somewhat hampered by the difficulty in reconstruction.

Parallel image reconstruction with Cartesian sampling is relatively simple, owing to its shift-invariance property in either the image space or the k -space. With non-Cartesian trajectory, parallel image reconstruction becomes more difficult as the shift invariance is no longer present. In the image domain, aliasing for non-Cartesian k -space trajectories is highly complex, as every pixel can contain a contribution from all other pixels in the entire field of view (FOV). While direct inversion to simultaneously solve for the true pixel intensities is possible in principle, it is computationally impractical.

Iterative solutions of the matrix inversion have been proposed (8,9), but these methods tend to be somewhat time consuming. Several k -space approaches, which do not require iteration, have also been proposed. With these methods, missing k -space data points are estimated through interpolation of the acquired data. Most of these are based on either PARS (9) or GRAPPA (10). The main difference between the two is that the former explicitly utilizes sensitivity maps in deriving the reconstruction weights while the latter uses k -space calibration data. In PARS, the reconstruction kernel can be dependent on the k -space location in general and can be applied to arbitrary k -space sampling. An

extension of this approach in which a reduced number of kernels are used is possible (11).

In GRAPPA, the reconstruction kernels derived with calibration measurements implicitly account for coil-sensitivity information. In the Cartesian case, shift-invariance in the k -space is utilized such that a single globally invariant kernel can be used to synthesize missing signals with a given shift in the k -space relative to the acquired signals. In the case of non-Cartesian k -space trajectories (e.g. radial and spiral trajectories), the kernels are no longer shift invariant, and rigorous GRAPPA reconstruction requires different reconstruction kernels for each missing datum because an invariant kernel is not applicable. Consequently, the reconstruction process can be very time consuming, and the use of GRAPPA is limited in non-Cartesian sampling. To overcome this difficulty, several authors have proposed dividing the k -space into sectors and assuming the kernel within each sector to be approximately the same (12-14). This segmentation of the k -space exploits the radial symmetry inherent to spiral and radial trajectories. In these methods, the missing data are first GRAPPA synthesized followed by a gridding (15,16) process that interpolates the non-Cartesian data onto a rectilinear grid. Transforming the accelerated data onto Cartesian grid following with GRAPPA interpolation has also been proposed (17,18).

A successful non-GRAPPA, non-PARS, and non-iterative based k -space algorithm has been recently introduced which formulates the reconstruction problem as a system of sparse linear equations in k -space from which the solution is obtained by computing a

sparse approximation inverse matrix. The method suffers from a considerable computational load (even heavier than that of iterative SENSE (8)) for a single image reconstruction but may be useful for applications that require repetitive measurement such as functional MRI (19) and diffusion tensor imaging (20,21) since the results of the first reconstruction can be applied to reconstruct subsequent images in a relatively shorter time.

Despite the successes of the existing algorithms, no commercial scanner currently supports reconstruction of undersampled non-Cartesian k -space data. This suggests that it remains a challenge to efficiently reconstruct an image from undersampled non-Cartesian k -space data. This chapter presents an efficient and reliable reconstruction strategy for parallel imaging with a strong potential of online reconstruction. The method operates on gridded k -space and exploits the energy contribution of each acquired signal during the gridding process to identify each group of gridded k -space data that can be synthesized with the same reconstruction kernel. As it turns out, the number of kernels per coil necessary to synthesize the gridded data can be reduced to the acceleration factor, leading to a computational effort (excluding the calculation of the gridding table) comparable to normal Cartesian GRAPPA. The basis of the gridded k -space data segmentation for efficient reconstruction is first provided through simulation. Then the effectiveness of the new method, non-Cartesian parallel image reconstruction with deconvolution of under-sampled gridding (DUG), is demonstrated on *in vivo* data and compared to segmented GRAPPA (12,14).

5.2 Theory

Conventional convolution gridding methods (16) assume that the non-Cartesian data fulfill the Nyquist criterion at all k -space locations. Therefore, applying gridding on undersampled non-Cartesian data may add gridding errors and thereby complicate the parallel MRI reconstruction problem. In this section, we first demonstrate that it is possible to apply a weighted average interpolation described by a kernel on data that has been gridded using conventional gridding approach to generate an artifact free image. Because our demonstration builds upon the PARS(9) formulation, a brief review of PARS reconstruction is provided first.

5.2.1 Review of PARS reconstruction

The l^{th} receiver coil of L , with sensitivity $h_l(r)$, $l = 1, \dots, L$, collects signal from an object $f(r)$ over a volume of interest (VOI) at the k -space position k_u that can be represented by

$$s_l(k_u) = \int_{\text{VOI}} e^{ik_u \cdot r} h_l(r) f(r) dr \quad [5.1]$$

In this article, it assumed that the signal is sampled on non-Cartesian grids described by k_u . In PARS, an un-acquired datum of a given coil can be synthesized by linearly combining acquired signals from all coil data and the final image can be obtained by root sum of squares of individual coil images. This procedure can be mathematically represented by

$$s_l(k_c) = \sum_{u \in \Pi_{c,D}} \sum_{l'=1}^L w_{u,l'}^{(l)}(k_c) s_{l'}(k_u), \quad [5.2]$$

where k_c represents the k -space position of the Cartesian sample to be determined that provides a predefined FOV and resolution, respectively. $\Pi_{c,D}$ is the set of k -space samples, within the radius D , participating in the synthesis of k_c , i.e. $\Pi_{c,R} = \{n : \|k_c - k_u\| \leq D\}$ and $\|\cdot\|$ is the Euclidean norm. $s_l(k_c - \Delta k_u)$ is the l^{th} datum acquired at a relative shift $\Delta k_u = k_c - k_u$ from k_c , $w_{u,l}^{(l)}(k_c)$ are reconstruction weights for the synthesis of the un-acquired point k_c of the l^{th} receiver. The weighting coefficients are calculated by performing a least-squares fit that satisfies the following equation:

$$\sum_{u \in \Pi_{c,z}} \sum_{l=1}^L w_{u,l}^{(l)}(k_c) e^{i(k_c - \Delta k_u)} h_l(r) \approx h_l(r) \quad [5.3]$$

These weights can also be derived directly in k -space by fitting the acquired k -space data to auto-calibration signals (ACS) which can be simply the densely sampled k -space center available for many trajectories such as radial and variable density spirals or an external calibration scan (11). This is accomplished by solving the equation

$$\mathbf{s}_l^{ACS} = \mathbf{E} \mathbf{w}_l \quad [5.4]$$

where \mathbf{s}^{ACS} is a column vector of calibration signal values obtained by the l^{th} coil, \mathbf{w}_l is the column vector of weights necessary to reconstruct the point k_c , and \mathbf{E} is the encoding matrix whose elements are defined by

$$[\mathbf{E}]_{x,(n,l)} = s_l(k_x - \Delta k_n) \quad [5.5]$$

where $x \in \Omega$, Ω being the ensemble of all k -space positions contoured by the calibration region, i.e. the Fourier domain of the l^{th} coil sensitivity map. Note that the sub-indexes x , (n, l) emphasize that the matrix \mathbf{E} has dimensions length of $\Omega \times (\text{length of } \Pi_{c,D} \times L)$.

5.2.2 Post-gridding k -space interpolation

Eq.[5.5] suggests that construction of the encoding matrix E amounts to re-sampling $s_l(k)$, which may be efficiently implemented using gridding (11). This suggests

that the PARS operator $\sum_{l'=1}^L \sum_{u \in \Pi_{c,D}} w_{u,l'}^{(l)}(k_c)$, which transforms non-Cartesian accelerated

data onto aliasing free full Cartesian data, can be represented by a product of a mono-

channel gridding operator $\sum_{m \in \Pi_{x,D'}} g_{x,m}$, which transforms a coil non-Cartesian accelerated

data onto aliased Cartesian data, and a multi-channel weighted average operator

$\sum_{l'=1}^L \sum_{n \in \Pi_{c,D''}} w_{n,l'}^l(k_c)$, which synthesizes a gridded datum by linearly combining gridded data

from all coils. This can be represented mathematically by

$$\sum_{l'=1}^L \sum_{u \in \Pi_{c,D}} w_{u,l'}^{(l)}(k_c) \approx \sum_{l'=1}^L \sum_{n \in \Pi_{c,D''}} w_{n,l'}^l(k_c) \cdot \sum_{m \in \Pi_{x,D'}} g_{x,m} \quad [5.6]$$

where D' and D'' are the gridding and the weighted average interpolation kernel widths, respectively. Therefore, Eq. [5.2] can be rewritten as

$$s_l(k_c) = \sum_{u \in \Pi_{c,D}} \sum_{l'=1}^L w_{u,l'}^{(l)}(k_c) s_{l'}^G(k_c - \Delta k_{c'}) \quad [5.7]$$

where $k_{c'}$ describes the Cartesian positions of the gridded data, $s_{l'}^G(k_c - \Delta k_{c'})$ is the l'^{th} coil gridded signal at a relative shift $\Delta k_{c'} = k_c - k_{c'}$ from k_c . The formulation in Eq. [5.7] requires all coil data to be gridded onto Cartesian grid before the weighted average interpolation.

The implication of Eq.[5.7] is that a weighted average interpolation can be applied to remove aliasing from the gridded data while recovering the errors induced by applying gridding on data that violate Nyquist condition. Note that in Eq. [5.7], the interpolation weights are still location dependent and calibrating the reconstruction for each k -space sample would be very time consuming. A segmentation strategy for efficient interpolation is therefore necessary.

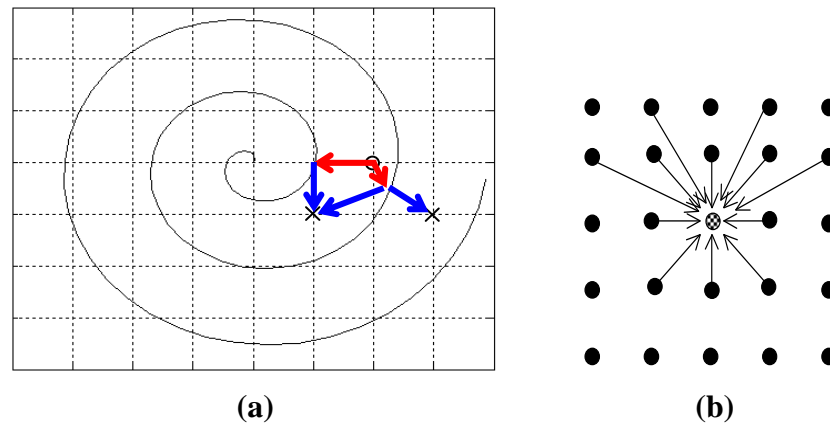


Figure 5.1 Analysis procedure of the energy distribution during gridding

(a) A unit signal located at a source point (o) is sinc interpolated onto the spiral grids (indicated by the red arrows). Then the interpolated signals are gridded onto several target Cartesian grid points (x) including the source point (indicated by the blue arrows). Repeating this process for all Cartesian grid points permit to generate maps which describe these grid points contribute to each other. (b) For each gridded point, a 5×5 neighborhood is examined.

5.2.3 Segmenting the gridded k -space data for efficient reconstruction

In a conventional gridding process, the non-Cartesian data are convolved with a window such as the Kaiser-Bessel function window (15). Segmenting the data gridded from an under-sampled non-Cartesian trajectory for efficient reconstruction requires a detail analysis of the energy distribution during the gridding process. A simulation study

was conducted to capture the dependence of the gridded k -space data points from under-sampled non-Cartesian data on original rectilinear k -space data. To this end, an impulse located at a given Cartesian point (denoted as source point) was first sinc interpolated to generate the non-Cartesian trajectory data and the non-Cartesian trajectory data, with missing segments zero-filled, were gridded to the Cartesian grids (target points) using a Kaiser-Bessel function window (e.g. Figure 5.1a). Repeating this process for every Cartesian point mapped out their contributions to each gridded point. Assuming this to be local, the contributions to each gridded point from a local neighborhood of 5×5 (Figure 5.1b) were examined and are shown in Figure 5.2. When there is no under-sampling, the contribution maps are uniform in the k -space (see Fig. 5.2a). When the spiral trajectory is under-sampled (Fig. 5.2b and 5.2c), the contribution maps exhibits a pattern similar to the sampling trajectory, with the grid points closer to acquired segments receiving more contribution. The cross-sectional profiles displayed on the top of each figure indicate that these contributions can be represented by steps, depending on the gridded point's distance from the sampled trajectory, with the number of steps equal to the reduction factor R . Dividing each map by the central map leads to relative contribution maps that are virtually uniform (Figs. 5.3a and 5.3b), suggesting that the grid points corresponding to the same step in the profile can be deconvolved with the same kernel. Similar results were obtained with radial trajectory (Figure 5.4). In other words, if gridding is applied to under-sampled spiral and radial trajectories, R (acceleration factor) interpolation kernels (DUG kernels) are sufficient to deconvolve the aliased gridded k -space data for proper reconstruction.

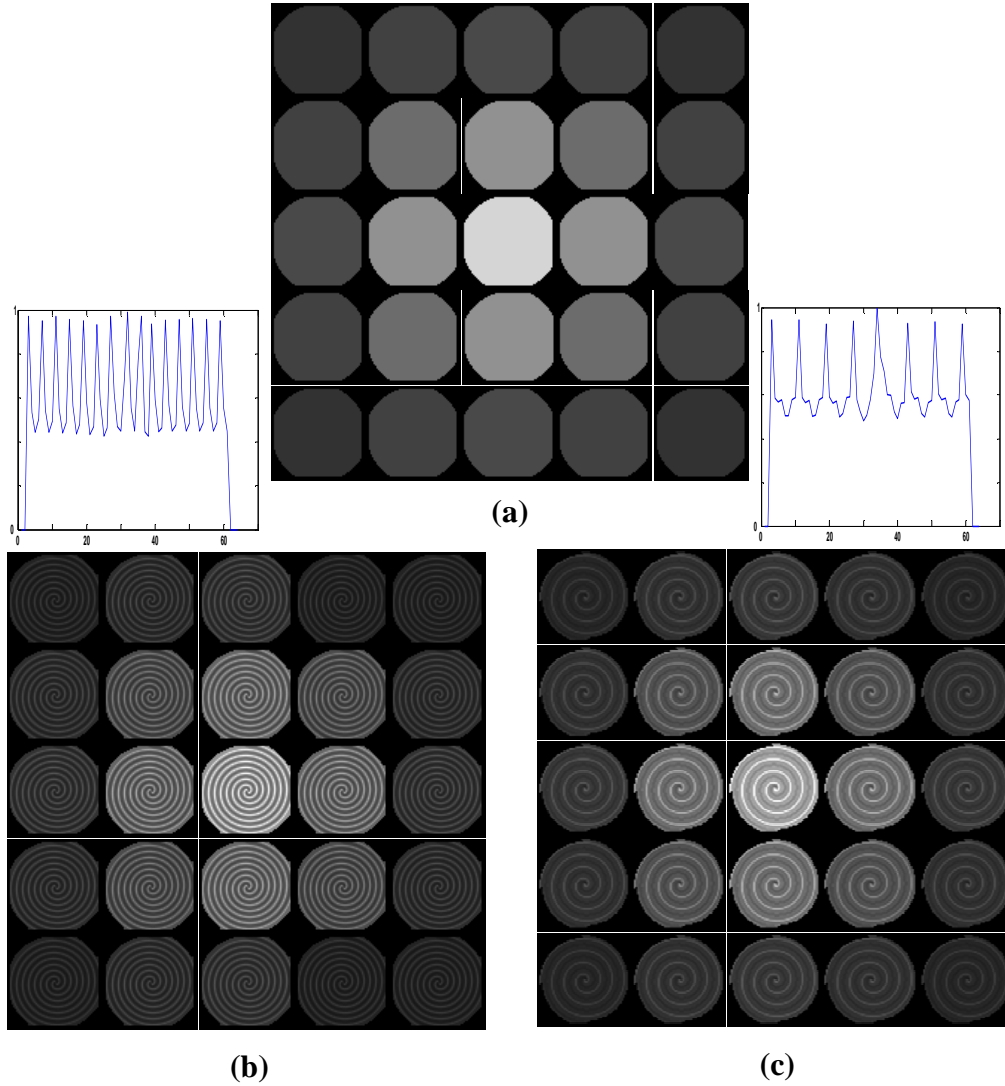


Figure 5.2 Absolute contribution maps for spiral trajectory

Simulation results of the contribution maps for 4-segment spiral with matrix size 64×64 accelerated at rate: (a) 1, (b) 2, and (c) 4. The maps are displayed in a configuration that reflects the contributions to each gridded point from a local neighborhood of 5×5 . The maps of (b) and (c) are weighted by the spiral trajectory. On the top of these maps, representative cross-section profiles of the maps are shown.

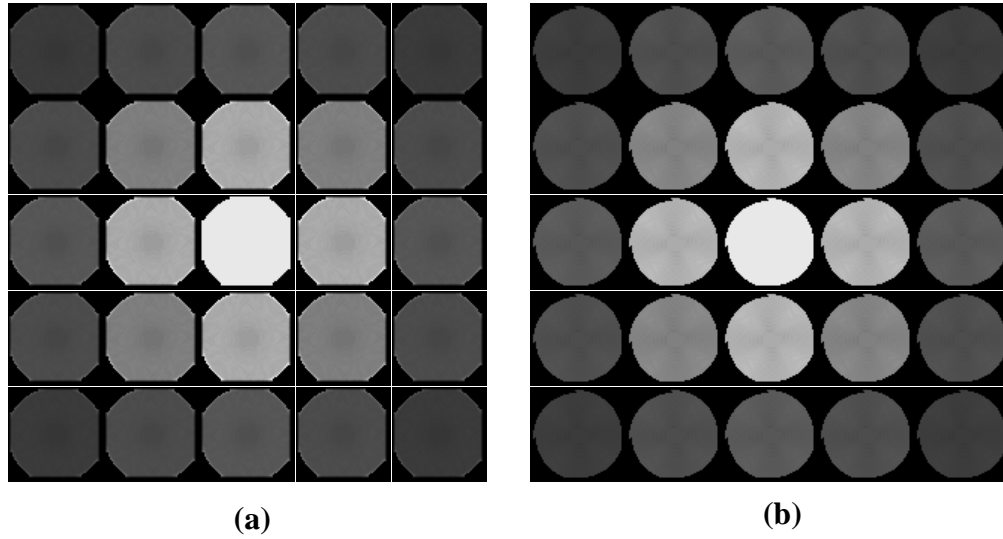


Figure 5.3 Relative contribution maps for spiral trajectory

Relative contribution maps for (a) $R = 2$ and (b) $R = 4$ obtained by dividing each map of Figure 5.2 ((b) and (c)) by its corresponding center map, respectively.

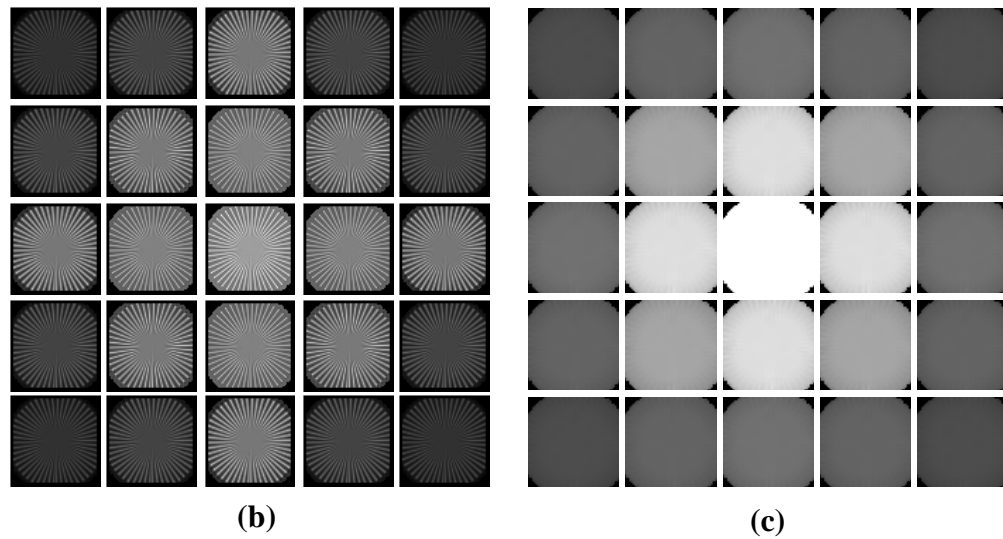


Figure 5.4 Simulation results for radial trajectory

Simulation results for a radial trajectory with matrix size 64×64 accelerated at rate 4: (a) absolute contribution map (b) relative contribution map. The maps are displayed in a configuration that reflects the contributions to each gridded point from a local neighborhood of 5×5 .

5.2.4 Determining the reconstruction weights

DUG weights are determined using a fraction of the data acquired without under-sampling which can be done before, after, or during the actual accelerated acquisition. Two copies of this calibration data are made. For each coil, spiral segments or radial projections in the first copy that would be normally omitted in an accelerated experiment are zero-filled, and the zero-filled data are subsequently gridded onto Cartesian grid, referred to as aliased grid, using Kaiser-Bessel function. At the same time, the second copy is also gridded to form the reference grid. This process is summarized in Figure 5.5. The gridded datasets are then segmented according to the procedure described above. We assume that each data point in the reference gridded k -space for each coil can be calculated by a simple weighted average (defined by a DUG kernel) of the corresponding point and its neighbors in the aliased k -space of all the coils as shown in Figure 5.5. This can be mathematically represented by

$$s_{l,m}^{ref-grid}(k_c) = \sum_{c \in \Pi_{c,R}} \sum_{l'=1}^L w_{c,l',m}^{(l)} s_{l'}^{aliased-grid}(k_c). \quad [5.8]$$

The system of linear equations formed by considering Eq. [5.8] for all samples of each group can be solved to determine the DUG reconstruction weights of the group. The set of optimized weighting coefficients of each group is obtained by applying the cross-validation as described in (22) to determine the kernel support that balance between artifacts and SNR.

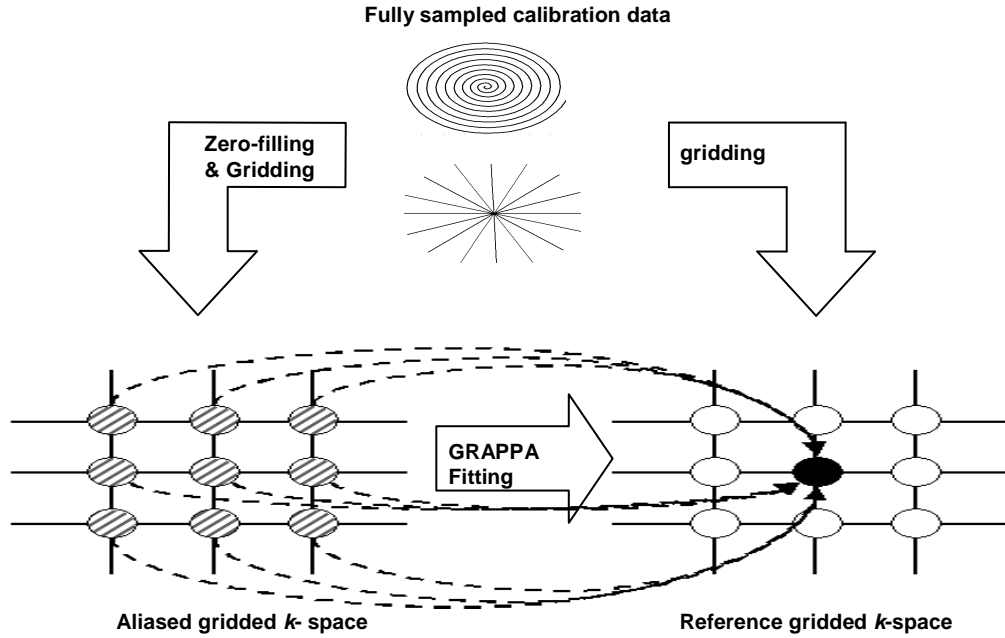


Figure 5.5 DUG weights calculation procedure

Both the fully sampled calibration data and its under-sampled copy (with zero filling) are gridded, clustered, and reordered to generate the reference and aliased hybrid spaces, respectively. By fitting the data in the aliased hybrid space (selected by the kernel support) to the target data in the reference hybrid space, the weights can be determined.

5.3 Methods

5.3.1 k -space trajectory

Our proposed method was demonstrated on spiral and radial trajectories. The spiral trajectory was a multi-interleaf Archimedean spiral (Figure 5.6a), described by the following general equations (23):

$$k_j(t) = \lambda \tau^\alpha e^{i(\omega\tau + \phi_j)}, \quad \begin{cases} j = 1 \dots J \\ \phi_j = 2\pi j / J \end{cases} \quad [5.9]$$

were $\tau = [0, 1]$ and a function of time and is determined according to the slew-rate and amplitude constraints as described in (Ref. 10), $\omega = 2\pi q$ with q equals the number of windings in k -space per interleaf, λ is a constant determined by the desired matrix size and field of view ($\lambda = M/(2 \times FOV)$, M : matrix size), $\alpha > 1$ defines the amount of oversampling near the origin of the k -space wanted.

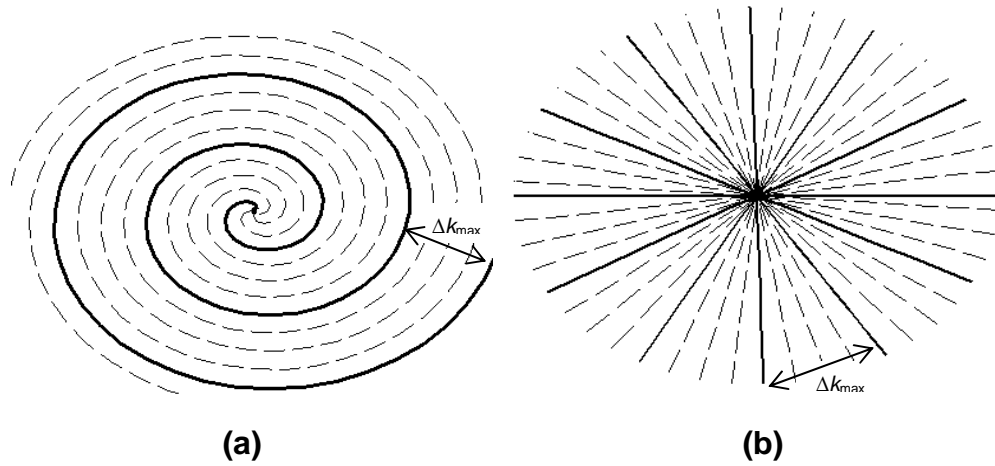


Figure 5.6 Non-Cartesian trajectories used

(a) 4-interleaved spiral and (b) radial trajectories accelerated at rate $R = 4$. The Filled line represents k -space data points acquired, and dash lines represent k -space point omitted. Δk_{\max} denotes the maximum separation of the k -space points and is R times the Nyquist required Δk .

The radial trajectory (Figure 5.6b) used in this work is described by Eq. [12],

$$k_j(t) = k_m \Gamma(t) e^{i\phi_j}, \quad \begin{cases} j = 1 \dots J \\ \phi_j = 2\pi j / J \end{cases} \quad [5.10]$$

$\Gamma(t)$ is a ramp function from -1 to 1 , and k_m is a constant determined by the desired matrix size and FOV ($k_m = M/(2 \times FOV)$). The number of radial views J is given by $J = \text{ceil}(2\pi M)$. The projections are azimuthally separated by phase offset ϕ_j .

5.3.2 Data acquisition

Spiral axial brain data and radial short axis view cardiac data were acquired on Siemens Tim Trio™ 3.0T system with a 12-channel head coil and on a 1.5T Siemens Avanto with a 12-channel cardiac matrix, respectively. In both cases, fully sampled data were acquired twice. The first measurement served as an external reference scan to derive the DUG kernels. The second measurement was downsampled to simulate parallel imaging with acceleration factors of 2 and 4 for spiral, 4 and 6 for radial, respectively. The spiral trajectory was implemented in the IDEA pulse programming environment (Siemens Medical Solutions, Malvern, PA, USA) and consisted of four-segment with matrix size: 128×128 , FOV: $256 \times 256 \text{ mm}^2$, slice thickness: 5.0 mm. The spiral specific acquisitions acquisition parameters were, TR/TE: 2000/30 ms. Maximum slew rate and gradient amplitude were 150 T/m/s and 23 mT/m, respectively. The radial data were acquired using True FISP sequence with: matrix size: 128×128 ; FOV = $280 \times 280 \text{ mm}^2$, TR/TE = 196.11/1.57 ms, flip angle 70° , slice thickness = 5 mm, 208 radial views acquired in 16 segments to meet the Nyquist criterion of $\pi/2 \times$ readout points.

5.3.3 Image reconstruction

Gridding using the Kaiser-Bessel function window was applied to both reference and undersampled data of the spiral and radial datasets followed by the segmentation of the gridded data as described above. Unless otherwise specified, the gridding window width of 6 was used. Next, cross-validation was applied to the reference dataset to determine the optimal kernel support of circular shape. Next, each datum in the aliased

gridded k -space of each coil was calculated by DUG interpolating its neighbors in the aliased gridded k -space of all coils. The final image was obtained by sum of square combination of all coil images. On the other hand, segmented GRAPPA reconstructions (12,14) were performed on the cardiac and brain data, respectively, for comparison. 16 segments along the readout and azimuthal directions for radial GRAPPA(12) and spiral GRAPPA(14), respectively, were used as described in their respective algorithms. All algorithms were implemented in MATLAB (The Mathworks Inc., Natick MA, USA) on a Pentium 3.00 GHz computer with 2GB RAM.

5.4 Results

Figure 5.7 presents the reconstruction results of the spiral brain data for $R = 2$ (b) and $R = 4$ (c). For each acceleration factor, the reconstructed images using direct spiral GRAPPA and DUG are shown. The reconstructed images are displayed with the same windowing for comparison. Below each image its absolute difference with the non-accelerated image (a) is displayed, with a window setting that is much lower than that for the reconstructed image. The optimal kernel supports (of circular shape) used for reconstruction were 9×9 ($R = 2$) and 11×11 ($R = 4$) for DUG and 4×4 ($R = 2$) and 5×5 ($R = 4$) for direct spiral GRAPPA. DUG reconstruction shows a better performance compared to spiral GRAPPA as indicated by the difference images. A quantitative comparison between these reconstructions is provided in Table 5.1.

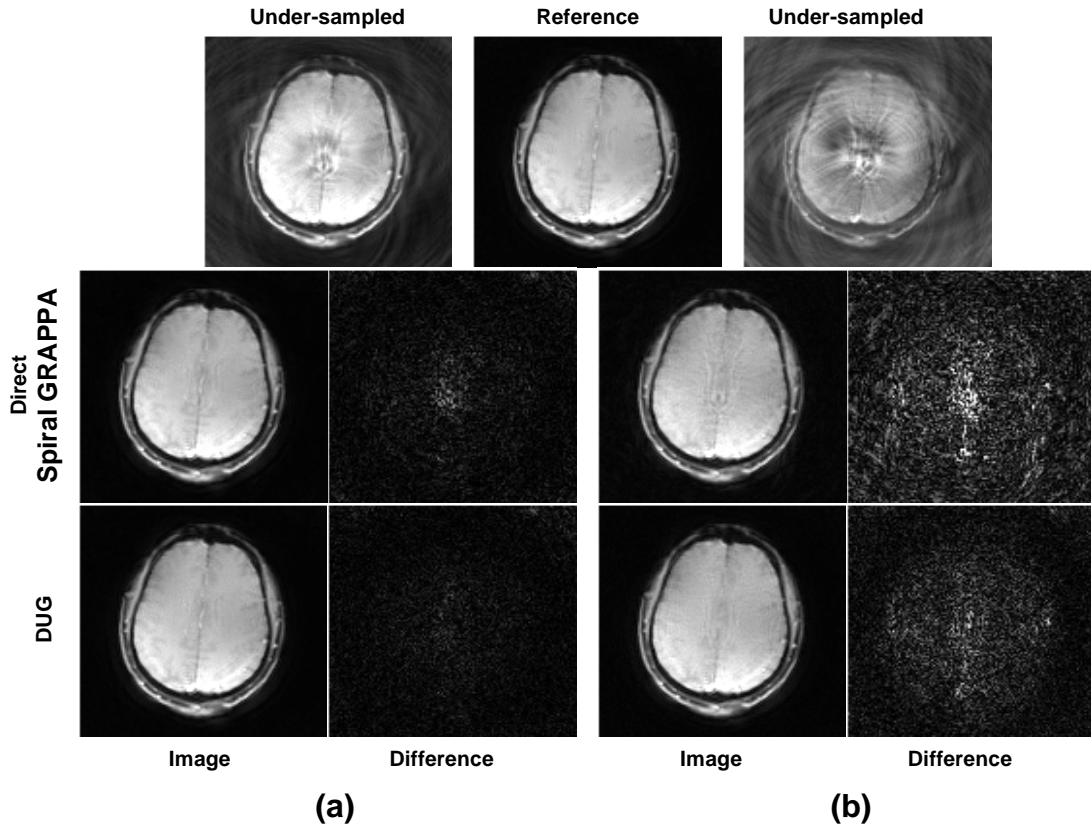


Figure 5.7 Spiral reconstructed images

(a) 2-fold acceleration and (b) 4-fold acceleration. For each stack images, the under-sampled image is shown at the top row and the middle and bottom rows correspond to the direct spiral GRAPPA and DUG reconstructed images, respectively. To the right of each reconstructed image, its absolute difference with the non-accelerated image is shown.

Gridding window width was varied to investigate its influence on the DUG reconstruction as illustrated in Figure 5.8 for $R = 4$. In all cases, the optimal kernel was used. It is obvious from visual inspection that the reconstruction performance increases with increasing gridding window width.

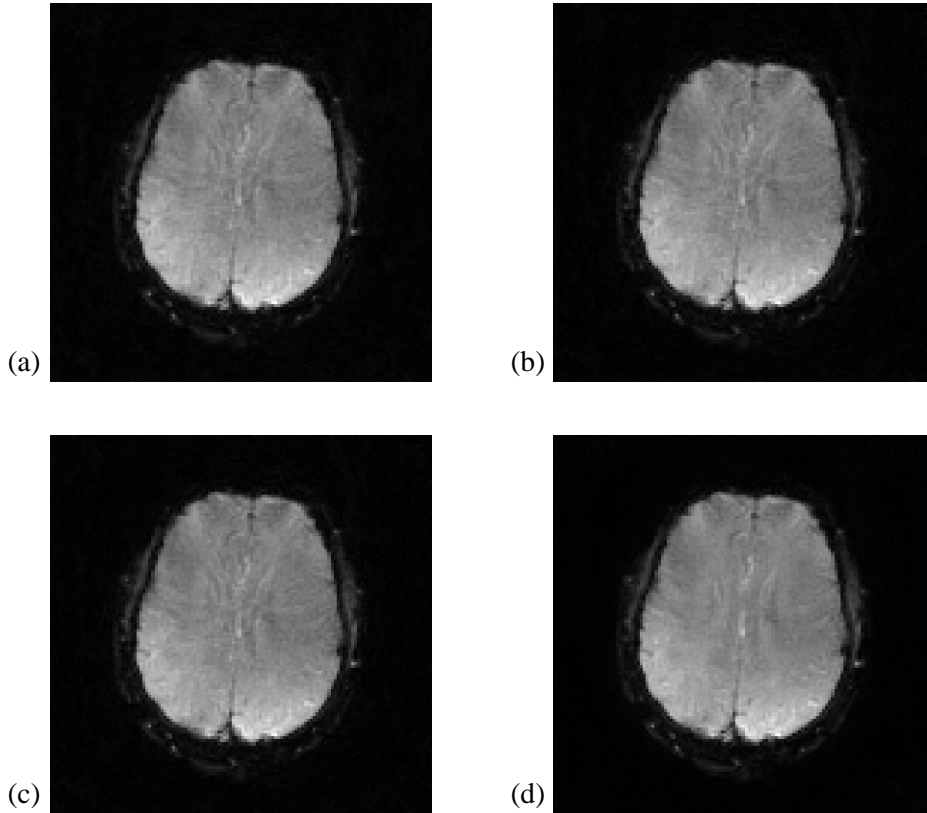


Figure 5.8 Reconstruction quality and gridding window

Influence of the gridding window width on the reconstruction performance for 4-interleaved spiral accelerated at rate 4. Widths of (a) 3, (b) 4, (c) 5, and (d) 6 were used. Reconstruction quality improves with increasing gridding window width.

Figure 5.9 presents the radial cardiac data results for $R = 4$ (b) and $R = 6$ (c). DUG reconstruction is compared to radial GRAPPA. The images are organized in the same manner as in Figure 5.7. The two reconstructions are visually comparable and only a quantitative comparison can be made as indicated in Table 5.2. The optimal kernel support used were 3×3 ($R = 4$) and 4×4 ($R = 6$) for DUG and 3×3 ($R = 4$) and 3×3 ($R = 6$) for radial GRAPPA;

5.5 Discussion

We have shown that an efficient reconstruction of non-Cartesian accelerated data can be achieved by deconvolution of the gridded k -space. While examples using spiral and radial have been shown, DUG can be used to reconstruct images from any trajectory with regularly organized patterns. In DUG, a judiciary interpretation of the energy distribution of the acquired signals during the gridding process is exploited in order to considerably reduce the number kernels necessary to achieve high quality reconstructed images, leading to faster reconstruction. The ability of DUG to reconstruct high quality data with a number of kernels per coil equal the parallel imaging accelerator, only one kernel more than that used in a normal Cartesian GRAPPA, provides a significant gain for non-Cartesian applications involving repetitive measurements such as function MRI, perfusion imaging, and diffusion tensor imaging.

The results of Figs. 5.7 and 5.9 and Table 5.1 clearly demonstrate the superior reconstruction performance of DUG as compared to segmented GRAPPA (12,14). DUG applies a weighted average interpolation at the last step of the two convolution processes (gridding followed by DUG interpolation), as opposed to segmented GRAPPA, and therefore better handles the error propagation during the reconstruction because of the ability of the DUG interpolation to blindly provide the best fit to the problem that is present to it. Compared to segmented GRAPPA utilizing n sectors, the proposed method is approximately $(n-1)$ times faster as indicated in Table 5.2.

The simulation analysis provided in the “Theory” section provides strong support to our segmentation strategy of the gridded data for efficient reconstruction. Although our proposed algorithm is not as theoretical exact as previously demonstrated non-Cartesian GRAPPA reconstruction schemes, it is far more efficient and reliable and can be used in a number of applications.

Table 5-1 Comparison between reconstruction mean square errors

	Radial		Spiral	
	R = 4	R = 6	R = 2	R = 4
Radial GRAPPA	182	366	-	-
Direct spiral GRAPPA	-	-	656	3840
DUG	165	321	456	1466

The demonstration of our method was performed with a full reference data acquired during the first measurement which corresponds to the acquisition scenario in many applications such as functional MRI, diffusion tensor imaging, and perfusion imaging. However, the reconstruction using weights derived solely from the low k -space resolution of the reference data showed comparable performance to that using the full reference data (results not shown). This suggests that the new method can also be used in applications requiring internal calibrations.

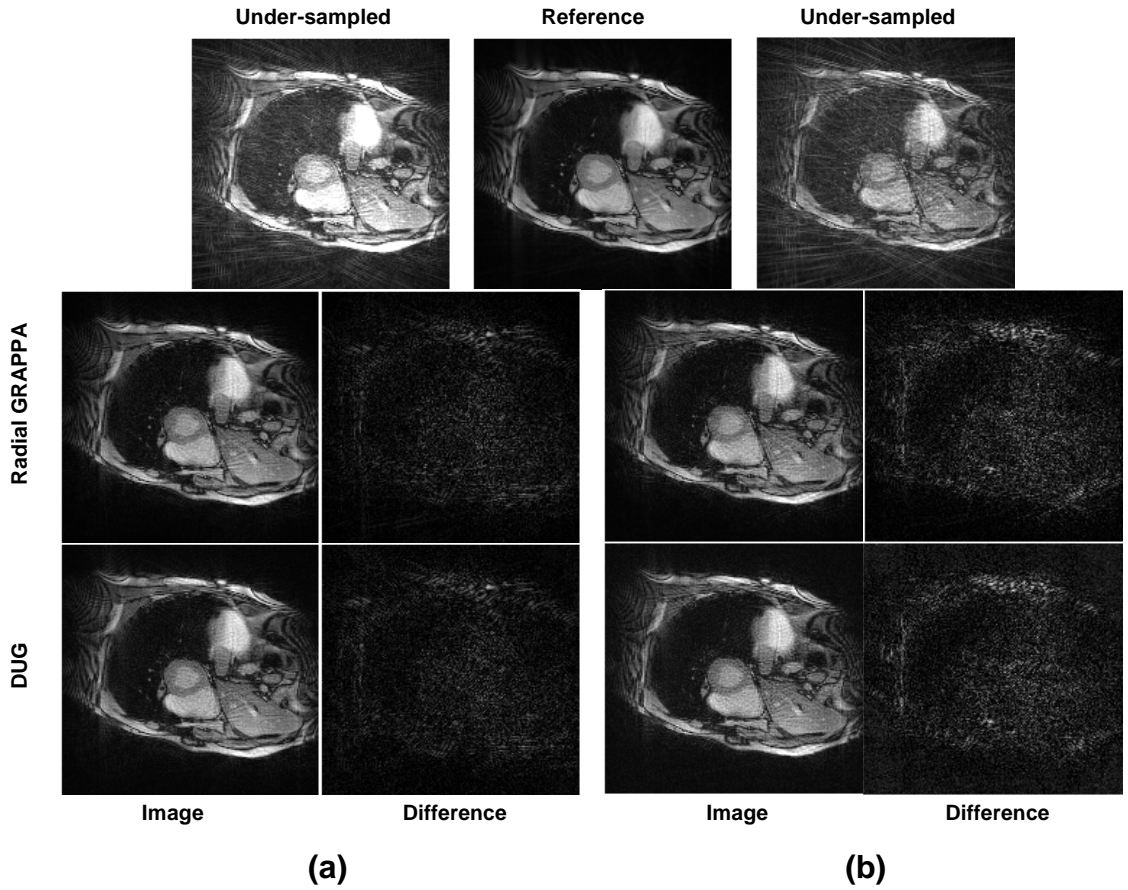


Figure 5.9 Radial reconstructed images

(a) 2-fold acceleration and (b) 4-fold acceleration. For each stack images, the under-sampled image is shown at the top row and the middle and bottom rows correspond to the direct radial GRAPPA and the new efficient GRAPPA reconstructed images, respectively. To the right of each reconstructed image, its absolute difference with the non-accelerated image is shown.

Distances between acquired non-Cartesian k -space data points increase with the parallel imaging acceleration factor. It is therefore important that the chosen gridding window width be large enough to avoid gridded data points with zero value as indicated by the results of Figure 5.8.

To avoid gridding errors that may occur when the sampled data violate the Nyquist criterion, the recently introduced pseudo-GRAPPA (18) algorithm utilizes a special gridding algorithm in which, instead of spreading each non-Cartesian datum on neighbor Cartesian grids as done in conventional convolution gridding algorithms, each datum is shifted to the nearest Cartesian grid leaving holes in the k -space. Then different patterns in the Cartesian grid are identified for normal GRAPPA interpolation. However, while the method can be applied to any arbitrary non-Cartesian trajectory, it may require a considerably high number of GRAPPA kernels (as one kernel per pattern is required) leading to potentially long acquisition time. Our proposed method can utilize any conventional gridding algorithm and provide considerable computational advantage while ensuring high quality images for non-Cartesian trajectories composed of regularly organized patterns.

Table 5-2 Comparison between computation times per unit image (in sec)

The total calculation time of the gridding table and GRAPPA weights are not included since they were virtually identical for the three methods.

	Radial		Spiral	
	R = 4	R = 6	R = 2	R = 4
Radial GRAPPA	145	158	-	-
Direct spiral GRAPPA	-	-	131	143
DUG	10	11	8	10

The total calculation for determining the gridding table and DUG weights took less than 2 min for all the data examined in this study. Once the DUG weights and the

gridding table were determined, subsequent imaging reconstruction including gridding took approximately 10 sec per image (as shown in Table 5.2), making online imaging reconstruction possible for non-Cartesian parallel imaging with large volume datasets.

5.6 Conclusions

A new parallel imaging reconstruction method for non-Cartesian parallel imaging is introduced and demonstrated on *in vivo* data. Compared to existing methods, DUG works on data gridded using conventional gridding algorithm and is faster and provides a significant gain for non-Cartesian applications that require repetitive measurements such as functional MRI and diffusion tensor imaging. The proposed method introduces further improvements in computation times and reconstruction efficiency for parallel imaging using non-Cartesian trajectories.

5.7 Chapter 5 References

1. Larkman DJ, Nunes RG. Parallel magnetic resonance imaging. *Phys Med Biol* 2007;52(7):R15-55.
2. Ahn CB, Kim JH, Cho ZH. High speed spiral-scan echo planar imaging. *IEEE Trans Med Imag* 1986;MI-5:2.
3. Meyer CH, Hu BS, Nishimura DG, Macovski A. Fast spiral coronary artery imaging. *Magn Reson Med* 1992;28(2):202-213.

4. Glover GH, Pauly JM. Projection reconstruction techniques for reduction of motion effects in MRI. *Magn Reson Med* 1992;28(2):275-289.
5. Scheffler K, Hennig J. Frequency resolved single-shot MR imaging using stochastic k -space trajectories. *Magn Reson Med* 1996;35(4):569-576.
6. Noll DC. Multishot rosette trajectories for spectrally selective MR imaging. *IEEE transactions on medical imaging* 1997;16(4):372-377.
7. Pipe JG. Motion correction with PROPELLER MRI: application to head motion and free-breathing cardiac imaging. *Magn Reson Med* 1999;42(5):963-969.
8. Pruessmann KP, Weiger M, Bornert P, Boesiger P. Advances in sensitivity encoding with arbitrary k -space trajectories. *Magn Reson Med* 2001;46(4):638-651.
9. Yeh EN, McKenzie CA, Ohliger MA, Sodickson DK. Parallel magnetic resonance imaging with adaptive radius in k -space (PARS): constrained image reconstruction using k -space locality in radiofrequency coil encoded data. *Magn Reson Med* 2005;53(6):1383-1392.
10. Griswold MA, Jakob PM, Heidemann RM, Nittka M, Jellus V, Wang J, Kiefer B, Haase A. Generalized autocalibrating partially parallel acquisitions (GRAPPA). *Magn Reson Med* 2002;47(6):1202-1210.
11. Samsonov AA, Block WF, Arunachalam A, Field AS. Advances in locally constrained k -space-based parallel MRI. *Magn Reson Med* 2006;55(2):431-438.
12. Griswold MA, Heidemann RM, Jakob PM. Direct parallel imaging reconstruction of radially sampled data using GRAPPA with relative shifts. In: Proc of 11th Annual Meeting ISMRM, Toronto 2003:2349.

13. Heberlein K, Hu X. Auto-calibrated parallel spiral imaging. *Magn Reson Med* 2006;55(3):619-625.
14. Heidemann RM, Griswold MA, Seiberlich N, Kruger G, Kannengiesser SA, Kiefer B, Wiggins G, Wald LL, Jakob PM. Direct parallel image reconstructions for spiral trajectories using GRAPPA. *Magn Reson Med* 2006;56(2):317-326.
15. O'Sullivan JD. A fast sinc function gridding algorithm for fourier inversion in computer tomography. *IEEE transactions on medical imaging* 1985;4(4):200-207.
16. Jackson JI, Meyer CH, Nishimura DG, Macovski A. Selection of a convolution function for Fourier inversion using gridding [computerised tomography application]. *IEEE transactions on medical imaging* 1991;10(3):473-478.
17. Hu P, Meyer CH. Parallel imaging reconstruction based on successive convolution in k -space. In: *Proc of 14th Annual Meeting ISMRM, Seattle 2006*:10.
18. Seiberlich N, Breuer F, Heidemann R, Blaimer M, Griswold M, Jakob P. Reconstruction of undersampled non-Cartesian data sets using pseudo-Cartesian GRAPPA in conjunction with GROG. *Magn Reson Med* 2008;59(5):1127-1137.
19. Le Bihan D. Functional MRI of the brain principles, applications and limitations. *Journal of neuroradiology* 1996;23(1):1-5.
20. Basser PJ, Mattiello J, LeBihan D. MR diffusion tensor spectroscopy and imaging. *Biophys J* 1994;66(1):259-267.
21. Le Bihan D, Mangin JF, Poupon C, Clark CA, Pappata S, Molko N, Chabriat H. Diffusion tensor imaging: concepts and applications. *J Magn Reson Imaging* 2001;13(4):534-546.

22. Nana R, Zhao T, Heberlein K, LaConte SM, Hu X. Cross-validation-based kernel support selection for improved GRAPPA reconstruction. *Magn Reson Med* 2008;59(4):819-825.
23. Kim DH, Adalsteinsson E, Spielman DM. Simple analytic variable density spiral design. *Magn Reson Med* 2003;50(1):214-219.

CHAPTER 6. SINGLE-SHOT MULTI-ECHO PARALLEL EPI FOR DTI WITH IMPROVED SNR AND REDUCED DISTORTION⁸

In this chapter, a multi-echo parallel echo planar imaging (EPI) acquisition strategy is introduced as a way to improve the acquisition efficiency in parallel diffusion tensor imaging (DTI). With the use of an appropriate echo combination strategy, the sequence can provide a signal-to-noise ratio (SNR) enhancement while maintaining the advantages of parallel EPI. Simulations and *in vivo* experiments demonstrate that a weighted summation of multi-echo images provides a significant gain in SNR over the first echo image. It is experimentally demonstrated that this SNR gain can be utilized to reduce the number of measurements often required to ensure adequate SNR for accurate DTI measures. Furthermore, the multiple echoes can be used to derive a T_2 map, providing additional information that might be useful in some applications.

6.1 Introduction

Diffusion tensor imaging (DTI (1)) permits noninvasive characterization of water self-motion in tissue and thereby provides information regarding the architecture and microstructure of a tissue. DTI has been proven to be an invaluable tool for the diagnosis

⁸ The work in this chapter has been adapted for publication as “Nana R, Zhao T, Hu X. *Single-shot Multi-echo Parallel EPI for DTI with Improved SNR and Reduced Distortion*. Magn Reson Med. (In Production)

of pathologies that modify tissue integrity (2). Characterization of water diffusion requires a set of diffusion-weighted (DW) images (3), acquired with diffusion gradients applied in at least six non-collinear directions, plus an image with negligible diffusion weighting (b_0 image). The greatest technical difficulty in acquiring DW images is to overcome the effects of macroscopic tissue motion, while retaining sensitivity to microscopic water motion. Owing to its insensitivity to motion, single-shot EPI (4) is the most widely used sequence for diffusion-weighted imaging (DWI). However, limited spatial resolution, sensitivity to field inhomogeneity, and low signal-to-noise ratio (SNR) are well-recognized limitations of EPI (5).

Multi-shot EPI has been used to circumvent the shortcomings of single-shot EPI (6). Multi-shot EPI reduces the off-resonance induced distortions proportionally to the number of interleaves and leads to an SNR improvement as compared to single-shot EPI. However, ghosting artifacts due to variations between shots limit its use in DWI. Due to the complexity of brain motion and DTI's high sensitivity to motion, navigator correction (7) does not always lead to ghosting free images. In addition, DWI using multi-shot EPI has a relatively low temporal resolution and throughput, limiting its use for clinical applications.

Parallel imaging (8,9) has been demonstrated to mitigate the shortcomings of single-shot EPI effectively in general (10), as well as for DTI (11). Parallel imaging exploits the sensitivity variations of coils in a coil array to reduce the number of encoding steps necessary for gradient-based spatial encoding. Combining parallel imaging with

EPI provides the advantages of a multi-shot EPI without the need of multi-shot but potentially compromises the SNR due to shortened readout and g-factor (8). Any compromise in SNR is detrimental for DTI since SNR is often limited in DTI. Therefore, it is highly desirable to improve the SNR in parallel diffusion-weighted EPI.

Multiple spin-echo or gradient-echo non-EPI acquisition strategies have been previously applied to improve the SNR (12,13) in DTI; these are, however, limited to ex-vivo studies due to the sensitivity to motion of non-EPI acquisition schemes. Parallel imaging reduces the EPI acquisition window, permitting the acquisition of multiple images with multiple echoes after a single excitation. In addition to the expected gains of reduced distortion artifacts and increased spatial resolution, the multi-echo approach is expected to improve SNR, increasing data acquisition efficiency, and provide a T_2 map. The present work investigates the benefits of acquiring multi-echo images using single-shot parallel EPI for DTI. For the combination of multi-echo images, weighted averaging in which the weights for each image are determined pixel-wise as the relative attenuation of its intensity to that of the first echo image is used. The improvement in SNR of this approach is characterized both by simulation and experiments. Its practical utility is demonstrated by fractional anisotropy (FA) maps. Furthermore, high-quality T_2 maps are also derived.

6.2 Methods

6.2.1 Data Acquisition and Processing

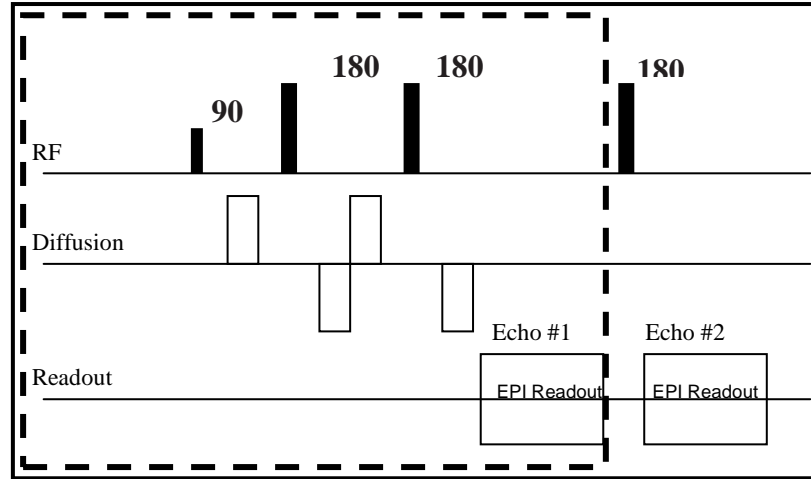


Figure 6.1 Single-shot Multi-echo parallel DTI sequence block diagram

In a standard diffusion-weighted imaging based on pulsed gradient spin echo (contoured with dash lines), a dual spin-echo with matched gradient pulses is used to provide the desired diffusion weighting while minimizing eddy current distortion (14). EPI readout produces a diffusion-weighted image with each excitation; nevertheless, only a single diffusion weighted image is acquired. We propose using multiple spin-echoes to acquire multiple EPI images with different echo times but with same diffusion weighting. Specifically, after the first diffusion-weighted EPI image is collected, another 180 RF pulse is added and a second EPI image, with the same diffusion weighting, is collected (contoured with filled lines). Additional echoes are collected by addition of 180 RF pulse. However, the long TE dictated by the length of the acquisition window limits the SNR in the second image. The combination of this approach with parallel imaging allows shorter acquisition windows, thereby shortening the TE. With this acquisition strategy, the echo images can be appropriately combined to improve the SNR and therefore reduce the number of measurements often used to improve the SNR

Starting from a standard diffusion-weighted EPI sequence (14), a multi-echo pulse sequence was constructed by the addition of refocusing RF pulses and EPI acquisition of the resultant spin-echoes (Figure 5.1). Phase encoding gradients are rewound after each echo so that the k -space trajectories are identical for all echoes. The sequence was implemented using the Siemens programming environment IDEA™.

All *in vivo* data were collected with participants' written consent in accordance with our institutional review board policy. The experiments were performed on a 3T Siemens Tim™ whole-body MR scanner (Siemens Medical Solutions, Malvern, PA) using a 12-channel head coil for reception and the body coil for transmission. Data were acquired on six healthy subjects (average age of 28 ± 4) with an imaging resolution of $2 \times 2 \text{ mm}^2$, a matrix size of 128×128 , and a slice thickness of 2 mm. Imaging protocols with an acceleration factor (R) of 2, 3, and 4, respectively, were used. The following imaging parameters were used: 5 echoes with minimum possible echo spacing, $TR = 3 \text{ s}$, bandwidth = 1954 Hz/pixel, FOV = 256 mm, 10 axial slices, $b = 1000 \text{ s/mm}^2$, and 12 diffusion weighting directions (plus $b = 0$). The echo parameters used for each imaging protocol are given in Table 6.1. GRAPPA (9) was used for image reconstruction. Additionally, standard spin echo (SE) images with five echoes were acquired on the same slices and at the same resolution for generating T_2 maps for comparison. The SE echo times corresponded to 30, 60, 90, 120, and 150 ms.

Echo combination was performed offline. FA maps were generated after distortion correction with FSL (FMRIB, Oxford, UK) which computes the apparent diffusion coefficient for each diffusion direction using only images acquired at $b = 0$ and at the desired b value. T_2 maps were calculated by mono-exponential fitting of the multi-echo b_0 images or SE images. All custom computer programs were implemented in Matlab (The MathWorks, Inc., Natick, MA, USA).

Table 6-1 Echo times (ms) used for different acceleration factors

R	TE(1)	TE(2)	TE(3)	TE(4)	TE(5)
2	96	141	186	231	276
3	85	117	149	181	213
4	80	104	128	156	184

6.2.2 Echo Combination Strategies and relative SNR Analysis

When multiple echo images are acquired where signals from successive images are coherent and the noises are incoherent, several strategies can be used to obtain a composite image. For the single-shot multi-echo parallel DTI acquisition, the signal strengths of later echoes are significantly attenuated as compared to the one of the first echo due to T_2 decay. In this case, weighted averaged combination of echoes would achieve higher gain in SNR than simple average and is therefore considered in this study. For simulating the SNR gain, a theoretical model of the ratio of the SNR of the combined echo to the first echo is derived as follows.

The measured signal in any pixel, \tilde{x} , can be represented as

$$\tilde{x}_i = xw_i + \xi_i, \quad [6.1]$$

where x is its true signal, i represents the echo number, ξ_i is the noise in echo image i assumed to have mean zero, w_i is the attenuation factor of the signal intensity of echo i with respect to that of the first echo ($i = 1$), implying that $w_1 = 1$. If N echoes are acquired, the weighted average of the measured signal, with weights given by the attenuation factors, is given by

$$\tilde{y} = \frac{x}{N} \sum_{i=1}^N (w_i)^2 + \frac{1}{N} \sum_{i=1}^N \xi_i w_i, \quad [6.2]$$

Let the SNR be the ratio of the mean value to the standard deviation of the noise, the ratio of the SNR of the combined echo to that of the first echo is given by

$$\frac{SNR_{\tilde{y}}}{SNR_{echo1}} = \sqrt{\sum_{i=1}^N (w_i)^2}. \quad [6.3]$$

In implementing the weighted averaging, a pixel-wise mono-exponential decay of the signal intensity between echoes was assumed and T_2 map was first calculated. The pixel weight was then derived according to

$$w_i(x, y) = e^{-\frac{\Delta TE_i}{T_2(x, y)}}. \quad [6.4]$$

where ΔTE_i is the echo spacing between echo i and echo 1, x and y are pixel coordinates.

The weights were determined on b_0 images and used for all DW images.

SNR was measured in 18 different ROIs (per subject) categorized as major white matter (WM) tracts, deep gray matter (GM) regions, cortical WM (refers to peripheral WM within the gyri), and cortical GM. These regions were identified based on FA maps and cross-referenced with b_0 images to avoid inclusion of CSF-filled spaces as described by others (15). Deep GM regions comprised of bilateral sections of the globus pallidus (GP), thalamus, and putamen. Deep WM ROIs included the genu and splenium of the corpus callosum, the anterior limb of the internal capsule (AIC), the posterior limb of the

internal capsule (PIC), and the external capsule (EC). Five regions of cortical WM, consisting of the superior frontal gyrus (SFG), supra marginal gyrus (SMG), superior temporal gyrus (STG), middle occipital gyrus (MOG), and postcentral gyrus (PG), were considered. The cortical GM ROIs resided in gray matter of SFG, SMG, STG, MOG, and PG. The SNR was determined according to a previously described procedure (16,17) to account for the number of receivers and the noise distribution in magnitude images obtained by sum-of-squares images. The ratio of the SNR of the combined image to that of the first echo image was computed for each ROI.

6.3 Results

It is evident from visual inspection that the distortions present in diffusion-weighted images acquired using a conventional DTI sequence without acceleration in the acquisition (Figure 6.1a) are significantly reduced in the ones obtained using the single-shot multi-echo parallel DTI sequence with an acceleration factor of 4 (the first echo is shown) (Figure 6.2). This improvement is in good agreement with previous observations that parallel imaging reduces distortion artifacts in EPI-DTI (10,11).

The simulated (according to equation [3]) ratios of the SNR of the combined image to that of the first echo for cerebro-spinal fluid (CSF), gray matter (GM), and white matter (WM) with assumed T_2 values of 2200 ms, 100 ms, and 80 ms, respectively, are shown in Figure 6.3a. In generating the plots, a constant echo spacing of 24 ms (which corresponds to the experimental value used for $R = 4$, see Table 6.1) was assumed

and the respective weights (attenuation factors) were determined using Eq. [1.4]. The CSF shows nearly no attenuation and its relative SNR contribution is approximately the square root of the number of combined echoes. The relative SNR of the combined image tapers off after 5 echoes for both GM and WM, with SNR gain plateaus at 54% and 45%, respectively.

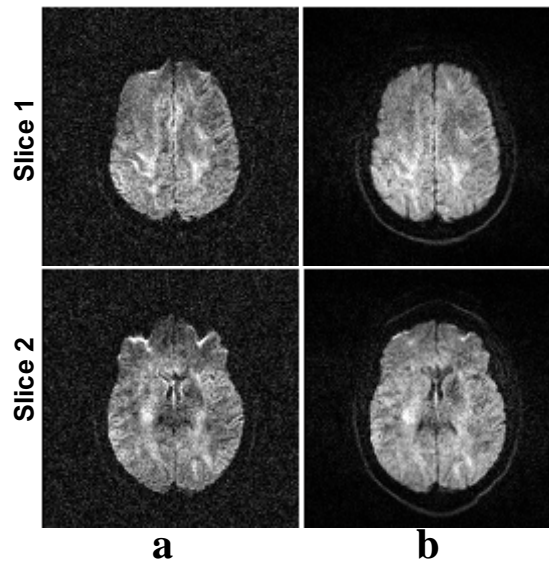


Figure 6.2 Evidence of geometric distortion reduction

Diffusion-weighted Images acquired using (a) a standard diffusion sequence without parallel imaging with TE = 132 ms and (b) single-shot multi-echo parallel DTI sequence with acceleration factor of 4 (only the first echo image acquired at TE = 80 ms is shown). In both cases, $b = 1000 \text{ s/mm}^2$. The distortion artifacts present in the images of column (a) are significantly reduced in those of column (b).

The results of the experimental relative SNR are shown in Figure 6.3b for three imaging protocols corresponding to an acceleration factor of 2, 3, and 4, respectively. Each plot reflects the average of the relative SNR across the ROIs and the subjects. These results indicate that the gain in relative SNR tapers off after about 2, 3, and 4 echoes for R

= 2, $R = 3$, and $R = 4$, respectively. At the plateau, the relative SNR gain was $(15 \pm 2)\%$ for $R = 2$, $(25 \pm 3)\%$ for $R = 3$, and $(36 \pm 5)\%$ for $R = 4$.

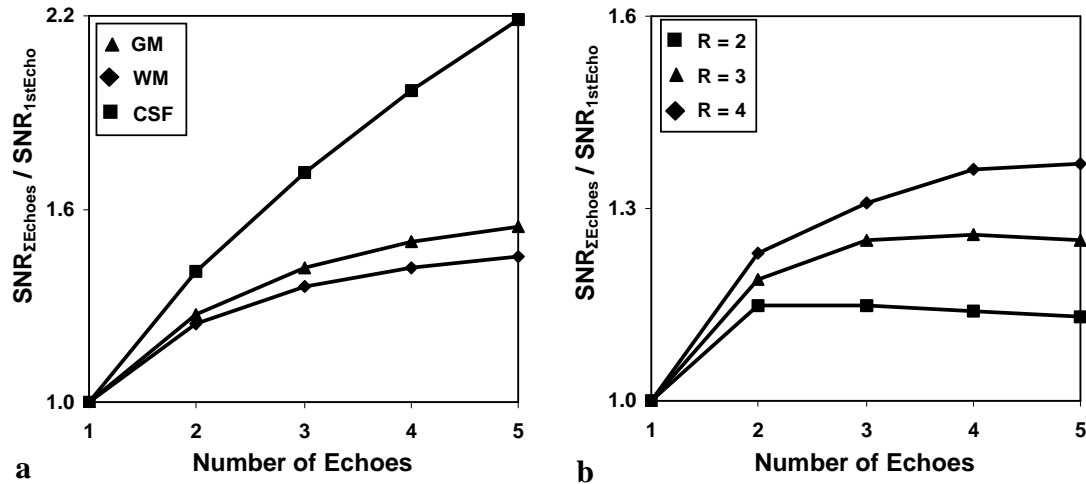


Figure 6.3 Simulated and experimental SNR gain

(a) Numerically derived ratio of the SNR of the echo combination to that of the first echo alone plotted as a function of the number of echoes combined, assuming a constant echo spacing of 24 ms and a T2 of 2200 ms, 100 ms, and 80 ms for cerebro-spinal fluid (CSF), gray matter (GM), and white matter (WM), respectively. (b) Experimental plots of the relative SNR change between the echo combination and the first echo as a function of the number of echoes for three different parallel imaging protocols corresponding to $R = 2$, $R = 3$, and $R = 4$, respectively. Each plot reflects the average of the relative SNR across the ROIs and the subjects.

Figure 6.4 presents FA maps of three slices (displayed in three different rows) generated (a) from a single-shot single-echo acquisition without averaging (corresponding to a scan time of 57 s), (b) a single-shot single-echo acquisition with two averages (corresponding to an acquisition time of 1 min 36 s), and (c) a single-shot 4-echo acquisition without averaging (corresponding to a scan time of 57 s). While the FA maps generated from the first echo without averaging exhibit significant noise level (Figure 6.4a), the noise level in the FA maps generated from the 4 echo combination is

significantly reduced (Figure 6.4c), on par with that in the FA maps generated with 2 averages (Figure 6.4b). Table 6.2 lists the mean FA values in the ROIs used for the SNR analysis. Note that for the cortical WM and cortical GM, respectively, values of individual ROIs were pooled together because they were very similar. The combination of 4 echoes led to FA values that are higher than those obtained with echo 1 without averaging and in good agreement with those obtained with echo 1 with 2 averages.

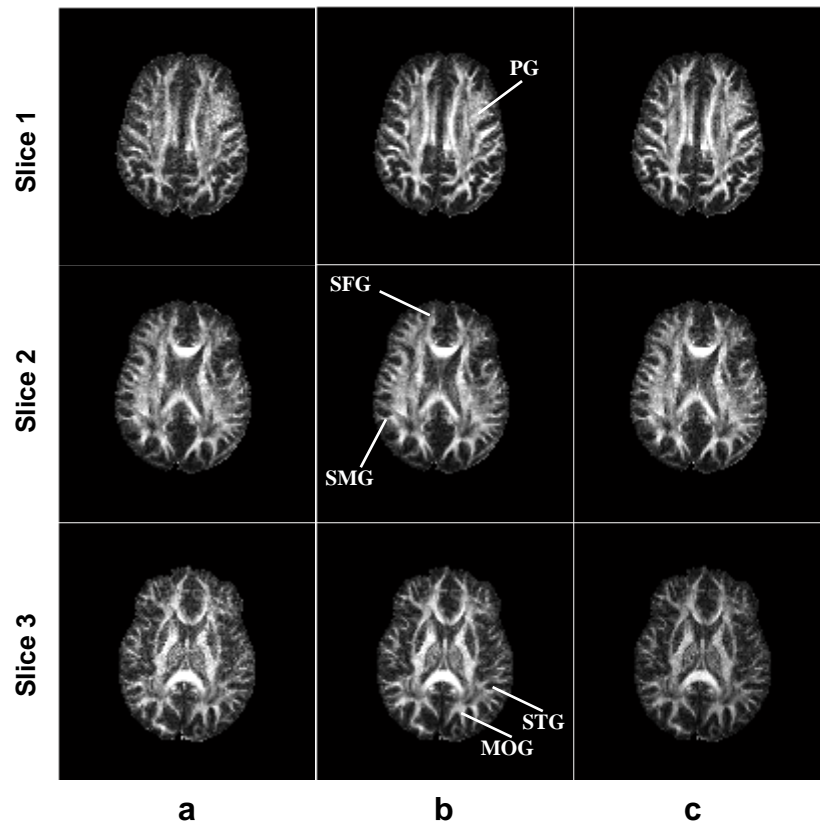


Figure 6.4 Illustration of acquisition efficiency improvement

Comparison between FA maps generated from multi-echo DTI datasets ($R = 4$) of 3 slices of a healthy subject from: (a) first echo without averaging; (b) first echo with 2 averages; (c) combination of four echoes of a single excitation without averaging.

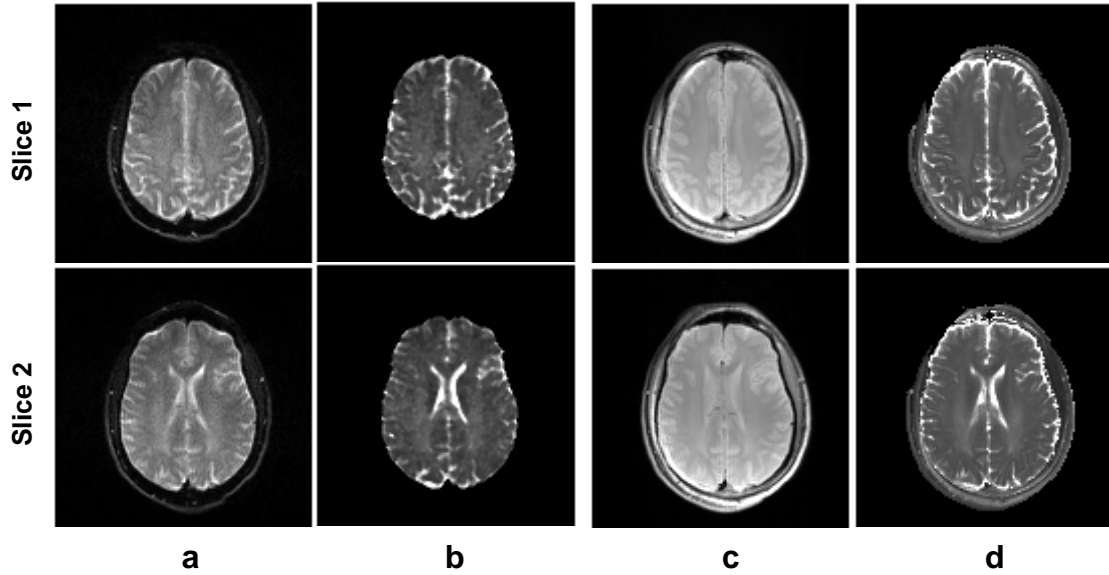


Figure 6.5 Comparison between T_2 maps

b_0 images (column a) and corresponding T_2 maps (Column b) generated from 4 echoes of a single excitation multi-echo DTI dataset ($R = 4$). SE images obtained on the same slices and corresponding T_2 maps are shown in columns c and d, respectively.

T_2 -weighted images (a) and the corresponding T_2 maps (b) of two slices generated from 4 echoes of an $R = 4$ multi-echo dataset are shown in Figure 6.5. For comparison, images of the same slices obtained using a standard multi-echo SE sequence and corresponding T_2 -maps are shown in panels (c) and (d), respectively. Table 6.3 lists the T_2 values of selected ROIs compared to those obtained using the standard multi-echo SE sequence.

6.4 Discussion

6.4.1 Echo combination and SNR

The numerical calculations allowed us to investigate theoretically the performance of combined image using multi-echo parallel EPI, assuming representative T_2 values and practical echo spacing. The latter mainly depends on the acquired matrix size and the bandwidth per pixel. The numerical results indicate that combining multiple echoes could result in SNR improvement and that considerably larger gains are expected in regions of longer T_2 or for acquisitions with short echo spacing. The experimental SNR ratio between the combined image and the first echo image (Figure 6.2b) largely follow the numerical prediction (Figure 6.3a). However, the height and the location of the SNR plateaus are slightly different from those of the simulations. Note that at $R = 4$, the experimental echo-spacing ($\Delta TE = 24$ ms) corresponds to that used for simulations. These discrepancies are likely due to errors in determining the attenuation factors (w_i) and the imperfection of the refocusing RF pulses. Overall, the experimental results support the prediction that echo combination leads to a SNR gain or at least maintains the SNR for all the number of echo combinations examined in this study.

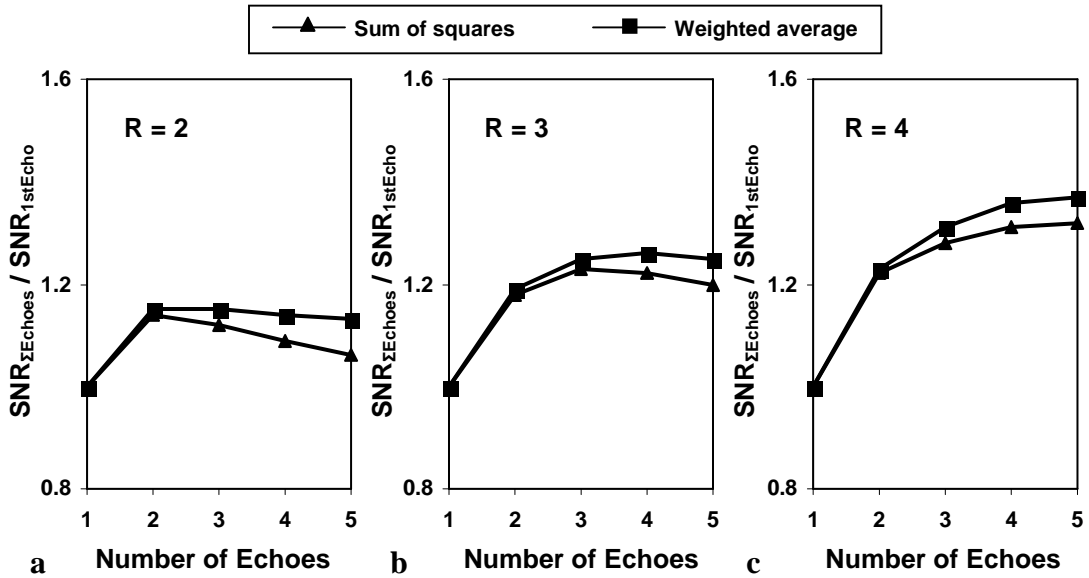


Figure 6.6 Comparison between SOS and weighted average echo combination

The figure compares the SNR in the combined images for different acceleration factors: (a) $R = 2$, (b) $R = 4$, and (c) $R = 4$. Weighted average performs better than SOS even for the b_0 images. It is expected that for the diffusion-weighted images, which have inherently low SNR, this difference would be bigger.

Sum of squares (SOS) is widely used to combine images from array coils and provides a near optimal combination when the SNR is high but is less than optimal at low SNR (18, 19). Because multi-echo DTI images have low SNR, weighted average instead of SOS is recommended for the singles-hot multi-echo parallel DTI images. This choice is supported by our comparison (Figure 6.6) of the two methods when applied to our experimental data, which showed that weighted average performs better.

In a previous paper, Matiello *et al.* (20) reported that the contributions of EPI readout and phase-encoding gradients to the b-matrix in DTI-EPI sequence were negligible. We have performed a similar analysis, taking into account the crusher and

slice selection gradients associated with refocusing RF pulses for additional echoes. With the imaging parameters used in this work, the difference in b-values between adjacent echoes ranges from 0.19 to 0.27 s/mm². This difference is negligible, even when multiplied by 4 for the 5th echo, compared to the nominal b-value of 1000 s/mm². For pixels containing multiple compartments with different T₂s, compartment-dependent T₂ decay between the echoes may complicate the combination of the echoes. This was not found to be a significant factor as there is no statistically significant difference between the FA values of the echo combination and the first echo with approximately similar SNR (see Table 6.2).

6.4.2 Acquisition efficiency

The fact that the SNR tapers off after the combination of two echoes for the acceleration factor of 2 and more echoes at higher reduction factors is understandable because the shorter echo spacing at higher *R* allows the inclusion of more echoes before the signal drops out due to T₂ decay. The 36% SNR increase in the combined image relative to the first echo image at *R* = 4 is close to the increase of 41% that would be expected from two averages of the first echo; this gain in SNR can be used to reduce the number of measurements and thereby leading to reduced scan time. This point is supported by the FA maps shown in Figure 6.4. The FA maps obtained from the first echo without averaging exhibits a significant noise level whereas the noise level of the FA maps generated from the weighted average of 4 echoes with the same acquisition time is significantly reduced, to a level comparable to that in the FA maps generated from 2 averages of the first echo. These noise level differences led to a significant difference in

the FA values reported in Table 6.2. The first echo without averaging resulted in a decrease in anisotropy as its signal is close to the noise level (21). On the other hand, averaging the first echo with two averages or combining 4 echoes led to a better estimate of the anisotropy.

Table 6-2 Comparison between calculated FA values of selected ROIs

The comparison is performed between the FA values derived from the first echo and those derived from the combined echo images, computed and represented in Figure 6.4.

Region	FA values		
	1 st echo image without averaging	1 st echo image with 2 averages	Weighted average combination of 4 echoes
Combined cortical white matter	0.38 ± 0.05	0.46 ± 0.04	0.43 ± 0.03
Combined cortical gray matter	0.17 ± 0.06	0.21 ± 0.02	0.20 ± 0.05
Major white matter			
Genu of Corpus callosum	0.60 ± 0.04	0.65 ± 0.03	0.66 ± 0.04
Splenum of Corpus callosum	0.64 ± 0.07	0.70 ± 0.03	0.68 ± 0.03
Anterior limb-internal capsule	0.55 ± 0.05	0.60 ± 0.03	0.62 ± 0.05
Posterior limb-internal capsule	0.56 ± 0.06	0.62 ± 0.04	0.61 ± 0.04
External capsule	0.40 ± 0.05	0.47 ± 0.02	0.45 ± 0.03
Deep gray matter			
Thalamus	0.33 ± 0.05	0.37 ± 0.03	0.35 ± 0.03
Putamen	0.18 ± 0.03	0.21 ± 0.03	0.23 ± 0.03
Globus pallidus	0.26 ± 0.06	0.31 ± 0.02	0.33 ± 0.04

The multi-echo approach provides more gain at high parallel imaging acceleration factors. In the past, an acceleration factor of 2 is often used for parallel imaging to avoid image degradation at high accelerations. With the availability of array coils with a large number of channels, it is now common to use higher acceleration factors, such as 3, 4, and even higher (22, 23). In fact, with the 12-channel commercial array coil used in this study, images obtained using an acceleration factor of 4 are of good quality.

While the multi-echo approach can enhance SNR per excitation, it could compromise the efficiency in multi-slice acquisitions. Specifically, with a given number

of slices, the minimum TR may be lengthened. In applications where a large number of slices are acquired, a good approach may be to acquire 2 echoes, achieving most of the SNR gain while avoiding significantly increasing the TR.

6.4.3 Additional T₂ map information

The quality of the T₂ maps derived using the single-shot multi-echo parallel EPI data (Figure 6.5b) is as good as the ones obtained using the standard multi-echo SE data (Figure 6.5d). Furthermore, as is illustrated in Table 6.3, no statistical significant differences between the corresponding T₂ values probed from selected ROIs were found, consistent with the results reported in the literature (24,25). This demonstrates the potential of the single-shot multi-echo parallel diffusion weighted EPI sequence for providing additional information that might be useful in some applications.

Table 6-3 Comparison between calculated T₂ values of selected ROIs

The comparison is performed between the T₂ values derived from the b₀ echo images of the single-shot multi-echo DTI and those derived from a multi-echo standard spin echo sequences.

Region	T ₂ Values, msec	
	Single-shot multi-echo parallel EPI	Standard SE
Cortical gray matter	70.42 ± 5.89	73.01 ± 4.53
White matter	54.71 ± 4.22	55.23 ± 3.64
Caudate Nucleus	61.95 ± 11.73	63.37 ± 9.15
Putamen	56.16 ± 9.12	57.65 ± 9.63
CSF	843 ± 206	871 ± 225

6.5 Conclusions

We have implemented and demonstrated a single-shot multi-echo parallel diffusion-weighted EPI sequence in improving the SNR while retaining the advantages of reduced distortion. The SNR gain can be used to reduce the number of measurements needed or improve the image resolution. Furthermore, these additional echoes can be used to calculate the T_2 map, providing complementary information that might be useful in some applications.

6.6 Chapter 6 References

1. Basser PJ, Mattiello J, LeBihan D. MR diffusion tensor spectroscopy and imaging. *Biophys J* 1994;66(1):259-267.
2. Horsfield MA, Jones DK. Applications of diffusion-weighted and diffusion tensor MRI to white matter diseases - a review. *NMR Biomed* 2002;15(7-8):570-577.
3. Le Bihan D. Molecular diffusion nuclear magnetic resonance imaging. *Magn Reson Q* 1991;7(1):1-30.
4. Mansfield P, Maudsley AA, Baines T. Fast scan proton density imaging by NMR. *J Phys E: Scient Instrum* 1976;9:271.
5. Farzaneh F, Riederer SJ, Pelc NJ. Analysis of T_2 limitations and off-resonance effects on spatial resolution and artifacts in echo-planar imaging. *Magn Reson Med* 1990;14(1):123-139.
6. Butts K, Riederer SJ, Ehman RL, Thompson RM, Jack CR. Interleaved echo planar imaging on a standard MRI system. *Magn Reson Med* 1994;31(1):67-72.

7. Anderson AW, Gore JC. Analysis and correction of motion artifacts in diffusion weighted imaging. *Magn Reson Med* 1994;32(3):379-387.
8. Pruessmann KP, Weiger M, Scheidegger MB, Boesiger P. SENSE: sensitivity encoding for fast MRI. *Magn Reson Med* 1999;42(5):952-962.
9. Griswold MA, Jakob PM, Heidemann RM, Nittka M, Jellus V, Wang J, Kiefer B, Haase A. Generalized autocalibrating partially parallel acquisitions (GRAPPA). *Magn Reson Med* 2002;47(6):1202-1210.
10. Griswold MA, Jakob PM, Chen Q, Goldfarb JW, Manning WJ, Edelman RR, Sodickson DK. Resolution enhancement in single-shot imaging using simultaneous acquisition of spatial harmonics (SMASH). *Magn Reson Med* 1999;41(6):1236-1245.
11. Jaermann T, Crelier G, Pruessmann KP, Golay X, Netsch T, van Muiswinkel AM, Mori S, van Zijl PC, Valavanis A, Kollias S, Boesiger P. SENSE-DTI at 3 T. *Magn Reson Med* 2004;51(2):230-236.
12. Gulani V, Iwamoto GA, Jiang H, Shimony JS, Webb AG, Lauterbur PC. A multiple echo pulse sequence for diffusion tensor imaging and its application in excised rat spinal cords. *Magn Reson Med* 1997;38(6):868-873.
13. Gulani V, Weber T, Neuberger T, Webb AG. Improved time efficiency and accuracy in diffusion tensor microimaging with multiple-echo acquisition. *J Magn Reson* 2005;177(2):329-335.
14. Reese TG, Heid O, Weisskoff RM, Wedeen VJ. Reduction of eddy-current-induced distortion in diffusion MRI using a twice-refocused spin echo. *Magn Reson Med* 2003;49(1):177-182.

15. Bhagat YA, Beaulieu C. Diffusion anisotropy in subcortical white matter and cortical gray matter: changes with aging and the role of CSF-suppression. *J Magn Reson Imaging* 2004;20(2):216-227.
16. Kellman P, McVeigh ER. Image reconstruction in SNR units: a general method for SNR enhancement. *Magn Reson Med* 2005;54(6):1439-1447.
17. Eratum to Kellman P, McVeigh ER. Image reconstruction in SNR units: a general method for SNR enhancement. *Magn Reson Med* 2005;54(6):1439-1447. *Magn Reson Med* 2007;58(1):211-212.
18. Larsson EG, Erdogmus R, Yan JCP, Fitzsimons. SNR-optimality of sum-of-squares reconstruction for phased array magnetic resonance imaging. *J Magn Reson* 2003;163:121-123.
19. Gilbert G, Simard D, Beaudoin G. Impact of an improved combination of signals from Array coils in diffusion tensor imaging. *IEEE Trans Med Imaging* 2007;26(11):11428-1436.
20. Mattiello J, Basser PJ, Lebihan D. The b matrix in diffusion tensor echo-planar imaging. *Magn Reson Med* 1997;37(2):292-300.
21. Jones DK, Basser PJ. "Squashing peanuts and smashing pumpkins": how noise distorts diffusion-weighted MR data. *Magn Reson Med* 2004;52(5):979-993.
22. Zhu Y, Hardy CJ, Sodickson DK, Giaquinto RO, Dumoulin CL, Kenwood G, Niendorf T, Lejay H, McKenzie CA, Ohliger MA, Rofsky NM. Highly parallel volumetric imaging with 32-element RF coil array. *Magn Reson Med* 2004;52(4):869-877.

23. McDougall PM, Wright SM. 64-channel array coil for single echo acquisition magnetic resonance imaging. *Magn Reson Med* 2005;54(2):386-392.
24. Jezzard P, Duewell S, Balaban RS. MR relaxation times in human brain: measurement at 4 T. *Radiology* 1996;199(3):773-779.
25. Rohan ML, Eskesen JG, Anderson CM, Kaufman MJ, Renshaw PF. TE Stepping with EPI: Reliable Relaxometry. *Proc of the Annual Meeting of ISMRM 2004; Kyoto 2004*:p. 993.

CHAPTER 7. CONCLUSIONS

Parallel imaging is now an established technique for accelerating imaging speed beyond conventional MRI limits. This increase in speed has far-reaching consequences with respect to increasing the accuracy of clinical diagnostic accuracy, reducing the cost of research and medical examinations, and improving patient comfort. Ongoing research continues to address various issues that hinder some aspects of parallel MRI applications. In this dissertation work, five specific challenges to optimal and efficient parallel image reconstruction have been explored with practical solutions to ease routine clinical and research applications presented in Chapters 2-6.

Chapters 2 and 3 explored methods for characterizing and minimizing errors in k -space based parallel imaging. Chapter 2 presented a method based on cross-validation for selecting the reconstruction kernel support that results in an optimal compromise between accuracy and stability, i.e. best balancing the tradeoff between artifacts and SNR. Because the method is simple and applied in post-processing, it can be used routinely with many existing reconstruction algorithms.

To further facilitate reconstruction optimization and characterization, Chapter 3 introduced a simple and robust metric that exploits the shift invariance property of the reconstruction kernel to provide a goodness measure of k -space interpolation for parallel imaging. This in turn has enabled optimization and quantitative comparisons of several

parallel MRI reconstruction techniques. The metric extends to applications where the cross-validation based optimization finds limitations.

Chapters 4 and 5 discussed strategies for improving efficiency of parallel image reconstruction in applications involving large datasets. In Chapter 4, a strategy was introduced that uses the metric describes in Chapter 3 to improve reconstruction efficiency and accuracy in free breathing non-gated dynamic parallel imaging by exploiting the cyclic nature of the respiration induced chest movement. This strategy can be coupled with existing algorithms to facilitate real-time on-the-fly image reconstruction.

In Chapter 5, a method based on GRAPPA reconstruction was introduced to improve computation time and reconstruction efficiency for parallel imaging using non-Cartesian trajectories. In many cases, the method adds a relatively small computational time per unit image as compared to conventional GRAPPA, making online parallel image reconstruction for non-Cartesian applications involving large datasets now possible.

Finally, Chapter 6 presented a pulse sequence that combines parallel imaging and multi-echo strategy to improve SNR in DTI. This SNR gain can be utilized to improve acquisition efficiency. Additionally, the multiple echo-images can be used to generate a T_2 -map, complementing information that can be useful in some applications.

In summary, methods developed in this thesis work address challenges in parallel image reconstruction. This dissertation represents a significant contribution to the improvement of existing state-of-art reconstruction methods and will provide useful tools and insights for future developments in parallel imaging.